Monitoring of Fatigue Damage for Offshore Wind Turbine Foundations

Investigating Operational Strain Estimation Techniques

J.O. Norbruis

Master's Thesis

Monitoring of Fatigue Damage for Offshore Wind Turbine Foundations

Investigating Operational Strain Estimation Techniques

by

J.O. Norbruis

to obtain the degree of Master of Science
at the Delft University of Technology
and the Norwegian University of Science and Technology
to be defended publicly on 12 December, 2017 at 10.30.

Student number:	4086880	
Project duration:	January 11, 2017 – December 12, 2017	
Thesis committee:	Prof. dr. ir. A. V. Metrikine,	TU Delft, chairman
	Ir. D. J. M. Fallais,	TU Delft
	Prof. dr. ir. S. K. Ås	NTNU
	Ir. R. J. N. J. Luiken,	Van Oord

An electronic version of this thesis is available at `http://repository.tudelft.nl/`.

EWEM TU Delft NTNU Norwegian University of Science and Technology Van Oord Marine ingenuity

Preface

This thesis has been written as finalisation of the European Wind Energy Master (EWEM) program and to obtain a Master's degree in Offshore Engineering at the Delft University of Technology, as well as a Master's degree in Wind Energy at the Norwegian University of Science and Technology.

The idea for this thesis was brought up in collaboration with Van Oord bv, a marine contractor. The final scope was determined by Delft University of Technology. The work has been performed at Van Oord in cooperation with the Delft University of Technology and the Norwegian University of Science and Technology. The work for this project was spread out over the spring and autumn semesters of 2017.

The aim of this thesis is to shed more light on the application of estimation methods for in-service stresses in offshore wind support structures and their impact on the fatigue damage accumulation. It is assumed that the reader has basic knowledge of structural dynamics.

The technical details, i.e. specifications of the Gemini offshore wind farm and the Van Oord finite element model for monopile foundations, are proprietary information of Van Oord bv. and may not be copied without specific authorisation from Van Oord bv.

The Hague, December 5, 2017

Joris Norbruis

Acknowledgements

The last year, I have worked on my thesis at Van Oord under the Structural Engineering department of Van Oord - Offshore Wind Projects. I would like to thank Wouter Dirks and Wouter op den Velde for giving me the opportunity to work within this department.

Furthermore, I would like to thank my colleagues within the department for their help and for the atmosphere that helped me stay on track. Of course a special thanks goes to my supervisor Ralph Luiken who has been able to answer any question regarding offshore wind foundations I have been able to come up with. Even more, he has deepened by understanding of the design of offshore wind support structures and has been an invaluable source of information regarding ANSYS Mechanical apdl and its application to foundation design.

Also, I would like to thank Eliz-Mari Lourens, not only has she sparked my interest for structural health monitoring during the Load Identification & Monitoring of Structures course. She also was my supervisor within the Delft University of Technology for the main part of this project. She ensured that I kept the theoretical background in mind and made sure I was critical of the generated results. Further I would like to thank Dominik Fallais who stepped in as my supervisor during the last months of the work on my thesis, he especially helped me to set concrete goals and to present my findings in a structured fashion, while asking critical questions along the way. Sigmund Ås has been my supervisor from the Norwegian University of Science and Technology and has been a great help keeping an eye on the mechanics regarding the stress and strain regimes, this was very useful as in the greater picture this sometimes became a bit underexposed.

In addition, I would also like to thank Andrei Metrikine from Delft Univeristy of Technology for his guidance, comments and discussions.

Finally, I would like to thank my family and friends for supporting me during this project and taking the time to listen to the stories of my adventures and struggles in Gorinchem and Delft.

J.O.N.

Summary

A global focus on the shift to renewable energy has introduced international targets for sustainable energy production, which have strongly increased the interest in offshore wind turbines (OWT's). In order to make offshore wind energy even more competitive, the levelised cost of energy for this industry has to be brought down. One of the OWT aspects that can still be developed further, with respect to the cost, is the foundation. As these structures usually have a design lifetime of 25 years and are subjected to cyclic loading, the foundation design is often driven by the fatigue limit state. In order to monitor the fatigue damage imposed on the structure, the stress history at certain "hot spots" needs to be known. Whereas measuring at every hot spot is not feasible, schemes have been developed to estimate the stresses based on a limited amount of sensors.

Van Oord is a marine contractor with a large portfolio in offshore wind energy, currently performing the foundation design in-house and is also active as wind farm owner. Insights into fatigue damage accumulation could lead to optimisation in both the design and operational stages of the life of an OWT. In the design phase, a more economical way of guaranteeing 'safe-life' design could be found and for the operational phase knowledge about the accumulation of fatigue damage could enable operation to continue passed the original design life. To facilitate predictions regarding the potential of life time extension, a requirement set by Van Oord is that the accuracy of fatigue computations based on estimated stresses should be within 2 % of the control values, i.e. an accuracy of one year in the lifetime of the structure should be achieved. The objective of this study can be summarised as:

"Verify and compare techniques for the estimation of in-service strains in offshore wind support structures from a limited set of sensors, for use in fatigue damage monitoring."

In this study two distinct approaches for the estimation of operational strains are investigated. The first approach is based on interpolation of section forces which are obtained from strain measurements at different levels; subsequently interpolated section forces can be transformed into strains using basic constitutive relations from structural mechanics. Since the strain measurements have to be taken from the region of interest, i.e. below the mudline, Fibre-Bragg Grating strain sensors are suggested for this application since they are both light and small, thus increasing their chance of survival during pile driving. It is found that the underlying assumption for the Section Force Interpolation (SFI) method, that the moment distribution between two measurement levels can be approximated as varying linearly with the distance to the point of interest, is valid. Therefore, the bending moment of a point in between two measurement levels can be calculated, as well as the related strains.

The second approach is the Multi-Band Modal Decomposition and Expansion (MDE) technique that was introduced by Iliopoulos et al. [38]. This method uses numerically or experimentally obtained structural mode shapes to expand a number of vibrational response measurements into modal responses for a considered frequency band of the measurement data. For OWT's one quasi-static and two dynamic bands are considered. The total operational strains are obtained by superposition of the strain contributions estimated from each band. Modal strain distributions and strain sensors are used to estimate the strain response in the quasi-static band and a combination of mode shapes, modal strain distributions and accelerometers is used to estimate the strain contribution from the dynamic bands. Furthermore, it is investigated if the Multi-Band MDE method can be improved to reduce its sensitivity to measurement noise; therefore the Least-Squares (LS) algorithm is replaced by a weighted LS algorithm which can assign weight to measurements according to their relative noise levels.

For the analysis of the aforementioned estimation methods, finite element(FE) models were set up to obtain the required structural input, i.e. mode shapes. To set up the FE models, the Van Oord in-house modelling tool for monopile foundations was used. To verify the proper set-up of this tool a verification was performed with the design documents for the Gemini Wind Farm. Since no real measurement data was available, the choice was made to utilise FE models to simulate the response of the structure to 5 load cases. Time domain

analyses were run in ANSYS where the structure was subjected to irregular wind and wave loading, from these analyses strain and acceleration measurements were read out, these would later be used as input for the SFI and MDE prediction methods. Control measurements were also generated at this point, so that the predicted values could be compared to output of the FE analysis. As the current analysis method utilises only computer generated data, the measurement signals are completely noise free. A situation where the input signals are contaminated by measurement noise is more realistic, in order to simulate the effect of these errors, the measurement data was manually contaminated with white noise.

The strain reconstruction based on Section Force Interpolation has the potential to give accurate estimations of the strain in the foundation, using a very simple and robust method. Under the condition that strain sensors are calibrated properly; the reconstructed signals are good estimates of the original signal, even for high levels of measurement noise, showing no sign of drift in the results and keeping a strong correlation with the frequencies found in the uncorrupted strains. Obtaining the strain measurements necessary for this reconstruction method does introduce a complicating factor as measurements along the length of the foundation are required.

Behaviour of the moment distribution along the length of the foundation is shown to be linear in the sections above mudline and below $2.5D$, the section between mudline and $2.5D$ below mudline cannot be approached by a linear relation, D is the pile diameter. Thus, for strain reconstruction, with 3 sensors covering each linear region already a decent estimation will be obtained for those areas, however to properly measure the peak moment it is advisable to install at least 2 sensors between 1 and $2D$ below the mudline. Thus a measurement system with 8 sensors would results in more accurate results than presented in this work.

It was found that the Multi-Band Modal Decomposition and Expansion method for full-field strain estimation suggested by Illiopoulos et al. shows accurate results for simulations on a FEM model of an OWT foundation excited by irregular waves and wind loads [38]. The multi-band approach allows for the use of both strain gauges and accelerometers, enabling the method to predict both quasi-static and dynamic response.

During the sensitivity analysis of the MB-MDE it was found that the sensor Configuration [*Mode: 1,2&3, Sensor: 87,66,34&19m*] provides the best accuracy under LC's 1 trough 7 and [*Mode: 1&2, Sensor: 66,34&19m*] is the optimal configuration for LC 8. The configurations for LC 1 and 7 differ significantly from the previous suggested configurations in the work on Multi-Band MDE by Iliopoulos et al.[38]; however, since the fact that the other research was performed on a different structure is expected to be the main reason for this dissimilarity.

Introducing the wLS algorithm to the Multi-Band MDE method did not result in significant improvement of the strain estimation results for the investigated load cases. The filtering required for the Multi-Band method already decreases the effect of noise on the signal and applying the MB-MDE strongly decreases the influence of measurement noise on the estimation results.

For noise levels of 0 % both methods perform very well, if measurement noise is introduced the results computed with the Multi-Band MDE become less accurate and show large amplitude and phase errors for noise levels of 5 and 10 %, while for the SFI method only limited amplitude errors are observed. Thus with respect to fatigue computation based on input signals contaminated with measurement noise, the SFI method gives better results.

Contents

List of Abbreviations

AA anti-aliasing

BoP Balance of Plant

BEM Blade Element Momentum

CAPEX Capital Expenditure

CB Craig-Bampton

DAU Data Acquisition Unit

DFT Discrete Fourier Transform

DNV-GL Det Norske Veritas Germanischer Lloyd

DoF Degree of Freedom

DSP Digital Signal Processing

DTG Draw Tower Grating

EPC Engineering, Procurement and Construction

FA For-Aft

FAT Factory Acceptance Test

FBG Fiber Bragg Grating

FE Finite Element

FEM Finite Element Method

FLS Fatigue Limit State

FRAC Frequency Response Assurance Criterion

GWEC Global Wind Energy Council

HF High Frequency

IRENA International Renewable Energy Agency

LCOE Levelised Cost Of Energy

LF Low Frequency

LTI Linear Time Invariant

LS Least-Squares

MB-MDE Multi-Band Modal Decomposition & Expansion

MEMS Micro-Electro-Mechanical System

MDE Modal Decomposition & Expansion

MP Monopile

MSL Mean Sea Level

MWL Mean Water Level

OHVS Offshore High Voltage Substation

OMA Operational Modal Analysis

OWF Offshore Wind Farm

OWT Offshore Wind Turbine

pp percentage point

PSD Power Spectral Density

QS Quasi-Static

RNA Rotor and Nacelle Assembly

SHM Structural Health Monitoring

SJOR Slip-Joint Offshore Research

SS Side-Side

TP Transition Piece

TRAC Time Response Assurence Criterion

ULS Ultimate Limit State

wLS Weighted Least-Squares

Nomenclature

Greek

$\boldsymbol{\phi}$	Matrix of the considered mode shapes $\{n_{DoF} \times n\}$	[-]
$\boldsymbol{\phi}_m$	Matrix with mode shape amplitudes for measured locations $\{n_m \times n\}$	[-]
$\boldsymbol{\phi}_p$	Matrix with mode shape amplitudes for predicted locations $\{n_p \times n\}$	[-]
β_{pitch}	Blade pitch angle	[°]
$\Delta\sigma$	Amplitude of a stress cycle	[N/m^2]
$\Delta\sigma_i$	Amplitude of stress cycle i	[N/m^2]
$\Delta\sigma_m$	Measured stress signal	[N/m^2]
$\Delta\sigma_p$	Predicted stress signal	[N/m^2]
ϵ_a	Axial strain	[-]
$\epsilon_{B,y,T}$	Elastic bending strain on the positive y side of an element (local axis system)	[-]
ϵ_b	Bending strain	[-]
ϵ_m	Measured strain	[-]
η_s	Total surface elevation	[m]
$\hat{\omega}$	Normalised angular frequency	[rad/s]
κ_y	Curvature around the z axis of an element (local axis system)	[1/m]
λ_B	Bragg wavelength of an FBG	[m]
μ_D	Mean of yearly damage	[-]
ω	Angular frequency	[rad/s]
ω_{rotor}	Rotor speed	[rpm]
Φ_m	Phase angle of the complex valued coefficients of the DFT	[-]
ρ_ϵ	Photo-elastic constant of the fibre core material	[-]
σ_D	Standard deviation of the yearly damage	[-]
σ_a	Axial stress	[N/m^2]
$\sigma_{b,dy}$	Nominal bending stress that acts at detail dy	[N/m^2]
$\sigma_{b,x}$	Bending stress, projected on the x-axis	[N/m^2]
$\sigma_{b,y}$	Bending stress, projected on the y-axis	[N/m^2]
σ_b	Bending stress	[N/m^2]
θ_{dy}	Angle between location of detail dy and the y-axis	[°]
θ_y	Angle between the moment loading and the y-axis	[°]

Roman

$\boldsymbol{\epsilon}_p$	Estimated total strain response	[-]
$\boldsymbol{\epsilon}_p^{HF}$	Estimated high frequency strain response	[-]
$\boldsymbol{\epsilon}_p^{LF}$	Estimated low frequency strain response	[-]
$\boldsymbol{\epsilon}_p^{QS}$	Estimated quasi-static strain response	[-]
$\hat{H}_{s,0}$	First estimate of the significant wave height for a lumped sea state	[m]
$\hat{T}_{z,0}$	First estimate of the zero-crossing period for a lumped sea state	[s]
$\mathbf{q}$	Modal coordinates $\{n \times k\}$	[-]
A	Constant from S-N curve	$[\mathrm{m}/(\mathrm{MPa}\sqrt{\mathrm{m}}^m)]$
a_k	Feed forward coefficients of a filter	[-]
a_m	Dynamic response vector, containing measured accelerations	$[\mathrm{m/s}^2]$
a_p	Dynamic response vector, containing predicted accelerations	$[\mathrm{m/s}^2]$
B	Frequency band from f_{min} to f_{max}	[Hz]
b_k	Feed backward coefficients of a filter	[-]
D	Total fatigue damage on a structural detail	[-]
$d(f)$	Data set in the frequency domain	[-]
$d(t)$	Data set in the time domain	[-]
D_i	Fatigue damage on a structural detail caused by stress cycle i	[-]
$d_{max}(f)$	Maximum value for a data set in the frequency domain	[-]
$d_n(f)$	Noisy data set in the frequency domain	[-]
$d_n(t)$	Noisy data set in the time domain	[-]
df	Frequency step of the frequency spectrum	[Hz]
dt	Time step of the time signal	[s]
E	Young's modulus	$[\mathrm{N/m}^2]$
E_t	Two dimensional Euclidian norm of a time signal	[%]
f_c	Cut off frequency for a filter	[Hz]
f_{max}	Lower bound of frequency range B	[Hz]
f_{min}	Lower bound of frequency range B	[Hz]
f_{nyq}	Nyquist frequency, defined for a bandlimited signal as $f_{min} - f_{max}$	[Hz]
f_s	Sampling frequency	[Hz]
$H(\hat{\omega})$	Frequency response of a filter	[-]
h_k	Impulse response of a filter	[-]
$H_{s,j}$	Significant wave height for element j of the scatter diagram	[m]
I_{xx}	Moment of inertia around the x-axis	$[\mathrm{m}^4]$

I_{yy}	Moment of inertia around the y-axis	[m^4]
K	The number of measurements in a time signal	[-]
KC	Keulegan Carpenter number	[-]
m	Wöhler constant	[-]
$M_{b,x}$	Bending moment, projected on the x-axis	[Nm]
$M_{b,y}$	Bending moment, projected on the y-axis	[Nm]
M_b	Bending moment	[Nm]
MAE	Mean Absolute Error	[-]
MAE_D	Mean Absolute Error for the fatigue damage	[-]
N	Number of samples in the time signal	[-]
N	The number of cycles to failure	[-]
N_i	Number of cycles to failure for stress cycle i	[-]
n_i	Number of cycles counted for stress cycle i	[-]
$n_n(f)$	Noise related to $d(f)$ in the frequency domain	[-]
P_e	Generated power	[W]
p_j	Probability of occurrence of element j of the scatter diagram	[-]
R	Resistance	[Ω]
R_o	Outside diameter	[m]
R_{in}	Inner radius of a cylindrical section	[m]
S_E	Gauge factor	[-]
S_m	Selection vector to select the active or measured DOF's	[-]
S_p	Selection vector to select the passive or predicted DOF's	[-]
T	End time of the the time signal	[s]
$T_{z,j}$	Zero-crossing period for element j of the scatter diagram	[m]
$TRAC$	Time Response Assurance Criterion	[-]
U_n	Coefficients of the Fourier transform of u_n	[-]
u_n	Filtered time signal	[-]
V_{wind}	Wind Speed	[m/s]
X_m	Complex valued coefficients of the DFT	[-]
X_n	Coefficients of the Fourier transform of x_n	[-]
x_n	Original time signal	[-]

Definition of Axis System

The axis system that is used in this report, is as defined in Figures 1 and 2. In the 3D axis system the height is measured along the z-axis. Furthermore, the x-y plane is aligned so that the y-direction is parallel to the North Arrow.

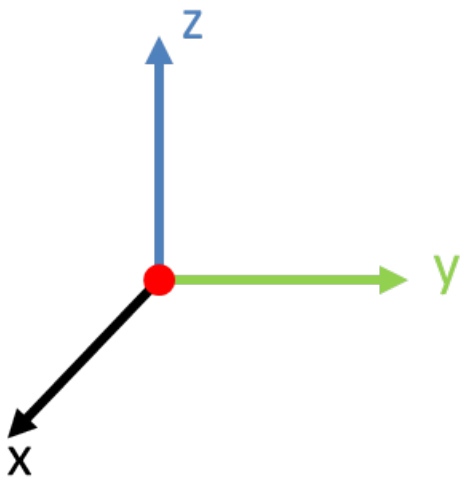

Figure 1: 3D axis system.

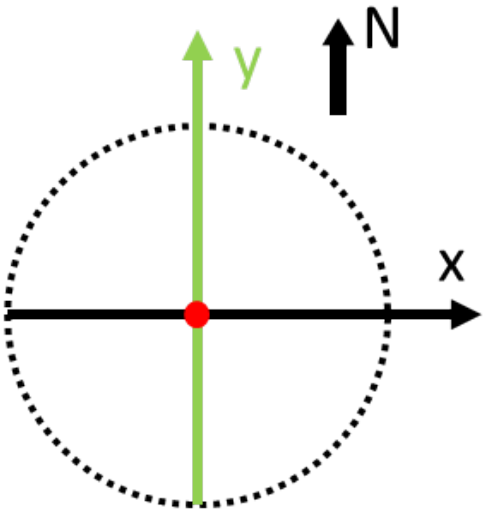

Figure 2: Axis system in the x-y plane.

Introduction

Offshore Wind Energy

A global focus on the shift to renewable energy has introduced international targets for sustainable energy production, this has strongly increased the interest in offshore wind turbines (OWT's). Although there were already several countries that had invested heavily in the construction of offshore wind farms (OWF's), in the last decade Europe has seen a surge in new projects in offshore wind. The first utility-scale OWF was installed in 2002 off the coast of Denmark and by 2015 11.2 GW of installed capacity was in operation in Europe, this represented 1.6 % of the total European power generation [24]. In 2016 this was increased to 12.6 GW, with European installations making up over 86 % of the worldwide offshore capacity [28]. The Global Wind Energy Council (GWEC) expects European offshore wind to reach an installed capacity of more than 24 GW by 2020. This increase in installed capacity goes hand-in-hand with a sharp decrease in offshore wind prices in 2016. Where in June 'Borssele 1 & 2' was won for a price of € 72,-/MWh, which was already below expectation, in the end of that year 'Krieger's Flak' and 'Borssele 3 & 4' were awarded at € 49.90/MWh and € 54.50/MWh, respectively. Finally, early in 2017 two German offshore wind projects were awarded at €0.-/MWh, meaning that the projects will not receive any subsidy. It should be noted here that the zero-subsidy farms are only due for production in 2025 and by that time the industry is anticipating a drop in costs based on technological improvements.

Figure 3: 3.6 MW Siemens offshore wind turbines at Gemini offshore wind farm.

To further decrease the cost of energy produced by an OWT, it makes sense to first identify what the largest cost items in an installed OWF are. Figure 4 displays the cost breakdown of an OWF, it shows that one of the main contributors to the capital expenditure (CAPEX) is the foundation. Thus, in this report an investigation into foundations is presented. In 2016, 88 % of the installed substructures was a monopile (MP) foundation, leading to a cumulative 81 % of the OWT's in Europe utilising MP foundations, see Figure 5. Therefore, a focus in this thesis on MP foundations is warranted.

Over time wind turbines have evolved into the biggest rotating structures on earth; Figure 6 shows the growth of rotor diameters for wind turbines in the last decades, compared to an Airbus A380 airliner. All major turbine suppliers have introduced turbines within the 8+ MW range with a diameter of around 160 m, this results in immense forces to be conveyed by the foundations. However, for wind turbines not only the highest expected force, known as the ultimate load state (ULS), is governing, the fatigue limit state (FLS) needs to be considered as well. One thing all OWT's have in common is that they are, by definition, susceptible for fatigue loading. Fatigue occurs in structures if they are subjected to repeated loading and unloading, this condition

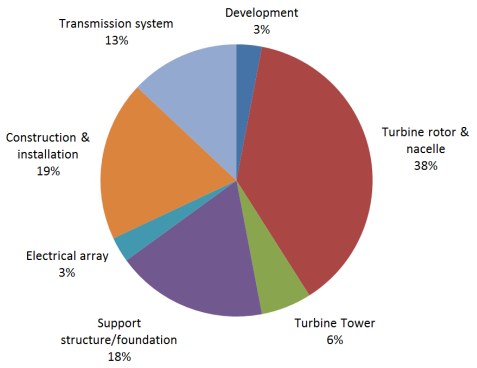

Figure 4: Total installed cost breakdown for a representative offshore wind farm in European waters (2015) [24].

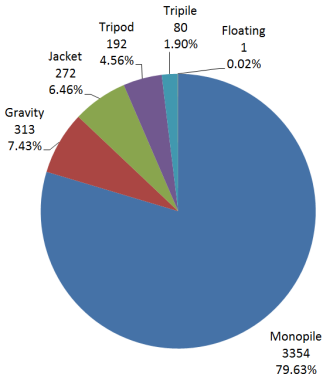

Figure 5: Cumulative share of substructure types for grid-connected wind turbines (units) in Europe [34].

is continually met in the offshore environment, where the structure is subjected to wind and wave loading. An OWT is deliberately placed in an environment where it will be exposed to as much wind as possible and since a significant part of the waves are wind induced an aggressive wave climate can be expected as well. The implications of these harsh environments in the contemporary design of support structures for an OWT are severe. As the wind and wave loading on these structures is stochastic by nature and the design lifetime is generally 25 years, there are numerous uncertainties that have to be accounted for, this results in conservatism in the fatigue load definitions in the design process.

In other words, the structure has to be operated for so long that it is not the highest load during storm conditions which drives the design costs, but it are the years of energy production and parked conditions that turn out to be the most harmful. It is said that each loading and unloading cycle causes fatigue damage to the structure and this fatigue damage is accumulated during the different phases of its life: transport, installation and operation. To better estimate the durability of foundation designs, more knowledge is required about the actual fatigue damage accumulation compared to the design values. Insights into fatigue damage accumulation behaviour could lead to optimisation in all stages of the life of an OWT. In the design phase, new information could lead to a more economical way of guaranteeing 'safe life' design. In the installation phase different techniques may applied to minimise the impact on the fatigue life in this phase. In the operational phase, there lie possibilities in the optimal utilisation of the substructure. Observations of the actual fatigue damage accumulation could enable wind park owners to continue operation even passed the original design life of the structures. Since fatigue is a stress-driven phenomenon, to gain more knowledge about fatigue damage, accurate data about the operational stresses in the support structure of OWT's is required. In this thesis two distinct methods to estimate these stresses will be investigated and compared. The first is a method based on the interpolation of strain measurements taken along the length of the MP, the second procedure depends on the use of strain and acceleration measurements in the tower and extrapolate these measurements to the foundation utilising mode shapes.

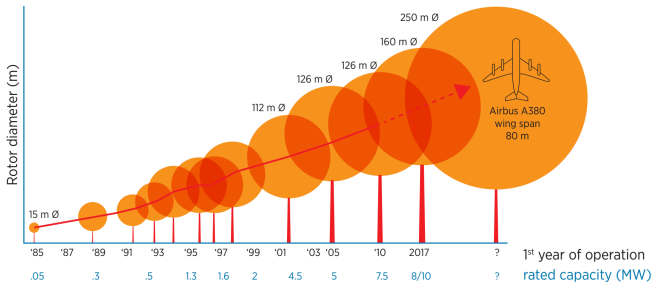

Figure 6: Growth in capacity and rotor diameter of wind turbines, 1985-2016 [51].

Van Oord

Van Oord is a marine contractor with a long history in the dredging industry, they worked on a number of well-known projects, e.g. the land reclamation for the Hong Kong airport in 1990 and the 'Palm Jumeirah' project in Dubai in 2001. However, since 2006 Van Oord started a new activity by working on the Dutch 'Princess Amalia' wind farm, the second offshore wind project came 4 years later with work for the Belgian 'Belwind' in 2010. In both these projects Van Oord's work consisted of all Ballance of Plant (BoP) activities, meaning all activities related to the construction of a wind farm, excluding the supply of the wind turbines. In 2012 Van Oord also acted as the BoP contracter for the English 'Teeside' OWF. The Van Oord business unit Offshore Wind Projects has been growing ever since and in June 2014 the offshore installation vessel 'Aeolus' was taken into operation (see Figure 7). The Aeolus was first put to work at the Dutch 'Luchterduinen' wind farm, a project Van Oord had been working on since 2013.

In the end of 2014, Ballast Nedam Offshore was incorporated in the company, which allowed Van Oord to keep more of the design process in-house, this further meant that Van Oord became owner of the heavy lifting vessel 'Svaenen' (see Figure 8) and the 'Westermeerwind' project. Ballast Nedam was a subcontractor for the German 'Baltic 1' OWF and the EPC contractor for the German 'Butendiek' wind farm, furthermore it was involved with the first Dutch wind farm, 'Egmond aan Zee'. In 2015 the new cable-laying vessel 'Nexus' was also taken into service, together with the other Van Oord equipment, this allowed Van Oord to perform the full BoP scope of a wind farm with their own vessels. The latest completed projects in which Van Oord was involved were the Dutch 'Westermeerwind' and 'Gemini' wind farms, with Gemini being one of the largest OWF's in the North Sea. For the Gemini project Van Oord was the EPC contractor and furthermore it holds a share in the completed OWF. Van Oord won some large contracts in 2016 of which the most noteworthy is the Dutch 'Borssele 3 & 4' site, in which it will act as part of a consortium together with Shell, Eneco, Mitsubishi.

Figure 7: Offshore installation vessel Aeolus.

Figure 8: Heavy lift installation vessel Svaenen.

Thesis Objective

To further reduce the LCOE for wind energy, it is of interest to investigate the fatigue damage accumulation of monopile foundations. As a foundation designer for offshore wind, Van Oord has a direct incentive to research the fatigue in the OWT foundations. Because better understanding of this topic can lead to lighter foundation designs, which may turn out to survive longer due to better knowledge of the "structural health" of the foundations. This will allow Van Oord to make more competitive designs for future wind farms. Furthermore, the estimation of in-service strains and thus stresses, necessary as input for the fatigue calculations, is relevant for the entire industry. To facilitate predictions regarding the potential of life time extension, a requirement set by Van Oord is that the accuracy of fatigue computations based on estimated stresses should be within 2 % of the control values, i.e. an accuracy of one year in the lifetime of the structure should be achieved. The objective of this thesis can be summarised as:

"Verify and compare techniques for the estimation of in-service strains in offshore wind support structures from a limited set of sensors, for use in fatigue damage monitoring."

Specifically, the multi-band Modal Decomposition & Expansion (MDE) approach will be verified by virtual

measurements. The results of the multi-band MDE (MB-MDE) will also be compared to the results from an interpolation of strain measurements.

Report Outline

In this report several topics will be covered. First, Chapter 1 will provide a literature survey on in-service stresses and sensors. Chapter 2 contains practical and theoretical consideration regarding the SFI method. Then Chapter 3 will cover the theory involved with the MB-MDE. In Chapter 4 the models utilised for this research are presented as well as a description of the generated measurements. Further, in Chapter 5 the results of the stress estimations based on the Section Force Interpolation and Multi-Band MDE will be presented. Finally a conclusion is given which is accompanied by recommendations for implementation and further research. In Appendix A environmental data is presented which normally would be found in a Basis of Design, in Appendix B design documents for the Gemini Wind Farm are displayed, Appendix C contains data referring to the FE models used to generate the measurement data, SCADA data from various load cases used to generate measurement data is displayed in Appendix D, computational tools and methods that have been used throughout this thesis are presented in Appendix E, in Appendix F the original settings used by Iliopoulos et al. are displayed and finally two complete result tables for Section 5.3 are presented in Appendix G.

1 Literature Survey

In this chapter literature is discussed that places the research presented in this thesis in context and helps form the basis of the theory presented in Chapter 2 and Chapter 3. In Section 1.1 various contributions presenting techniques for the estimation of in-service stresses are discussed, in Section 1.2 methods are presented to determine the eigenfrequencies and modes of an operational OWT and finally, Section 1.3 covers an overview of the sensors typically used for structural health monitoring.

1.1. Assessment of In-Service Stresses

In the Introduction, it was mentioned that fatigue is stress driven and thus a requirement for fatigue damage monitoring is the estimation of in-service stresses. In this review it shall be investigated what methods exist to estimate the stresses of structures during their operational life.

1.1.1. Local Strain Measurements at Hotspots

Firstly, the method described by Benedetti et al. is discussed [8] [9]. This method is based on the principle that the occurrence of a crack will cause a disruption in the stress-strain field in the structure, this principle was already proposed by Inglis in 1913 [40]. Using strain sensors this perturbation in the stress field is used to locate the crack and estimate the crack length. Then using crack growth calculations the time to failure is calculated based on the known S-N curve and the estimated initial crack.

This method is deemed to be inapplicable to the current fatigue damage monitoring problem of an OWT for several reasons. First of all, this method is aimed at very local effects as the perturbation in the stress-strain field decays rapidly. Because of the high uncertainty in the location of a crack initiation in an OWT this method would be very laborious and expensive to implement, as there are numerous hot spots to monitor. Secondly, because of the relatively short decay length of the stress perturbation, the method requires a high number of sensors to result in a good performance; every hot spot could require up to 100 sensors [9]. Finally, the theory on which the fatigue design of OWT's is performed is based on preventing the initial crack, so adhering to the safe-life methodology. The method described by Benedetti depends on the detection of an initial crack and performing a residual life analysis from that, this results in maintenance when the residual life is deemed to low, which has a closer correlation to the fail-safe methodology. Because of the gross incongruence between the applied design and assessment methodology this method is not investigated in more detail.

Other experimental methods exist to detect cracks that have already initiated. Lucena and Santos have described a method that combines time reversal and spectral elements which showed promising results for a cracked rod-like element [54]. Although this method requires less sensors than the method described by Benedetti, it is still based on the fail-safe methodology which is not applicable to OWT's.

1.1.2. Vibration Analysis

This approach is widely used in various fields of engineering and often referred to as vibration-based monitoring. There are several methods to perform the estimation of global stresses from a limited number of sensors, two methods that can be utilised are modal expansion and Kalman state estimation. A potential drawback of

vibration analysis for the calculation of fatigue damage, is the fact that most of the methods in this field make use of acceleration measurements. For fatigue the local stresses, which are related to the displacements, need to be computed, this means a double integration on the accelerations has to be implemented. Han et al. state that the "drift" problem caused by the integration induces errors in the measurements for SHM of long span bridges [30], Thong et al. and Stiros present far more detailed descriptions of this effect [84] [82]. The integration from acceleration to stress needs to be checked thoroughly, this will be discussed in Chapter 3 in further detail.

Modal Decompostion & Expansion
The main idea in modal decomposition & expansion (MDE) is to measure the response of the in-service structure at several locations and compare these measurements to mode shapes of the structure. Hjelm et al. experimented with this method in 2005, two experiments were conducted, the first was a laboratory test to confirm that stresses can be accurately computed from acceleration measurements using MDE for a control structure and known input, the second experiment was on a 20 m high lattice tower exposed to natural loads [33]. They concluded that the stress histories in a simple structure only loaded by wind can be accurately estimated. Avitabile et al. and López et al. did laboratory tests on MDE techniques and conclude that quite good agreement can be obtained between estimation and measurements [6] [4]. In modal decomposition, it is assumed that for every time step the response of a structure can be represented by the weighted summation of different mode shapes, Equation 1.1.

$$\mathbf{x} = \sum_{i=1}^{n} \phi_i q_i(t) \tag{1.1}$$

Where, x is the dynamic response, ϕ_i represents the i^{th} mode shape and q_i is the corresponding weight factor. If the response for the measured locations can be fitted to a representation by mode shapes, then implicitly that same combination of mode shapes describes the response of the entire structure. With the response of the entire structure as input, a finite element (FE) model can be utilised to obtain the stresses and thus the fatigue damage can be computed. This method was applied to OWT's, Iliopoulos et al. showed that for some cases, e.g. parked, operational at several wind speeds and an overspeed stop good results were generated [37]. However, changing operational or ambient conditions cause incongruities between estimates and measurements, also cases with misalignment of wind and waves were not reported. Maes et al. conducted similar experiments and came to agreeable conclusions, although they included strain measurements to increase the accuracy of the double integration of the acceleration [55]. From these reports it can be concluded that for specific and constant cases modal expansion is a valid technique for this application. Furthermore, the results from Iliopoulos et al. and Maes et al. are obtained by the use of only 6 mode shapes (3 for FA bending and 3 for SS bending). Here, it is assumed that it is possible to create a model that is accurate enough for this goal. The confidence in the accuracy of FE models can be increased by applying model updating techniques, Motterhead provides an introduction into model updating [63]. Model updating is performed adjusting model parameters to minimise a cost function based on mode shapes and eigenfrequencies acquired from both measurements and the FE model.

This method strongly depends on the accuracy of the modal properties used as input in the modal super positioning. Fluctuations arise in the modal properties as these are influenced by the operational conditions, e.g. temperature, wind loading. Extensive Operational Modal Analysis (OMA) should be performed to be able to correct for environmental conditions, a further discussion about OMA can be found in the subsection on *Operational Modal Analysis* of Section 1.2.

Kalman State Estimation
For linear systems it is common practice to utilise the Kalman Filter, to estimate the full state using only a limited number of sensors and a system model [44]. The filter uses a time update in which it projects the current state and error covariance estimates into the next time step, to get *a priori* estimates. Then the measurement update incorporates the new information from a measurement of the current time step into the *a priori* estimates and an improved *a posterior* estimate is obtained. Figure 1.1 displays the similarity between the Kalman filter algorithm and a predictor-corrector algorithm for solving numerical problems. An informative introduction on the Kalman Filter is written by Welch and Bishop [29]. For non-linear systems use can be made of the bootstrap filter or extensions to the Kalman filter, e.g. Extended Kalman filter, Unscented Kalman filter [27] [42] [57].

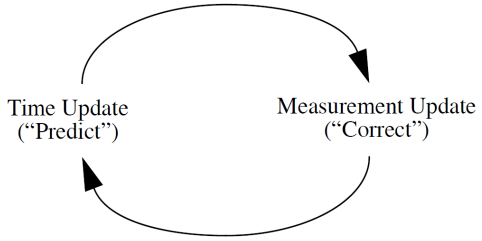

Figure 1.1: The ongoing discrete Kalman filter cycle the time update projects the current state estimate ahead in time. The measurement update adjusts the projected estimate by an actual measurement at that time [29].

There are many studies on the use of Kalman filters for vibration-based monitoring of steel structures, Papadimitriou et al. were the first to suggest using the estimated response for fatigue calculations [67].

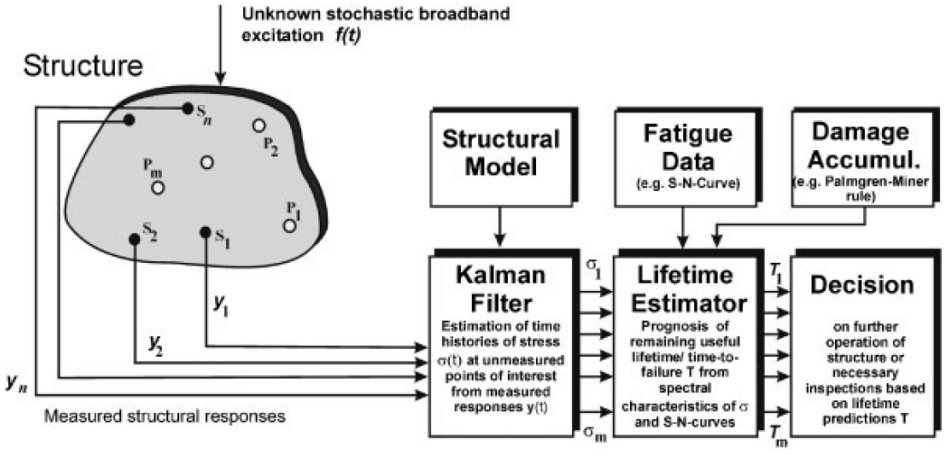

Figure 1.2: Scheme of lifetime prediction from a limited number of sensors using the Kalman Filter [67].

Multi-Metric SHM

An interesting presentation on the application of multi-metric structural health monitoring (SHM) is given by Jo and Spencer [41]. The basic idea is to combine several types of sensors, e.g. accelerometers, strain gauges, tilt sensors, to enhance the accuracy of the resulting state estimation. An advantage of this method is that the various sensor types tend to be most effective in different frequency ranges and for varying types of loading, thus when multiple types of measurements are used these can complement each other. Jo and Spencer show that for fatigue calculations significant improvement can be obtained by utilising multiple measurands. Furthermore, it is of interest to determine which measurands complement each other in such a way that the most accurate results are obtained. Palanisamy et al. performed a study on the response estimation of a bridge using strain gauges, accelerometers and tilt sensors and found that the best results were obtained with a combination of accelerometers and tilt sensors [65].

Smyth and Wu present a multi-rate Kalman filtering process to combine displacement and acceleration measurements [80]. An important aspect of this article is the fact that this filtering process allows for a difference in sample rates of the different measurands. In this study it is proven that the method is robust and effective for differing noise levels and varying relative sample rates.

Optimal Sensor Locations

The number and location of sensors for vibration analysis influence the cost and effectiveness of the system, choosing too few locations can result in inaccurate results, choosing too many is costly and can result in numerical issues regarding the Kalman filtering process. For the MDE method the number of sensors must be equal to the number of modes that are used to describe the response. Kammar presented a method of selecting the locations from a set of possible locations in an iterative manner, based on their contribution to

the linear independence of the modal partitions [45]. This method has the advantage that it gives physical insight due to the ranking of the sensor locations as well as being non-intensive in computational time. Yi et al. presented a strategy based on multiple optimisation methods which comes close to the optimal result [90]. Papadimitriou found another method based on information entropy, which refers to the amount of uncertainty in the system parameters, as a performance indicator for the sensor optimisation problem [66].

1.2. Operational Modal Analyis

It is proven that for an OWT nacelle position, rotor speed, wind speed and temperature effect the natural modes of the structure [36], thus it can be said that the operational and environmental condition influence the modal properties. Therefore, as stated in the subsection on *Modal Decomposition and Expansion* in Section 1.1.2, modal properties should be investigated under operating conditions, this can be done by spectral analysis of measurements, which will allow for estimation of the operational eigenfrequencies of the structure. In SHM the objective is to analyse measurements to obtain information about damage occurring to the structure, this means that any change in modal properties will be interpreted as damage. Sohn describes methods and research progress to normalise data sets to correct the structural changes for effects of the environmental and operating conditions [81].

Devriendt et al. performed a long-term dynamic monitoring campaign on an OWT in the North Sea, this study focuses on modal parameters of the eigenmodes corresponding to the ten lowest eigenfrequencies [18]. For this campaign a method has been developed which allows for fast implementation of a modal analysis, this enables continuous monitoring. The modal analysis tool used is known as PolyMAX [68], the data used by Devriendt et al. was collected during idling or when the turbine was parked. The study provides accurate results for the eigenfrequencies, damping ratios and mode shapes for an OWT. For operational conditions Weijtjens et al. present a method in which cases are defined (Table 1.1), then the monitoring is performed in a case-by-case process. Different modal properties are assigned to different cases to account for the varying dynamic properties. The results from Weijtjens et al. show that the stiffness of the structure increases over time [87]. This could be caused by soil stiffening, but Weijtjens does not speculate on the cause. Bhattacharya described the effect of soil-stiffening on the first eigenfrequency in his article on challenges in foundation design for OWT's [10], he notes that especially in sandy soils, soil-stiffening is to be expected. As the OWT reported on by Weijtjens et al. is located in sandy soil it is concluded that the soil-stiffening behaviour causes the increase in stiffness of the structure described in the article. It should be noted that Schafhirt et al. investigated the influence of soil parameters on the fatigue in OWT's, he found that soil-stiffening could lead to an increase in fatigue life [77], but also mentions further research and improvement of soil models are required. To resume on OMA, the Weijtjens' case-by-case approach does show promising results regarding the identification of eigenfrequencies for specific cases, but due to rotor harmonics the implementation still is difficult for the operational cases.

Table 1.1: Definition of the considered cases in the algorithm [87]

	Wind speed [m/s]		**RPM**		**Pitch angle [°]**	
	Minimum	Maximum	Minimum	Maximum	Minimum	Maximum
1: Pitch: >80	-	-	-	-	80	100
2: Pitch: +- 80	0	20	-	-	70	80
3: Pitch: +-20	-	-	-	-	19.5	20.5
4: RPM: <10	-	-	2.5	9.8	-	-
5: RPM: +-10	-	-	9.8	10.2	-	-
6: RPM: <16	-	-	10.2	15.9	-	-
7: RPM: +- 16	-	-	15.9	17	-	-
8: Cut-out	20	-	-	-	70	80

1.3. Sensors

In Section 1.1, methods were described to extrapolate or interpolate measured values to unmeasured locations. In the current section the focus will be on the sensors used to make the initial measurements. Faulkner and Hassel write about the practical issues and common practices [21], this gives some basic insight into the

measurement operations. Coronado and Fischer have written an extensive review on the state of the art of wind turbine SHM, in this contribution a useful overview of sensor producers has been included[15].

1.3.1. Strain

Strain sensors allow for accurate determination of the near static low frequency content of the dynamic response, however strain sensors do in general have a relatively high noise floor compared to other types of sensors. Two types of sensors will be discussed in this section: electrical strain gauges and optical Fibre Bragg Gratings (FBG)'s

Strain Gauges

Electrical strain gauges have been the primary means of strain measurements since the 1950's [35] [20]. Due to strain on the sensor, a metallic measuring grid is deformed and this results in a change in resistance, which can be read off as a change in electrical current trough the sensor. This relation may be defined as in Equation 1.2. Sensors can be set up in different gradations of the Wheatstone bridge, to minimise noise and compensate temperature change a full Wheatstone bridge is often applied. The output of the sensor is an electric signal that has to be amplified and translated to strain information in a data acquisition unit. Every sensor has to be connected to the data acquisition unit separately, which can lead to large quantities of cables for a fully instrumented structure. Special consideration has to be given to protect measurement points and cabling below the mudline. The most common way to apply electrical strain sensors is with an adhesive, this is a time consuming process but it does not compromise the base material. Spotwelding is possible as well, but that application is undesirable on the MP structure as it introduces faults in the primary steel. Next to the sensors the cabling has to be attached to the structure and protected as well, this can be quite a complex task for a fully instrumented structure.

$$\frac{\Delta R}{R} = S_E \epsilon_d = \Delta V \tag{1.2}$$

$$\epsilon_d = \frac{\Delta V}{S_E} \tag{1.3}$$

here, R (Ω) is the base resistance of the material, ΔR (Ω) is the change in resistance, S_E is the gauge factor and ϵ_b is the strain. More information on the workings and application of electrical strain gauges can be found in the extensive book on stress analysis using strain gauges by Hoffmann [35]. Research is being performed on new types of strain gauges implementing shunts to reduce the stress range, this development is not yet available for industrial applications however [88].

Fibre Bragg Grating Sensors

The implementation of fibre Bragg grating (FBG) sensors for strain measurement is a development that has just recently come to maturity. Instead of using electrical signals to measure strain, FBG sensors use light. The FBG can be interpreted as a filter, it reflects part of the light spectrum and transmits the rest, see Figure 1.3. If the FBG is subjected to strain, the wavelengths which are reflected change (Figure 1.4), this difference in wavelength can be measured with an optical interrogator, at the interrogator the light signal is converted to electrical signals. One of the advantages of fibre optic measurements is the utilisation of light signals, signal attenuation only has a minimally impact on these systems, thus there is no penalty for placing the data acqusition unit (DAU) far away from the sensor. Furthermore, the FBG is a passive system only relying on the light in the fibre, which means no electricity is required at the sensors, only the interrogator needs power.

$$\frac{\Delta \lambda_B}{\lambda_B} = (1 - \rho_e)\epsilon_d = \Delta V \tag{1.4}$$

$$\epsilon_d = \frac{\Delta V}{(1 - \rho_e)} \tag{1.5}$$

Here λ_b is the base Bragg wavelength of the FBG, $\Delta \lambda_b$ is the change in Bragg wavelength and ρ_e is the effective photo-elastic constant of the fibre core material [56]. Still, at this point it is difficult to find standard procedures and packaging to install FBG sensors. There has been a lot of research in the application of this type of sensors for dynamic analysis in marine environments. Sun et al. applied FBG sensors and strain gauges to a model of an offshore platform subjected to seismic loads [83]. This research proofed that FBG sensors

are superior to strain gauges with both theoretical and experimental results. Furthermore, Majumder et al. reviewed the status and applications of FBG sensors in SHM and concluded that although there are some significant benefits (lightweight, immunity to electromagnetic interference and harsh environment) they have not yet reached there full market potential due to high cost of interrogation and lack of standardisation by international governing bodies [56]. Another challenge for FBG sensors that needs to be covered before industrial application of FBG sensors is possible, is the packaging of the sensors, as the optic fibres are too vulnerable to be installed uncovered. Gangopadhyay et al. presented some deeper theoretical background and found results for different packaging materials which they compared to the standard FBG sensors and mechanical strain gauges, this led to positive conclusions regarding the presented packaging methods [25]. In 2012, Bang et al. wrote a paper on the shape estimation of an onshore wind turbine based on strain measurements from FBG sensors, the results showed the validity of FBG strain measurements as close agreement was obtained between expected and estimated shapes [7]. Mieloszyk and Ostachowicz applied FBG strain sensors on the model of an OWT tripod structure to monitor the dynamic strain caused by simulated environmental forcing [61]. Finally, it can be concluded that there are several indications that FBG's will in the near future gain market share due to the fact that they are less sensitive to noise of electrical equipment and by signal distortion due to cable length, better able to withstand the though environmental conditions of offshore SHM and less sensitive to fatigue failure [47].

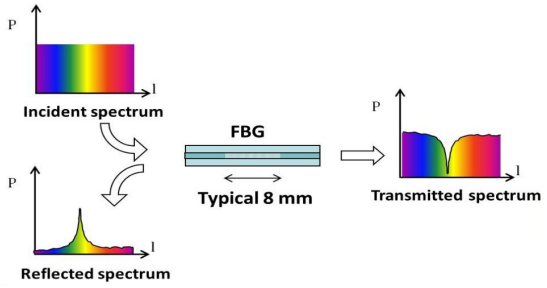

Figure 1.3: Working principle of FBG [22].

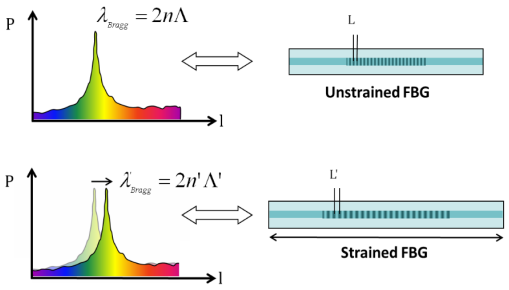

Figure 1.4: FBG response as function of strain [22].

Multiplexing

Multiple FBG sensors can be applied on a single fibre, this method is known as multiplexing. This strongly reduces the amount of cabling required. Multiplexing works because FBG sensors can be created to reflect different wavelengths, choosing wavelengths far enough from each other allows the system to measure them without getting any interference, the amount of sensors that can be applied to one fibre depends on the input spectrum and the expected offset of the peaks caused by the strain measurement. Because of the possibility to multiplex sensors the optical measurement system will lead to a dramatic decrease in cables compared to an electrical measurement system. For the sensors along the length of the foundation this leads to a smaller and lighter cable tray to protect the sensors below the mudline. The less intrusive cable and sensor protection system will especially be important during pile driving.

1.3.2. Acceleration

Accelerometers are a widely used method of measuring dynamic responses of large structures and are good at measuring the high frequency content of the response. Comparing the known acceleration due to gravity and the experienced acceleration, this type of sensor has a quite simple working mechanism [58]. According to Martinez the most common accelerometers are either piezoelectric or micro-electromechanical systems (MEMS).

Maes et al. used a combination of strain and accelerometer sensors to measure dynamic strain of an OWT monopile [55]. According to this study, accelerometers do achieve higher reliability and lower installation errors than strain sensors. Although the report also mentions the effects of the noise floor of the accelerometers multiplied with $1/\omega^4$ from the integration, clearly visible in Figure 1.5. There are several different types of accelerometers available, a selection is made based on the expected response and the requirements set for the data.

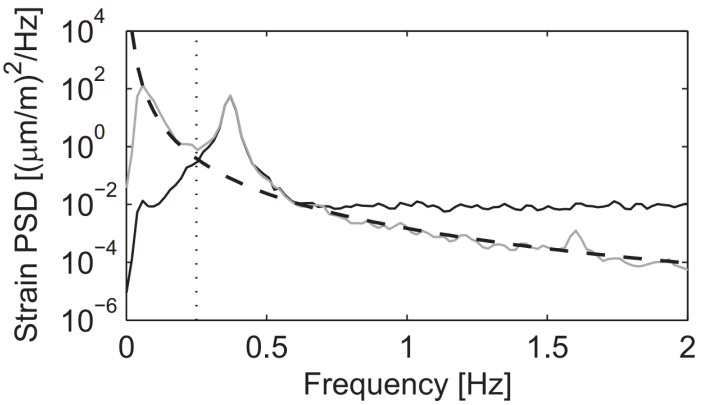

Figure 1.5: PSD of the measured (black) and estimated (gray) FA strain at level h = 19 m (parked conditions). The estimated strain is obtained from the modal expansion algorithm. The black dashed line shows a $1/\omega^4$ curve fit, in order to illustrate the influence of noise on the acceleration data [55].

1.3.3. Inclination

These sensors are often utilised in structural engineering, however in most cases implementation of tilt sensors is with quasi-static measurements in mind [85]. There are numerous ways of developing inclinometers, the most common type is a force balance sensor, which can be seen as movable mass within a casing, the displacement of the mass with respect to the casing can be related to the inclination of the sensor [91] [39].

An interesting contribution was given by Yi et al., who implemented dynamic tilt data to analyse the lowest modes of a jacket-type offshore structure [89]. The study was meant to investigate the influence of the effect of tidal changes on the modal parameters and succeeded in finding modal parameters and fluctuations related to the tides. Yi et al. were able to determine the eigenfrequencies and modal damping ratios from the dynamic tilt measurements and concluded that for measurement of signals with a low frequency content it was a viable solution.

1.3.4. Signal Acquisition & Processing

A critical part of the measurement system is the process that happens in the DAU, here the measurement signals are sent out to the signals and later processed to obtain the actual measurement data. The following topics are relevant for the data processing: sampling frequency, calibration, amplification and recording.

Sampling Frequency

Brandt describes the Nyquist sampling theorem in his book on Noise & Vibration Analysis [12], this theory prescribes the sampling frequency that is required to accurately describe an analog signal by a digital signal. Consequently, for an analog signal with a frequency spectrum that is zero outside the frequency band $B = (f_{min}, f_{max})$, the Nyquist frequency is defined as $f_{nyq} = f_{max} - f_{min}$. Then f_s is the minimum sampling frequency required to be able to reconstruct the analog signal from the frequency spectrum, where $f_s > 2f_{nyq}$. It is best-practice to run the signal through an anti-aliasing filter to ensure the spectrum is zero outside of B. For the ratio between the cut-off frequency f_c of this filter and the sampling frequency f_s a factor of 2.56 has been a standard in the field of vibration analysis [12].

For the application in an monitoring scheme for OWT's, the frequency band B is determined by the spectrum of the loading and the frequencies of the structural modes that are expected to contribute to the response. Generally, the first three bending modes in both FA and SS direction are investigated, as discussed in Section 1.1.2. The sampling parameters are related to each other as noted in Equations 1.6 through 1.8, for example there let there be a required frequency accuracy of df = 0.001 Hz and sampling frequency f_s = 50 Hz. The resulting time step dt = 0.02 s, the required number of samples N = 50000 and the measured T = 1000 s. For the structure investigated by Iliopoulos et al., the third eigenfrequency is found to be 3.910 Hz and for a sampling frequency of 50 Hz the ratio f_{max}/f_s = 12.8.

$$dt = \frac{1}{f_s} \tag{1.6}$$

$$N = \frac{f_s}{d_f} \tag{1.7}$$

$$T = N dt \tag{1.8}$$

From Table 1.2 it can be seen that sampling rates are often far higher than required by the Nyquist sampling theorem for the lower eigenfrequencies, which can be partly explained by the need for analogue filtering [19]. It can be concluded that the sampling frequency strongly depends on the structure under investigation and that the general trend in monitoring of OWT's is to choose a sampling frequency such that $f_s >> 2f_{nyq}$. The wind and wave loading spectra have their peak frequency lower than the first eigenfrequency and thus are always included.

Table 1.2: Examples of sampling rates for different studies with varying measurands.

Author	**Year**	**Study subject**	**Measurand**	**Nyquist[1] Frequency [Hz]**	**Sampling Frequency [Hz]**
Camp et al. [14]	2003	Support structure	Strain	<5[2]	40
Hansen et al. [32]	2006	Support structure	Strain	2.6	25
Damgaard et al. [16]	2013	Support structure	Acceleration	0.3	10
Shirzadeh et al. [78]	2013	Support structure	Acceleration	3.9	12.5 (5 kHz)[3]
Koukara [49]	2014	Support structure	Acceleration Inclination Strain	1.9	20
Kaufer and Cheng [46]	2014	Support structure	Acceleration Strain	3	50

1.3.5. Calibration

Most sensors that are applied in contemporary sites are calibrated sensors which can be tested during the Factory Acceptance Test (FAT). However, it is good practice to calibrate strain sensors after they have been installed, as the installation procedure can introduce pre-strain. In IEC614300-13 it is recommended to apply a quasi-static load on the structure as a way of calibration [1], these loads can be introduced as known masses or through a cable and load cell set-up. Camp et al. describe using both methods, primarily making use of the known eccentricity of the Rotor and Nacelle Assembly (RNA) mass during a 360°rotation with the RNA to compare the expected and measured strains to determine the amount of pre-strain in the sensors. Koukara et al. used a similar method of which results are plotted in Figure 2.1. Furthermore, Camp et al. used an anchor, cable, winch and load cell to check the results of the 360° RNA rotating procedure. Although they managed to obtain results it was observed that pulling on the tower with a cable was a time-intensive solution.

[1] Based on the highest frequencies reported in the respective articles.

[2] Measured frequencies were normalised, thus it is impossible to say what their maximum frequency was, however eigenfrequencies for the 1st two eigenfrequencies were presented therefore it is assumed here that the maximum frequency of import to them was lower than 5 Hz.

[3] Measured at ('x' kHz), then resampled at 'x' Hz before analysis.

Figure 1.6: Strain gauge calibration by anchor, cable, winch and load cell, operated from a barge next to the wind turbine [14].

Online Recording

For long-term measurement campaigns there are generally speaking two solutions to data transfer from the OWT to the Offshore High Voltage Substation (OHVS) either fibre optics cabling similar to the SCADA system or by long-range wifi. For new wind projects it is deemed to be the most effective to the utilise fibre optic cabling, as this system is the most reliable and there always is such a system in place for SCADA data. If a measurement campaign is started at a site where fibre-optics are not feasible, then long-range wifi is a good alternative to transfer data to a sub station where there is a cable network connection. Exchanging hard disks manually when there is maintenance scheduled is not practical for long-term campaigns, but this method may be applied in shorter campaigns on parks that are visited regularly [20].

1.3.6. Suppliers

Five suppliers have been contacted to discuss the possibilities of their measurement equipment and service: 24SEA, FBGS, FiberSail, HBM and Zensor. Both 24SEA and Zensor are spin-offs from the Belgian research platform OWI-Lab, they are small companies specialised in measurement of civil structures (24SEA is only specialised in OWT support structures). The equipment provided by these companies is off-the-shelf, but as they have several suppliers they are able to provide suitable solutions. Next to the measurement equipment, 24SEA and Zensor provide post-processing services which give insight in fatigue damage accumulation and the variation of structural parameters.

The company 'FBGS' is a cooperation between a Belgian and a German firm. FBGS mainly focuses on production of the fibres and fibre optic sensors, thus the technical knowledge on FBG's is high and this allows for customisation of the sensors to fit to the specific Van Oord requirments. A drawback of FBGS is that they prefer to be a supplier of the hardware and not provide much further service. This means that even processing the signal from the response to a strain measurement falls beyond their scope. They do provide interrogator units to readout the sensors.

FiberSail is a Portugese start-up that uses fibre optics for shape estimation. Their method is based on a strip with embedded FBG fibres, because the properties of the strip are well-known displacements of this strip can be accurately estimated. The application of the strip to a structure that is under investigation the allows for the estimation of the operational deflections of the structure. These deflections can be combined with a FE model to obtain the strains in the structure. If an accurate FEM model of the structure is available it is possible to impose the shape found from the test on the model and read out the resulting stresses.

Finally, HBM is a large German company with a lot of experience in strain measurements, especially with electrical sensors. Since having acquired the Portugese company FiberSensing in 2014, HBM also provides fibre optic measurement systems. Advantages of HBM are that they provide the entire range of products and services required for a measurement campaign. However, since they produce sensors, they have an extensive product line to choose from, but they do not facilitate the same degree of customisation as FBGS.

2

Strain Reconstruction Based on Section Force Interpolation

Chapter 1 references to several methods to estimate the operational stresses in an OWT foundation. A number of these methods are based on modal approaches where vibrational analysis is used to extrapolate the measured response from several locations to the entire structure. In this chapter however, a alternate approach is discussed, the Section Force Interpolation (SFI). This method is based on an interpolation of section forces computed from strain measurements along the length of the foundation. The goal is to circumvent any difficulties in using the correct mode shapes or errors introduced in the integration of accelerations to displacements. The first section of this chapter is dedicated to the type of sensors that are to be used, then the theory regarding the Section Force Interpolation will be discussed and the chapter will end with a short discussion on the prediction of life time fatigue.

2.1. Fiber Bragg Grating Sensors

Fibre-optic sensors have some interesting advantages over electrical strain gauges:

- Multiplexing (see Section 1.3.1)
- Small sized and lightweight cabling [56]
- Better fatigue performance of the sensor[47]

Therefore, fibre optic strain gauges should be installed. A drawback of the fibre-optic system is the relatively high cost of the interrogation unit used to send and read the optical signal. This countered by the increased likelihood of survival of sensors below the mudline. The choice of appropriate accelerometers and other sensors will be discussed with the sensor supplier.

2.1.1. Decision on Sensor Supplier

For the instrumentation of the foundation structures several suppliers were investigated in Section 1.3. After this preliminary review a selection can already be made between companies that are considered to be qualified for the task and companies that do not fit the expectations.

24SEA, Zensor and HBM have all been asked for to write a proposal for a planned measurement campaign. The decision to choose these companies is based on their experience and the fact that they provide both the equipment and the services of installation and commissioning, further more they have the knowledge to be taken on board for shadow calculation of the estimated fatigue damage accumulation. A final decision between these three companies will be based on the price estimates, the quality of the proposed systems and the confidence in logistical capabilities to complete the project in time. A remarkable difference between the suppliers is the number of FBG sensor they offer to multiplex on a single fibre, where HBM limits that amount to 13, Zensor offers 30 sensors on a single channel. It is expected that this difference originates from the expected bandwidth required by each sensor, since all optical interrogators have a measurement range

between 1500 nm and 1600 nm.

FBGS has been left out of this selection because their specialty lies with production of FBG sensors and not the service of installation and data acquisition. Although this may not be a problem for a test campaign, if larger campaigns are set up it is preferred to have supplier that can provide the aforementioned services. Fibersail, is judged not to have the right technological approach for the measurement requirements set for this project. Although their technology could be interesting to chart the long-term operational deflections of an offshore wind support structure, i.e. tower and foundation.

2.1.2. Calibration of the Sensors

In Section 1.3.5, two methods for the calibration of the system have already been presented. Pulling on the tower with a cable and load cell is deemed unfeasible by the industry and is therefore not investigated any further. The RNA 360° method is fairly common practice in the field and thus seems like a viable option, an advantage of this method is the strong visibility in the strain signal, as can be observed in Figure 2.1. This method does rely on calm weather, to allow the RNA 360° procedure and to minimise the influence of dynamic behaviour on the signal. Applying a filter so that the higher frequency signals from dynamic loading are left out could further improve the accuracy, digital filtering will be discussed in greater detail in Appendix E.4. The mean from the cable unwinding strain signal is expected to be zero, any offset in the average value indicates pre-strain in the signal. Furthermore, the phase lag between the strain measurements around the pile gives a good representation of the relative distance between the sensors and the location of the peaks and zero-crossings gives an exact representation of the orientation of the sensors. However, a drawback of this method is that is based on more or less instantaneous measurements and it is thus a snapshot of the state of the sensors. Finally, it has to be settled with the turbine supplier that the data on when a cable unwinding occurs is readily available, or that an automatic calibration run is triggered. A more detailed theoretical discussion on the relation between the bending moment, strain and loading direction is presented in Section 2.2.1.

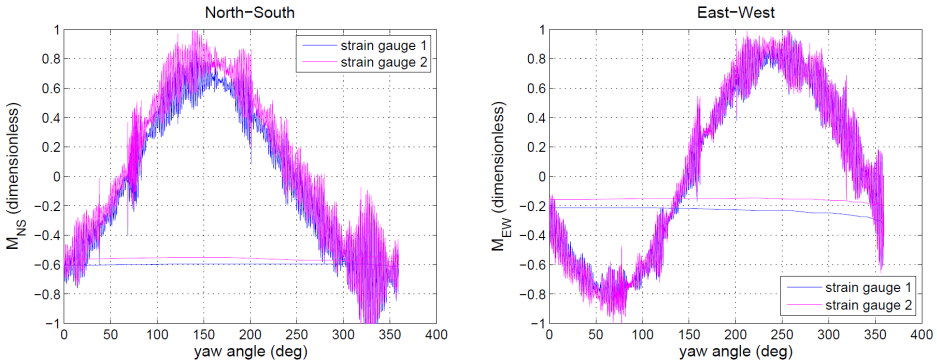

Figure 2.1: Bending moment in the North-South (left) and East-West (right) directions observed during the yaw test from the two sets of strain gauges on the transition piece. Normalised with the maximum from strain gauge 2. [49].

2.2. Section Force Interpolation

This approach is based on the interpolation of section forces which are obtained from strain measurements at different levels; subsequently interpolated section forces can be transformed into strains using basic constitutive relations from structural mechanics. The underlying assumption for the Section Force Interpolation (SFI) method, is that the moment distribution between two measurement levels can be approximated as varying linearly with the distance to the point of interest. For the conversion to moment and the interpolation the available geometry an material information of the structure are utilised. In this manner with a limited amount of measured data, insight can be obtained in the local strains and stresses at multiple hot spots.

2.2.1. Section Forces from Strain Measurements

First of all, the constitutive relations from construction mechanics prescribe that the stress in the wall of the foundation structure is caused by axial forces and bending moments:

$$\sigma_m = \frac{F_a}{A} + \frac{M_b R}{I} = \sigma_a + \sigma_b \tag{2.1}$$

Where, σ_m are the measured stresses, F_a the axial forces, the A the cross-sectional area, M_b the bending moment, R the radius of the cross-section and I moment of inertia of the cross-section. Further, σ_a and σ_b are the axial and bending stresses, respectively. The wall of the foundation structure can be assumed to be in a plane stress state as the wall thickness is far smaller than the other 2 dimensions of the plate. This means that Hooke's law can be simplified to:

$$\epsilon = \frac{\sigma}{E} \tag{2.2}$$

Here, E is the Young's Modulus. The assumption of plane stress introduces some inaccuracy due to the stress normal to plate surface that is neglected. The bending strains can subsequently be found through:

$$\epsilon_b = \epsilon_m - \epsilon_a \tag{2.3}$$

Where, ϵ_b are the bending strains. ϵ_m and ϵ_a are measured and axial strains. Furthermore, the bending moment can be computed from the bending stress by rewriting Equation 2.1.

$$M_b = \frac{\sigma_b \cdot I_{xx}}{R_{in}} \tag{2.4}$$

where M_b is the bending moment for the section at which the measurement is performed. An estimation of the bending moment at a critical height can be obtained by linear interpolation of the section forces between two measurement levels.

$$M_{b,crit} = \left(\frac{M_{b,1} - M_{b,2}}{z_1 - z_2} \right) (z_{crit} - z_2) + M_{b,2} \tag{2.5}$$

Here, $M_{b,crit}$ is the bending moment at the height of the hot spot, $M_{b,1}$ and $M_{b,2}$ are the bending moments at levels indexed with 1 and 2, respectively. Similarly z_1 and z_2 refer to the heights of level 1 and level 2, finally z_{crit} is the height of the detail. Obtaining the nominal stress $\sigma_{b,crit}$ at the critical height is now trivial.

3

Strain Reconstruction Based on Multi-Band Modal Decomposition & Expansion

As presented in the literature review in Chapter 1, there are several techniques to estimate the stresses and fatigue damage in a structure based on structural response measurements. The technique that is the focus of this chapter is the multi-band Modal Decomposition and Expansion method. The basics of the MDE technique have been mentioned in Section 1.1.2, to improve the MDE method for the application of strain estimation in OWT's Iliopoulos et al. introduced a multi-band approach to estimate the response for separate frequency bands. Finally, these separate responses are superimposed to obtain the total response for the structure [38]. This method allows sensor data to be used only in the frequency bands where they are expected to be most reliable.

In section 3.1, the algorithm for the MDE technique and its application to strain estimation is covered. Then in Section 3.2 the multi-band MDE approach for OWT's by Iliopoulos et al. is presented. Finally, in Section 3.3 the weighted least-squares algorithm is considered as extension of the least-squares algorithm in the application of the MDE method. The weighted least-squares algorithm is implemented in order to try to minimise the effect of measurement noise on the quality of the strain reconstruction.

3.1. Modal Decomposition & Expansion for Strain Response

The underlying assumption of the MDE is that the dynamic response of a structure is described by a summation of weighted contributions of the mode shapes. Equation 3.1 describes this modal superposition theory mathematically for acceleration response.

$$\mathbf{a} = \boldsymbol{\phi}\mathbf{q} \tag{3.1}$$

Where, $\mathbf{a} \in \mathbb{R}^{n_{DoF} \times k}$ is the matrix of all structural accelerations, n_{DoF} is the number of all degrees of freedom (DoF's) of the structure and k is the number of time steps. $\boldsymbol{\phi} \in \mathbb{R}^{n_{DoF} \times n}$ is the full mode shape of the structure, with n the number of participating mode shapes considered for the analysis, then $\mathbf{q} \in \mathbb{R}^{n \times k}$ is the matrix of weight factors for the modal contributions, also known as the modal coordinates. Now if for a subset of $\mathbf{a}$ measurements are available, a selection matrix $\mathbf{S}_m \in \mathbb{R}^{n_m \times n_{DoF}}$ for the measured DoF's n_m can be applied on the mode shapes $\boldsymbol{\phi}$ to obtain a matrix with the mode shape amplitudes for specific locations $\boldsymbol{\phi}_m \in \mathbb{R}^{n_m \times n}$ as presented in Equation 3.2

$$\mathbf{a}_m = \boldsymbol{\phi}_m \mathbf{q} = \left(\mathbf{S}_m \boldsymbol{\phi}\right) \mathbf{q} \tag{3.2}$$

Where, $\mathbf{a_m} \in \mathbb{R}^{n_m \times k}$ is the dynamic response vector for the n_m considered DoF's. The pseudo-inverse can be used to compute a least-squares estimate of the modal coordinates, the required matrix manipulations for the modal decomposition are presented in Equation 3.3.

$$\mathbf{q} = \boldsymbol{\phi}_m^{\dagger} \mathbf{a}_m = \left(\boldsymbol{\phi}_m^T \boldsymbol{\phi}_m\right)^{-1} \boldsymbol{\phi}_m \mathbf{a}_m \tag{3.3}$$

Here, $\boldsymbol{\phi}_m^{\dagger} \in \mathbb{R}^{n_m \times n_m}$ is the pseudo-inverse of $\boldsymbol{\phi}_m$. Once the modal coordinates $\mathbf{q}$ have been determined, the accelerations $\mathbf{a}_p \in \mathbb{R}^{n_p \times k}$ at the n_p predicted DoF's can be computed by Equation 3.4. This last step is also

known as modal expansion and allows for the prediction of all the DoF's of the structure. Similar to the selection matrix $\mathbf{S}_m$ for measured DoF's, a selection matrix $\mathbf{S}_p \in \mathbb{R}^{n_p \times n_{DoF}}$ can be established for the predicted DoF's n_p.

$$\mathbf{a}_p = \boldsymbol{\phi}_p \mathbf{q} = \left(\mathbf{S}_p \boldsymbol{\phi}\right) \mathbf{q} \tag{3.4}$$

Now that the structural accelerations at every DoF are predicted, the strains should be computed. A double integration on the accelerations is required since strains are related to displacements. It is chosen to perform this integration on the modal coordinates $\mathbf{q}$ in the Fourier domain.

$$\boldsymbol{\epsilon}_p = \boldsymbol{\phi}_{\epsilon,p} \mathscr{F}^{-1}\left\{\frac{1}{-\omega^2}\mathscr{F}\left\{\mathbf{q}\right\}\right\} \tag{3.5}$$

Where, $\boldsymbol{\epsilon_p} \in \mathbb{R}^{n_p \times k}$ are the predicted strains, $\boldsymbol{\phi}_{\epsilon,p} \in \mathbb{R}^{n_p \times n}$ are the strain distribution values for the n_p predicted locations. $\mathscr{F}^{-1}\{\bullet\}$ and $\mathscr{F}\{\bullet\}$ are the regular and inverse Fourier operators, respectively. The strain distributions, or strain mode shapes, are derived numerically by imposing the displacements from the mode shape on the structure as modelled in the finite element software. The curvature in the structure caused by the imposed modal displacements can be translated to strain through the constitutive relations of structural mechanics, Section 4.1.3 covers the extraction of the strain distributions.

3.2. Multi-Band MDE method

The concept of the Multi-Band MDE method as presented by Iliopoulos et al. is to split up the structural response into contributions of several frequency bands, namely the quasi-static (QS), low frequency (LF) and high frequency (HF) bands [38]. The response is estimated for the separate bands and superimposed to obtain the total response. The frequency bands can be observed in Figure 3.1, which shows an example of a Power Spectral Density (PSD) estimation for an OWT. The frequency bands are chosen such that they are dominated by one or several modes, for example the QS band is dominated by a static displacement mode, while the LF band mainly contains response due to the wave loading and first eigenmode, the HF band contains energy at rotor harmonics and higher eigenfrequencies.

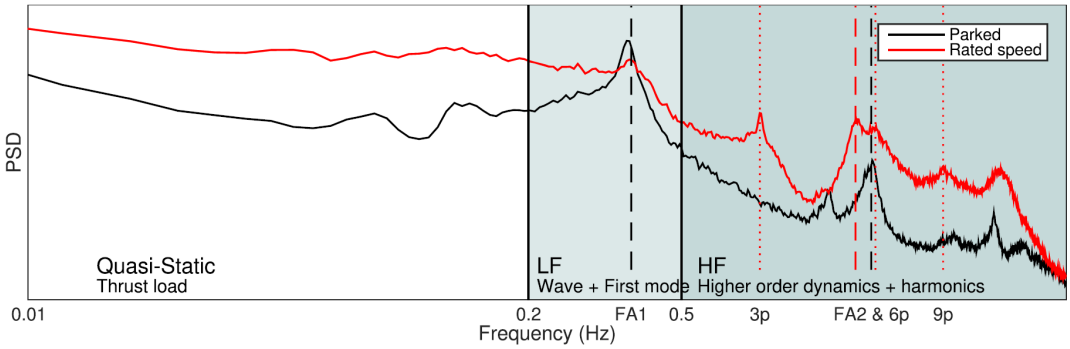

Figure 3.1: Multi-band modal decomposition and expansion uses different frequency bands to deal with different dynamics driving each band. Dashed lines indicate the structural resonance frequencies and doted lines indicate the rotor harmonics during operation at rated speed [38].

Equation 3.7 shows the computation of the LF strain contributions $\boldsymbol{\epsilon}_p^{LF}$, the contributions for the QS and HF band could be performed in a similar fashion.

$$\mathbf{q}^{LF} = \boldsymbol{\phi}_m^{LF,\dagger} \mathbf{a}_m^{LF} \tag{3.6}$$

$$\boldsymbol{\epsilon}_p^{LF} = \boldsymbol{\phi}_{\epsilon,p}^{LF} \mathscr{F}^{-1}\left\{\frac{1}{-\omega^2}\mathscr{F}\left\{\mathbf{q}^{LF}\right\}\right\} \tag{3.7}$$

Where, $\mathbf{q}^{LF} \in \mathbb{R}^{n^{LF} \times k}$ are the modal coordinates for the n^{LF} participating mode shapes for the LF band. $\boldsymbol{\phi}_m^{LF\dagger} \in \mathbb{R}^{n_m^{LF} \times n^{LF}}$ are the mode shape amplitudes for the n_m^{LF} measured DoF's and $\mathbf{a}_m^{LF} \in \mathbb{R}^{n_m^{LF} \times k}$ are the filtered measurement signals considered for the LF band. $\boldsymbol{\phi}_{\epsilon,p}^{LF} \in \mathbb{R}^{n_p^{LF} \times n^{LF}}$ are the strain mode shape values for

the n_p^{LF} predicted locations and n^{LF} participating strain modes for the LF band. The original measurement signals are filtered to obtain the separate measurement inputs for the different frequency bands, Butterworth filters are implemented to achieve this, more details on the filters can be found in Appendix E.4. Before the these filters are applied, the signal is run through a low-pass anti-aliasing (AA) Butterworth filter. As stated before, the total response can be obtained by superposition:

$$\boldsymbol{\epsilon}_p = \boldsymbol{\epsilon}_p^{QS} + \boldsymbol{\epsilon}_p^{LF} + \boldsymbol{\epsilon}_p^{HF} \tag{3.8}$$

The motivation for this approach is that accelerometers perform well for the dynamic structural response (LF and HF bands), but produce measurements that are only just above their noise floor for the QS band. As the $1/-\omega^2$ operation would strongly amplify the measurement noise in this band (see Figure 1.5), Iliopoulos et al. present a solution where the QS response is predicted based on strain measurements and strain mode shapes. The computation of $\boldsymbol{\epsilon}_p^{QS}$ is performed according to equation 3.10. Only the LF and HF bands are based on acceleration measurements, there will be no noise from low frequencies due to the band pass filters. Therefore the result of the integration in the frequency domain will be very accurate for the LF and HF bands.

$$\mathbf{q}^{QS} = \boldsymbol{\phi}_{\epsilon,m}^{QS,\dagger} \boldsymbol{\epsilon}_m^{QS} \tag{3.9}$$

$$\boldsymbol{\epsilon}_p^{QS} = \boldsymbol{\phi}_{\epsilon,p}^{QS} \mathbf{q}^{QS} \tag{3.10}$$

Further, it was chosen to define two dynamic bands, i.e. the LF and HF band, since the accelerometer at the top of the tower is essential for the estimation of response at the 1$^{\text{st}}$ eigenfrequency and thus the LF band. However, as the sensor is close to the nodal point of the higher eigenmodes, its output at the related eigenfrequencies would be strongly contaminated with measurement noise. As measurement noise could be decomposed into the modal coordinates, Iliopoulos et al. chose to define different sensor arrangements for the LF and HF bands.

3.3. Weighted Least-Squares

In the least-squares estimation of the pseudo-inverse, it is assumed that every input has the same variance in its errors. Often this assumption is violated and thus not all data points provide equally accurate information, this means that the decomposition of the modes is corrupted. One way to increase the accuracy of the estimation is by introducing the weighted least-squares estimator. Here, the variance of the errors is estimated to a proportionality constant and the inputs with lower error variance are given more importance in the solution. In Equation 3.11 a weight matrix is introduced, apart from that the same matrix manipulations are applied as in Equation 3.3.

$$\mathbf{q}(t) = \left(\phi_{\mathbf{a}}^{\mathbf{T}} \mathbf{W}_\epsilon \phi_{\mathbf{a}}\right)^{-1} \phi_{\mathbf{a}}^{\mathbf{T}} W_\epsilon \mathbf{a}_{\mathbf{a}}(t) \tag{3.11}$$

Where, $W_\epsilon \in \mathbb{R}^{n_a \times n_a}$ is the diagonal weight matrix that distributes the importance given to the different inputs. Ideally, the weight matrix is set up according to $w_i = 1/\sigma_i^2$, with w_i the weight and σ_i^2 the variance of the error of input i. Although the exact variance of the errors is often unknown, an estimate of the variance can still be used to increase the accuracy of the final solution. Based on input signals corrupted with measurement noise, estimations of the error variance give an indication of the accuracy of each measurement signal. The information about the accuracy of the input can be taken into account in the modal decomposition, reducing the influence of inaccurate sensor data and improving the quality of the strain estimation.

4

Numerical Modelling & Data Generation

The SFI and MDE method, presented in Chapter 2 and 3 respectively, will be verified and compared using simulated measurement data for several different load cases. Several load cases are investigated because of the expected difference in dynamic behaviour of the structure under varying operational conditions. The data is simulated using an FE model which is constructed according to the design specification of a turbine foundation in the Gemini Wind Farm. One of the driving reasons behind this choice is the fact that Van Oord has partial ownership of the wind farm and thus the model can be based on the design documents generated by Rambøll. Relevant information on the structural design, consisting of the structural design data and soil information can be found in Appendix B and the Design Basis [69].

The first section of this chapter describes the 1D modelling of the tower and foundation structures, two models are introduced: the first is used as a benchmark study to verify the model against the design made by Rambøll; the second model is slightly adjusted so that it can be used in the main analysis presented in this work. In Section 4.2 an overview of the models utilised for the environmental loads caused by wind and waves is given. The chapter is concluded with a section that discusses the different load cases that were tested in this thesis and the simulated measurements.

4.1. 1D Beam Models

For this thesis, one tower and foundation geometry has been taken into account, which has been based on Gemini turbine *Zee Energie C5*, also known as ZEC5. Two versions of this geometry were created in ANSYS, they were constructed to have different RNA properties, one had the characteristics of the Siemens 4 MW and the other of the NREL 5 MW turbine. The models were generated using the Van Oord in-house design tool for FE models of monopile foundations and according to the Gemini design produced by Rambøll. The goal of constructing the first model was to verify it against the Rambøll design, introduce the modelling method and ensure a realistic set of modal properties was obtained. The second model was used in the ANSYS time domain analysis for combined wind and wave loading. Since the wind loads were generated in Bladed and there was no Bladed model for the Siemens 4 MW turbine available, it was decided to recreate an identical tower and foundation geometry in Bladed, but equip it with the NREL 5 MW turbine. The turbine loads generated in Bladed for this model were subsequently used as input for the ANSYS time domain analysis. First the model with the Siemens 4 MW turbine is presented, then in Section 4.1.2 the model for the NREL 5 MW machine is discussed.

4.1.1. ZEC5 - Siemens 4 MW

The model used for the benchmark study of the FE modeling method is presented here, Figure 4.1 shows the schematic beam model that is used to represent the OWT in the computer model. As can be observed point masses are used to model internal equipment and platforms; springs are implemented to model the response of the soil to displacement of the structure.

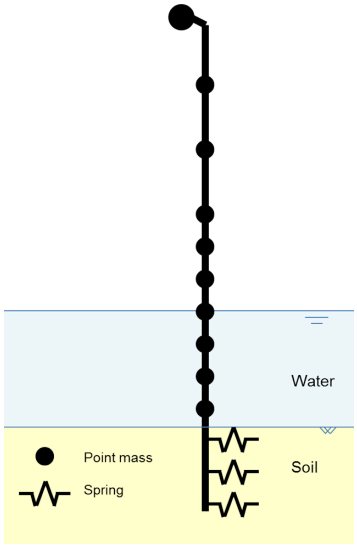

Figure 4.1: Schematic representation of the beam model utilised for the global stresses and modal analysis.

Geometry
The monopile design of the Gemini wind farm exists out of two cylindrical sections that are connected by a conical section. The bottom diameter is 7 meter and the top diameter is 5.5 meter. The detailed information about the design is presented in the relevant technical drawings contained in Appendix B.1 and B.2. The monopile and the transition piece have been assembled with a bolted connection, next to the bolted connection there is a concrete skirt overlapping the monopile over a length of 7.6 m. The concrete skirt barely affects the stiffness of the structure and is mainly there to support attachments, e.g. boat landing and ladders. The grout also distributes the stresses in the TP and MP during small boat impacts and serves as corrosion protection. It is however important to account for the weight of the concrete skirt [72]. Relevant added masses have to be added to the model to represent internal or external attachments or equipment.

Furthermore, the tower and the rotor and nacelle assembly (RNA) have to be accounted for to obtain the proper eigenfrequencies for the structure. In this case the data is taken from the Tower Design document drafted by Siemens [79]. The tower has a bottom diameter of 5.5 meter and has 2 cylindrical sections on which a conical upper section is positioned, the top diameter is just over 3 meter, the details of the tower design can be found in Appendix B.1. It is important to take the correct top and internal masses into account, the RNA is accounted for by an eccentric point mass of 237 metric ton with a moment of inertia representative of the actual RNA. In the tower there are several internal components and flanges that are represented by added point masses as well. An overview of some basic dimensions is given in Table 4.1.

Table 4.1: Dimensions of the support structure

	Length [m]	**Diameter [m]**		**Wall thickness [m]**		**Ratio D/t [-]**		**Weight [mton]**
		Top	**Bottom**	**Top**	**Bottom**	**Max**	**Min**	
Part	**l**	$\mathbf{D_{top}}$	$\mathbf{D_{bot}}$	$\mathbf{t_{top}}$	$\mathbf{t_{top}}$			**W**
Pile								
Transition piece								
Tower								

ANSYS Structural Modelling
The model is now constructed in ANSYS with beam elements of type pipe288, which have 6 degrees of freedom at each node; 3 translations and 3 rotations. The physics of the elements are predetermined by Timoshenko's beam theory[5]. For the tower structure nodes are defined according to the levels defined in Appendix B, Figure B.1. The foundation nodes, from interface level down, are defined along the z-axis at a 0.5 m

interval. One node defines the nacelle, accounting for its weight and inertia. Pipe elements are defined between consecutive nodes and have attributes corresponding to the design by Rambøll and Siemens. For every element the following attributes are defined:

- Pipe diameter (outer)
- Wall thickness
- Number of cells around the circumference
- Number of cells through the pipe wall
- Internal fluid
- External material
- Thickness of external material

For conical sections an average pipe diameter is taken, similarly wall thickness is taken to be constant over the element length. Added mass of the water for the element, is implemented as a concentrated mass at the nodes, the grout and steel mass of the overlapping TP are also modelled as point masses at the nodes. The material types used in the model are defined in Table 4.2. The 1D ANSYS beam model presented here is utilised in the modal analysis to compare the Van Oord and Rambøll approaches

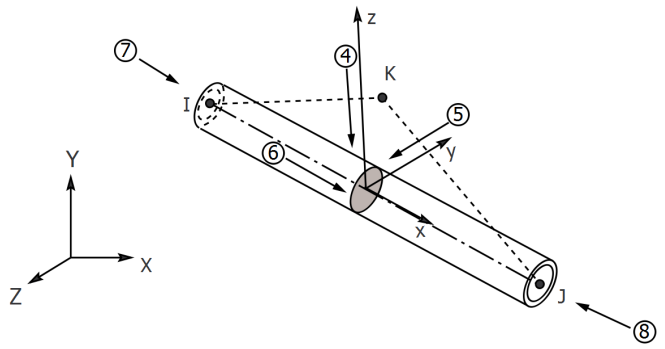

Figure 4.2: Geometry and axis system of the PIPE288 element from ANSYS [5].

Table 4.2: Materials in the 1D beam model.

Material	**Young's Modulus [GPa]**	**Poisson's ratio [-]**	**Density [kg/m^3]**
Steel	210	0.3	7850
Grout	55	0.19	2500
Water	-	-	1025

Soil Model

The soil model utilised by Rambøll is presented in Figure 4.3, here the non-linear P-y spring represents horizontal loading mechanism and the T-z and Q-w springs represent vertical loading mechanisms. In the Van Oord model non-linear P-y curves are used to represent the lateral effects of the soil stiffness. These springs are applied as point actuators but actually imitate the influence of half-meter intervals of soil. Furthermore, in the Van Oord model, as used in this thesis, no vertical springs are assigned as the vertical loading mechanism is simplified by setting the vertical displacement at the pile toe to be zero. For the current study, this is assumption is valid as the horizontal component is dominant in the dynamic loading that is being investigated. It is assumed that the bearing capacity of the soil suffices for the foundation loads.

One challenge that had to be resolved was the incongruity between the soil model regarding the horizontal loading applied by Rambøll and the one used by Van Oord. Rambøll specifies P-y curves at the top and bottom

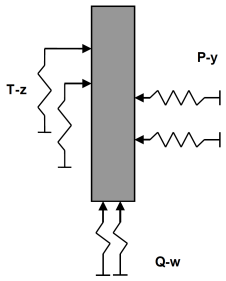

Figure 4.3: Soil Model employed by Rambøll for their computer model [74].

of each layer and assumes linear varying soil stiffness in between [74], then the Rambøll model actually uses a fine spacing between the defined horizontal springs to simulate a continuous soil. Van Oord uses a soil model in which the springs are defined every 0.5 m, this means an interpolation has to be performed on the soil data presented in the Attachment Report by Rambøll [71]. Figure B.6 in Appendix B displays the P-y curves as generated by Rambøll at the top of every soil layer, in Figure B.7 the interpolated results are shown.

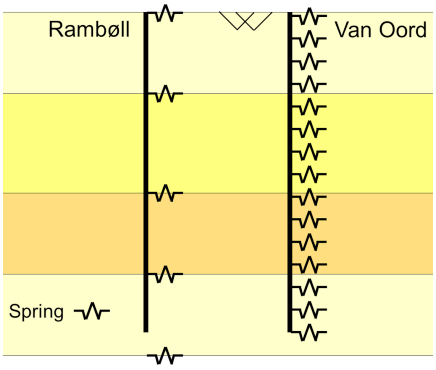

Figure 4.4: Schematic representation of the difference in soil modelling between Rambøll(left) and Van Oord(right).

The Van Oord model is set up to accommodate a toe shear spring, this spring can be set up utilising the pile toe depth and the soil information provided by Rambøll [71]. Even more, soil damping can also be implemented in the Van Oord model, in the design documents provided by Rambøll no mention is made of soil damping. To match the results with the Rambøll model, both the toe shear spring and the damping are turned off.

Model Verification

To ensure that the constructed models have been set up properly with the help from the Rambøll design documents, a comparison is made between the resulting eigenfrequencies of the current model and the documented frequencies. The eigenfrequencies and mode shapes can be determined by solving the eigenvalue problem. The general form of this problem is presented in Equation 4.1. To solve this problem the mass and stiffness matrices $\mathbf{M}$ and $\mathbf{K}$ have to be known, these can be set up if the characteristics of the materials, geometry and masses of the structure are known.

$$\left(\mathbf{K} - \omega^2 \mathbf{M}\right) \boldsymbol{\phi} = \mathbf{0} \tag{4.1}$$

Here, $\boldsymbol{\omega}$ is a vector of the eigenfrequencies and $\boldsymbol{\phi}$ is the matrix of eigenvectors. First, The frequencies of the tower structure are compared to the frequencies provided by Rambøll [73]. In Table 4.3 the first eigenfrequencies of the tower, clamped in at interface, in both the for-aft and side-side direction are noted for both models. The values seem to correspond well, this is to be expected as the input is defined by well-known material parameters and the original tower geometry developed by Siemens. When the substructure is taken into account as well, the problem becomes far more complicated as the dynamic effect of the water and soil have to be taken into account as well. As different models for the soil are applied, it is harder to obtain a perfect match for the higher eigenfrequencies. The results of the eigenfrequency analysis are presented in Table 4.3, a good match is obtained for the first eigenfrequency with an error smaller than 0.05 %, for the third eigenfrequency the error builds up to about 1.37 %. As the eigenmodes are not reported in detail in the Rambøll

design documents these cannot be compared to the current design. Thus proof of similarity of the models will have to be provided by a proper match of the eigenfrequencies. The mode shapes of the Van Oord model have been read out from ANSYS, where they were calculated in the modal analysis of the support structure for the Gemini location ZEC5. Figure 4.5 gives an overview of the first four mode shapes in the for-aft (FA) and side-side (SS) direction. The figure also shows quasi-static shapes, these are not mode shapes, but will be used to approximate the response due to the quasi-static loads. Two types of quasi-static modes are defined, one due to a point force acting at the upper tower node and one due to a moment applied to the upper node.

Table 4.3: Eigenfrequencies [Hz] of the modelled structure (only the first five frequencies were documented by Rambøll). Top: RNA & Tower ,Bottom: full structure[73].

RNA & Tower			
Eigenfrequency	**Van Oord**	**Rambøll**	**Difference [%]**
1st (side-side)	0.500	0.501	0.200
1st (for-aft)	0.511	0.512	0.195
Full Structure			
1st (side-side)	0.2891	0.2892	0.035
1st (for-aft)	0.2906	0.2907	0.021
2nd (side-side)	0.8097	0.8037	-0.752
2nd (for-aft)	0.8219	0.8219	-0.951
3rd (side-side)	1.2391	1.2563	1.369

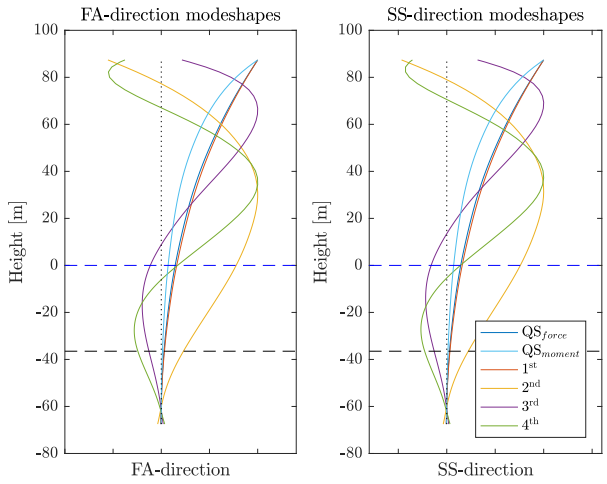

Figure 4.5: Mode shapes of the OWT support structure based on the Gemini foundation design. Left: mode shapes in the for-aft direction, right: mode shapes in the side-side direction

4.1.2. ZEC5 - NREL 5MW

The time domain analysis for wind and wave loading was run with this model, which matches in both foundation geometry and turbine characteristics with the Bladed model, that was used to obtain the hub loads due to the wind loading on the turbine. Furthermore, in both Bladed and ANSYS the nodes and elements have been defined with exactly the same coordinates, dimensions and added masses. In Appendix C a short overview of the turbine definition can be found, as well as the mass totals of both the Bladed and ANSYS models.

Some small adjustments to the set-up of the structural model are made. Firstly, the RNA is represented by two nodes, one for the rotor and one for the nacelle. Furthermore, the very short elements representing the flanges in the original tower design by Siemens have been removed and their length has been added to the neighbouring elements, this has removed high peaks in the strain distributions at these nodes, but did not

noticeably impact the dynamic characteristics of the structure .

Verification

A similar method of verification is implemented here as was utilised in Section 4.1.1. Firstly the eigenvalues for the structure are compared if the structure is clamped in at interface level, then the values for the full structure are computed, the results can be found in Table 4.4. Computing the eigenfrequencies and mode shapes is straight forward in ANSYS and follows the concept presented in the subsection on *Verification* in Section 4.1.1. For the Bladed eigenfrequencies and mode shapes, the system identification technique Frequency Domain Decomposition (FDD) was implemented [13].

Table 4.4: Eigenfrequencies [Hz] of the modelled structure. Top: RNA & Tower, Bottom: full structure

RNA & Tower			
Eigenfrequency	**ANSYS**	**Bladed**	**Difference** [%]
1^{st} *(side-side)*	0.412	0.425	3.198
1^{st} *(for-aft)*	0.420	0.430	2.717
Full Structure			
1^{st} *(side-side)*	0.231	0.240	3.681
1^{st} *(for-aft)*	0.233	0.240	3.195
2^{nd} *(side-side)*	0.698	0.787	12.730
2^{nd} *(for-aft)*	0.710	0.800	12.609
3^{rd} *(side-side)*	1.565	2.373	51.600
3^{rd} *(for-aft)*	1.740	2.373	37.152

To check if the combined model of turbine and support structure does not resonate too much the frequency range of the external loading is compared with the first two natural frequencies of the structure. In Figure 4.6 an overview of the results is presented, here the eigenfrequencies are shown with a margin of 10 % in both directions.

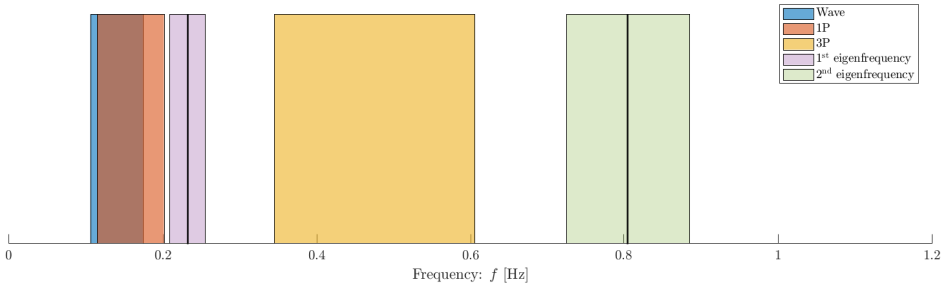

Figure 4.6: Relevant frequency bands for the structure below 1 Hz.

4.1.3. Strain Mode Shapes

A Strain mode shape is the strain distribution in a structure due to a static deformation corresponding to a specific mode shape of the structure. These strain mode shapes can be used to estimate strain in the structure by multiplying the strain mode shapes with the corresponding modal coordinates, e.g. if the modal deflections for the first mode shape are known, the strain related to these deflections can be computed by multiplying the the modal coordinates for the first mode shape with the strain mode shape. In other words, the modal strain distributions are used to estimate the strain, similar to the estimation of structural deflections through mode shapes, as was mentioned in Section 3.1. The strain distributions are derived numerically by imposing the displacements from the mode shape on the structure as modelled in the finite element software. The model and mode shapes are described in the previous sections, the strain distributions are displayed in Figure 4.7 and 4.8. The strain distributions have been plotted alongside the D_o/t ratio of the structure over

the height, this gives insight in the expected discontinuities in the strain distributions. The elastic bending strains are found from the ANSYS element solution by Equation 4.2.

$$\epsilon_{B,y,T} = -\kappa_y R_o \tag{4.2}$$

Which may be derived from the constitutive relationships in Equations 4.3, 4.4 and 2.2.

$$M_y = \frac{EI_{yy}}{\kappa_y} \tag{4.3}$$

$$\sigma_y = -\frac{ER_o}{\kappa_y} \tag{4.4}$$

Where $E_{B,y,T}$ is the elastic bending strain on the positive y side of the element, κ_y is the curvature around the y-axis and R_o is the outside diameter of the element. Here, a local axis system is implemented, which differs from the general axis system, the local axis system that is implemented here is presented in Figure 4.2.

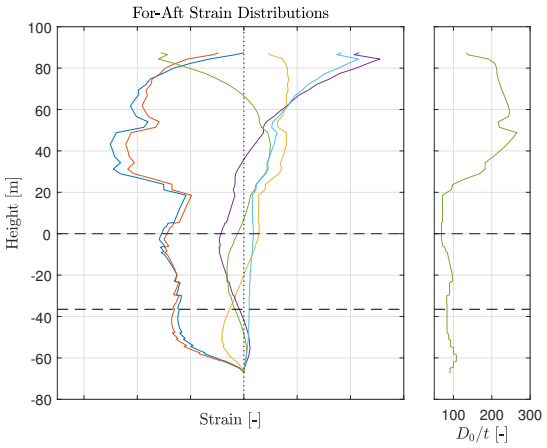

Figure 4.7: Strain distribution for the F-A mode shapes, the distributions presented here computed for the ANSYS model. Computed from displacements related to mode shapes similar to the shapes presented in Figure 4.5.

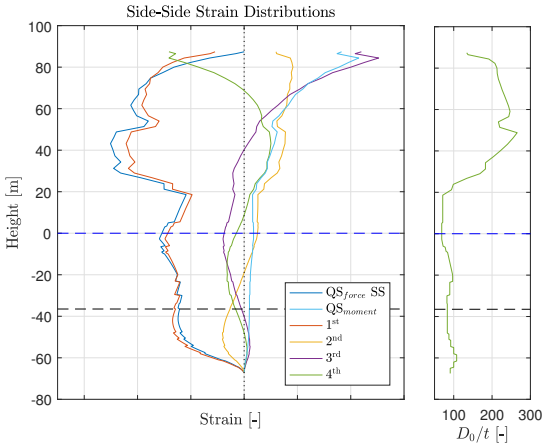

Figure 4.8: Strain distribution for the S-S mode shapes, the distributions presented here computed for the ANSYS model. Computed from displacements related to mode shapes similar to the shapes presented in Figure 4.5.

4.2. Modelling Wind and Wave Loading

This section covers a brief overview of the modelling of the environmental phenomena. In Section 4.3 the specific parameters for each load case (LC) are defined. The blade element momentum (BEM) and actuator disk theories are used to compute the structural response to wind loading, a detailed introduction to these theories and the application to wind turbines can be found in the book on turbine aerodynamics by Hansen [31]; the Morison equation is applied to calculate the response to the wave loading.

4.2.1. Wind

The computer program GH Bladed 4.6 was used to calculate the time-varying wind fields and obtain the hub loads for several LC's. According to the Bladed Theory Manual, the implemented theories are based on the method for wind simulation reported by Veers and the Kaimal turbulence model [11] [86] [43]. The wind velocity that is used to calculate the aerodynamic loads is given by an average wind speed on which a turbulence spectrum is superimposed. The turbulence can be modelled as dimensionless wind speed deviations. As described by Veers the turbulence field may be defined by autospectral density and the coherence function. The implementation of the Kaimal turbulence model was performed according to the IEC standard 61400-1 edition 3 [43] [2].

4.2.2. Waves

The hydrodynamic loads modelled are the result of a random wave, i.e. a summation of several regular Airy wave components with random phases. The amplitudes and frequencies of the wave components are defined

by the JONSWAP spectrum, which gives a distribution of wave frequencies for a given significant wave height H_s and wave period T_p, further the peak enhancement factor γ defines the steepness of the spectrum. Finally the wave components are found by dividing the area under the spectrum in strips, such that all strips have an equal area, 200 wave components were used. Furthermore, Wheeler stretching is applied to approximate the wave kinematics above the mean water level (MWL).

4.3. Simulated Structural Response

Due to the lack of actual measurement data for OWT's available for this thesis, an approach was sought to generate virtual measurements that contained frequency content similar to what is expected for offshore conditions. Chosen was to work with the computer program GH Bladed, which is an integrated software package for wind turbine efficiency and loading calculations. Because the program is able to implement aero-elastic coupling, wave loading and soil response, it is often used to simulate the response for OWT's in an offshore environment [17]. During the operational lifetime of the OWT many different LC's occur. In the design phase these are represented by Design Load Cases (DLC's), which are commonly taken from the IEC design code for OWT's [2].

As presented in Section 1.2, Weijtjens et al. suggested a method where the OWT is analysed in a case-by-case method, the cases are presented in Table 1.1. Thus, several LC's are run, because of the interest in how the changing dynamics under different environmental conditions affect the strain and response estimation. In Table 4.5 the LC's are presented alongside the parameters chosen for the modelling of the environmental loads. In Appendix D the SCADA data for the different LC's is presented. In general all LC's will be treated as if wind and waves are aligned, for Load Case 5 both an aligned (LC 5) and misaligned (LC 5_m) case are considered. For the misaligned case the waves will be modelled under an angle $\theta_{wave} = 15\,°$. For the current research no directional wave spectrum was implemented, thus the waves are modelled as if they were unidirectional. The locations for data read-out points are presented in Figure 4.9, here the detail names refer to the boat landing stub (BB1A), circumferential welds (CWxx) and the cable entrance hole (MPCH). The data from the "sensor" locations is used as input in the algorithms and the data generated for the "control" nodes are kept as control values.

Table 4.5: Definition of the considered test cases in for which data was generated.

	Case Definitions						**Load Cases Specifications**					
	v_{wind} *[m/s]*		*RPM*		*Pitch [°]*		V_{wind} *[m/s]*	*TI [%]*	H_s *[m]*	T_p *[s]*	Peakedness *[-]*	θ_{wave} [°]
	min.	max.	min.	max.	min.	max.						
1: Idling	0	4	0	0	80	100	2	29.2	1.07	6.03	1	0
5: RPM +- 9	7.5	8	8.8	9.2	0	0	8	16.0	1.31	5.67	1	0
5_m: RPM +- 9	7.5	8	8.8	9.2	0	0	8	16.0	1.31	5.67	1	15
7: RPM +- 12.1	19	21	11.9	13	16	19	20	13.4	2.76	6.99	1	0
8: Cut-Out	25	-	-	-	89	91	28	11.9	4.17	8.49	1	0

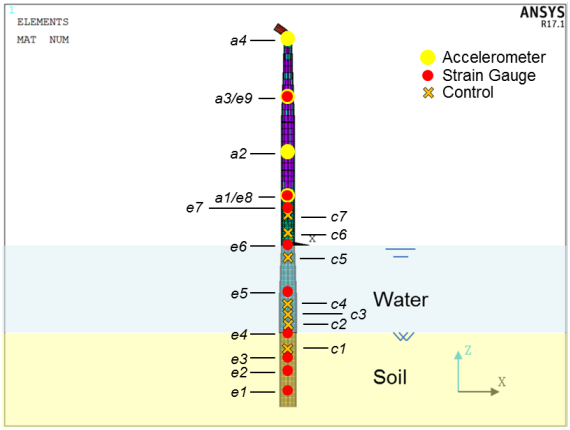

Figure 4.9: Read-out locations along the structure, circles represent "sensors" and crosses mark the "control" locations. Yellow circles imply accelerometers and red circles are strain sensors.

Table 4.6: Definition of the sensor and control levels presented in Figure 4.9

	Sensors Levels			
Notation	**ANSYS node**	**Height [m]**	**Acceleration**	**Strain**
e1	1448	-60		x
e2	1428	-50		x
e3	1420	-46		x
e4	1401	-36.5		x
e5	1174	-18		x
e6	1138	0		x
e7	1106	16		x
a1/e8	1101	18.6	x	x
a2	1023	31.24	x	
a3/e9	1010	66.831	x	x
a4	1001	87.4	x	

	Control Levels		
Notation	**ANSYS Node**	**Height [m]**	**Detail Name**
c1	1423	-47.5	CW36
c2	1204	-33	MPCH
c3	1197	-29.5	CW24
c4	1178	-20	CW18
c5	1144	-3	CW08
c6	1128	5	CW11
c7	1121	8.5	BB1A

4.3.1. Data: Bladed vs. ANSYS

Bladed was used to obtain data for the structure under the presented load cases, however the MDE requires the exact mode shapes to be known and these could not be properly obtained from Bladed, due to the sub-structuring technique implemented in the software and thus it was chosen to introduce a work-around. In an effort to stay as close to reality as possible, hub loads were taken from GH Bladed, based on the load cases defined in Table 4.5. The hub loads from Bladed were read out as time series of moments and forces in both x- and y-directions in the global axis system. These were subsequently implemented in the ANSYS 1D beam model, where also a random wave was introduced according to the load case parameters. In this manner 10 minute time series, with a 50 Hz sampling rate, were produced. The first 30 seconds were disregarded due to transient behaviour caused by the start-up effects of the transient ANSYS solution. As the mode shapes from the ANSYS model were fully available, the data from the ANSYS transient solution allowed the estimation with the MDE to be performed with matching mode shapes, thus minimising the model error in the algorithm. In Figures 4.10 and 4.11, examples of the generated data are given. Figure 4.10 displays the time history of the for-aft acceleration of the top tower node for a mean wind speed of 8 m/s (LC 5). Figure 4.11 shows the for-aft and side-side accelerations of the top tower node set out against each other for the investigated load cases, this gives an idea of the 3 dimensional nature of problem investigated in this thesis.

As data is generated for both Bladed and ANSYS, a comparison was drawn between the frequency content of the signals. Because of the random nature of the signals, it is difficult to compare the two methods in the time domain. Therefore, the signals were compared by investigating their Power Spectral Density (PSD) as this allows the inspection of the amount of energy located at a certain frequency, more information on the PSD can be found in Appendix E.4. Figures 4.12 and 4.13 show the PSD's for the Bladed and ANSYS data, respectively. Inspecting the figures, some clear similarities as well as a couple of differences become apparent. Firstly, we can see that in both cases the 1st three eigenmodes are triggered and there seem to be small peaks in the PSD at multiples of the 3P frequency, which indicates influence from the rotor rotation. Furthermore,

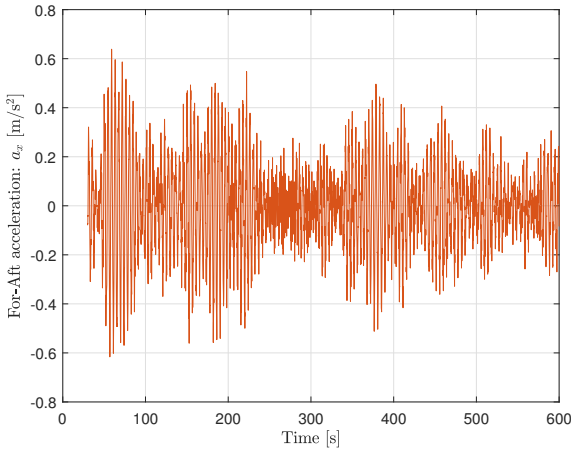

Figure 4.10: Time history of the for-aft acceleration of *Node 1001* (87.4 m) for LC 5.

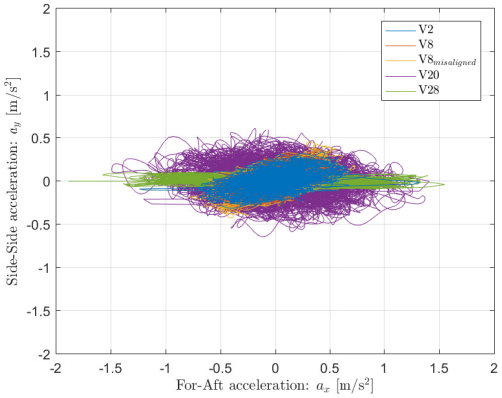

Figure 4.11: For-aft and side-side accelerations of *Node 1001* (87.4 m), plotted against each other for all the investigated LC's.

there is a clear difference in the tail of the PSD's as for the Bladed data, a clear distinction between the four wind speeds can be observed, this is related to the turbulence fields that are introduced. Each turbulence field corresponds to a specific wind speed. The ANSYS data suggests that the turbulence has not been fully transferred in by the use of Bladed hub loads.

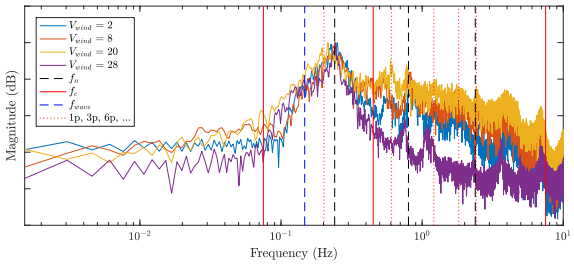

Figure 4.12: normalised PSD's of the Bladed data for several wind and wave conditions, the presented PSD's are for the acceleration at the top tower node (*Node 1001*).

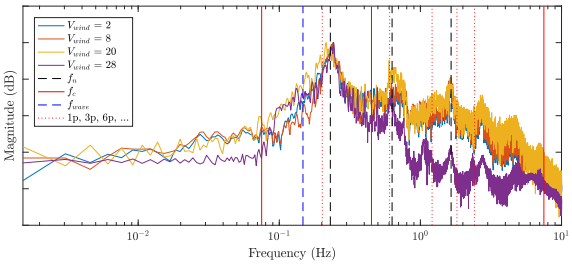

Figure 4.13: normalised PSD's of the ANSYS data for several wind and wave conditions, the presented PSD's are for the acceleration at the top tower node (*Node 1001*).

4.3.2. Addition of Noise to the Signal

Because the virtual measurements from ANSYS are computer generated, they do not contain any noise. As it is expected that during actual measurements measurement noise will corrupt the signal, some level of artificial noise can be added to the virtual data as well. In this way the algorithm can be tested against noise, noise levels of 2 ,5 and 10 % are tested. It is chosen to add independent normally distributed noise to the signal. The algorithm to add noise to the signal is build up as follows:

1. Transfer the set of time domain measurement signals to the frequency domain;
2. Per frequency select the largest value of the signals;
3. Generate the noise by multiplying this value times a random complex number chosen from a normal distribution and the predetermined noise level;
4. Add the noise and the original signal in the frequency domain;
5. Transfer the frequency domain signal to the time domain.

Mathematically this can be noted as:

$$d(f) = \mathscr{F}\{d(t)\} \tag{4.5}$$
$$d_{max}(f) = \max|d(f)| \tag{4.6}$$
$$n_d(f) = d_{max}(f)\,\epsilon_{1,r}\,e^{2\pi i \epsilon_{2,r}}\,nl \tag{4.7}$$
$$d_n(f) = d(f) + n_d(f) \tag{4.8}$$
$$d_n(t) = \mathscr{F}^{-1}\{d_n(f)\} \tag{4.9}$$

Here $d(f) \in \mathbb{I}^{n_m \times 1}$ is the frequency domain representation of the signal $d(t) \in \mathbb{R}^{n_m \times 1}$, n_m is the number of measurement signals, $d_{max}(f)$ is the maximum absolute value in the frequency domain of the input signal, at a certain frequency, $n_d(f) \in \mathbb{I}^{n_m \times 1}$ is the frequency domain representation of the noise, $\epsilon_{1,r}$ is a real random number drawn from a standard normal distribution, $\epsilon_{2,r}$ is a real random number drawn from a standard uniform distribution, $d_n(f) \in \mathbb{I}^{n_m \times 1}$ is the frequency domain representation of the noisy signal and $d_n(t) \in \mathbb{R}^{n_m \times 1}$ is the time history of the noisy signal. Furthermore, $\mathscr{F}^{-1}\{\bullet\}$ and $\mathscr{F}\{\bullet\}$ are the regular and inverse Fourier operators, $|\bullet|$ denotes the absolute value of $\bullet$. For the regular and inverse Fourier transforms the *fft* and *ifft* functions from Matlab are utilised, respectively. Figures 4.14 through 4.19 give a brief overview of the noise added to the signal and the effect that has on uncorrupted signal in both the time and frequency domains.

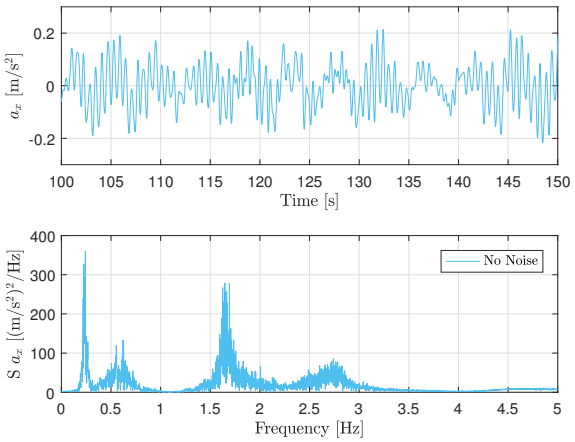

Figure 4.14: Time history (top) and frequency spectrum (bottom) of the for-aft acceleration of *Node 1010* (66.8 m) for LC 5.

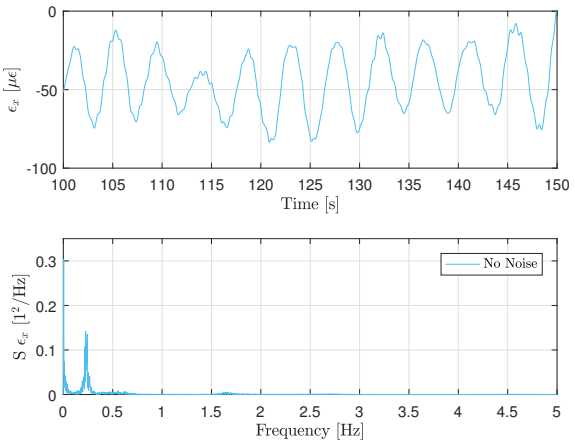

Figure 4.15: Time history (top) and frequency spectrum (bottom) of the for-aft strain of *Node 1401* (-36.5 m) for LC 5.

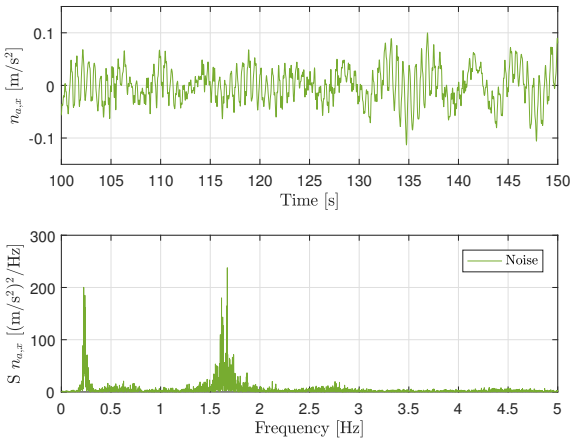

Figure 4.16: Time history (top) and frequency spectrum (bottom) of the noise on the for-aft acceleration of *Node 1010* (66.8 m) for LC 5, with a noise level of 10 %.

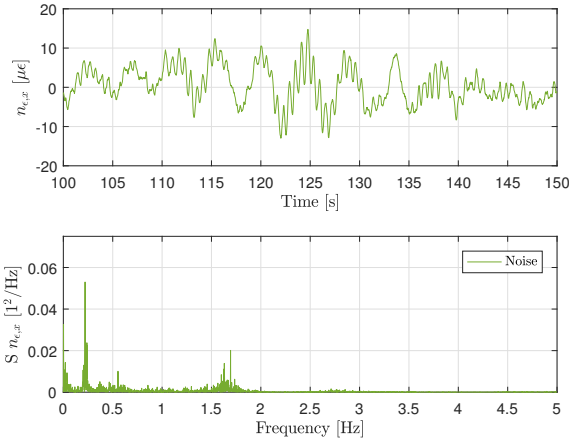

Figure 4.17: Time history (top) and frequency spectrum (bottom) of the noise on the for-aft strain of *Node 1401* (-36.5 m) for LC 5, with a noise level of 10 %.

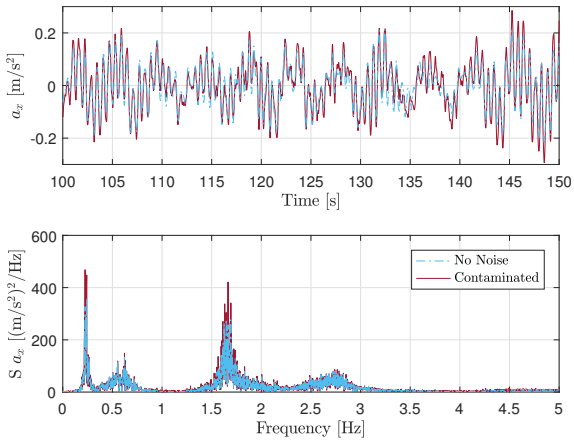

Figure 4.18: Time history (top) and frequency spectrum (bottom) of the clear and contaminated for-aft acceleration of *Node 1010* (66.8 m) for LC 5, with a noise level of 10 %.

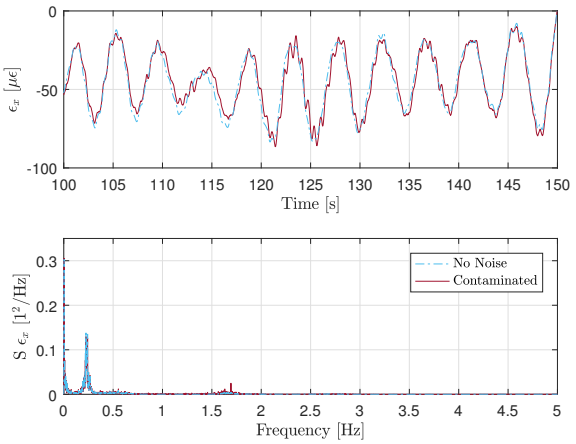

Figure 4.19: Time history (top) and frequency spectrum (bottom) of the clear and contaminated for-aft strain of *Node 1401* (-36.5 m) for LC 5, with a noise level of 10 %.

5
Results

In this chapter the SFI and MB-MDE method, presented in Chapter 2 and 3 respectively, are applied on measurement data generated according to the model presented in the Chapter 4. Several load cases and sensor arrangements are used to assess the sensitivity of the accuracy of the MB-MDE. Finally, the results of MB-MDE are compared to the results of the SFI. In order to properly test the SFI and MB-MDE methods, a methodology was applied in which the starting point was a perfect match between measurement data and the implemented model, in subsequent steps more complexity was introduced. For the SFI method this means that first uncontaminated measurement data is used as input and later noise is introduced to the input. For the MB-MDE a variation on this methodology was applied, the first step was also to use uncorrupted measurement data and to select the sensors and modes for each load case as proposed by Illiopoulos et al., see Appendix F. Then the influence of noise on the strain estimation results was investigated, further variations were made to the sensor and mode settings of the HF band to determine an optimal configuration for each load case. Finally, a weighted least-squared (LS) estimator was put in place of the regular LS estimator to establish whether the negative effects on the strain reconstruction of the measurement noise could be effectively countered. Figure 5.1 shows an overview of the applied methodology for the MB-MDE analysis.

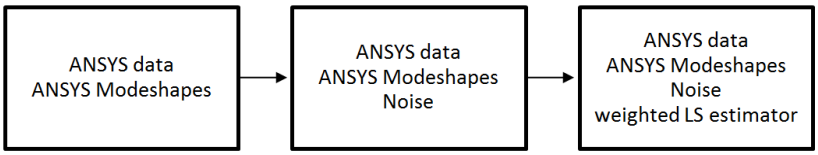

Figure 5.1: Overview of the methodology followed to investigate the multi-band MDE algorithm.

The results will be primarily presented in the form of the Time Response Accuracy Criterion (TRAC) and Mean Absolute Error (MAE) values, which are defined in Appendix E.1.2, here the TRAC value describes the correlation between signals in the time domain and the MAE gives normalised mean error. Some time history plots of the signals will be given in this chapter to support or clarify these values.

The first section covers the strain reconstruction based on the SFI method, through the results in Section 5.2 the quality of the strain reconstruction by the multi-band MDE is discussed. In Section 5.3 the results of a sensitivity analysis on various configurations of the HF band of the multi-band MDE will be reported. Section 5.4 will introduce a comparison between the quality of the results obtained based on the Least-Squares weighted Least-Squares algorithms. Finally, the results of the SFI and MB-MDE will be compared in Section 5.5.

5.1. Strain Reconstruction based on Section Force Interpolation

The results of this method are discussed on the basis of Table 5.1, TRAC values close to 1 are found for all time histories, the values of the MAE criterion show a larger variation. This incongruence between MAE and TRAC can be caused by an offset or amplitude mismatch in the signal, while the frequency content of the signal

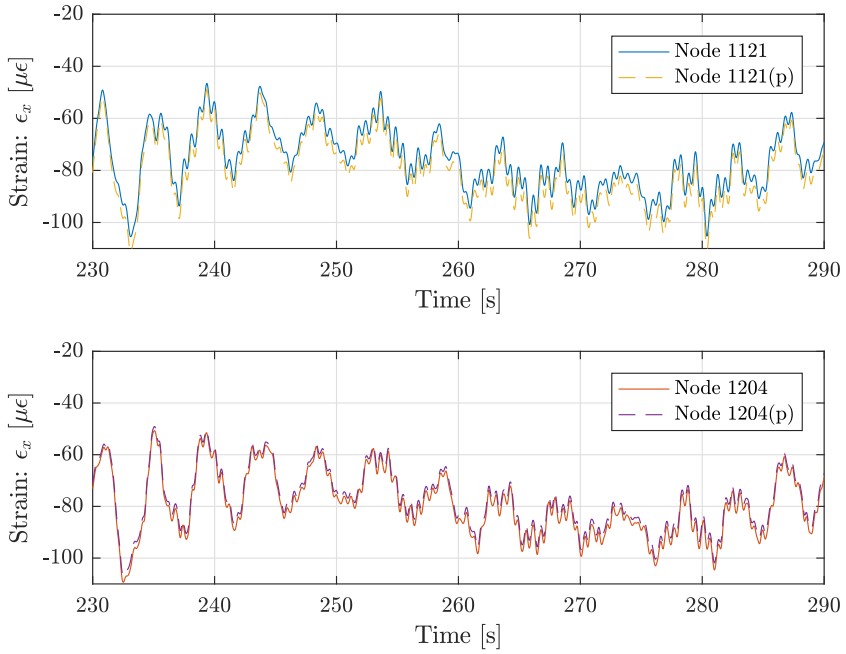

Figure 5.2: Strain time histories for Detail *BB1A* (Node 1121) and *MPCH* (Node 1204) in LC 5, where the signals denoted with *(*p) are the predicted signals, utilising the SFI method. Node 1121: MAE = 0.0193, TRAC = 0.1.000 and Node 1204: MAE = 0.0096, TRAC = 1.0000.

is properly reconstructed. *Detail BB1A* is somewhat of an outlier with both (relatively) high MAE and TRAC scores, this indicates that although there is a good correlation between the estimate and the control signal there is an offset in the signal. Further it can be observed that *Detail CW24* and *Detail MPCH* also perform significantly lower than the other details, this could be caused by an ill-chosen sensor position. Another factor could be that there is a change in the influence of the second mode at these levels. Modes theoretically have a more or less arbitrary correlation with other modes, however for linear interpolation to be valid, the correlation between modes should be constant. For *Detail CW08*, a significant drop in accuracy is displayed between the the strain reconstruction results for Load Cases 1, 5 and 5_{m} and for Load Cases 7 and 8. This could be related to the increased influence of wave loads on this level. Furthermore, there is a slight drop in the values of the TRAC for LC's 7 and 8 as well, especially for the rated operational conditions it could be that rotor dynamics trigger higher order modes, which cause a more complex structural response than can be approximated by linear interpolation. It is noteworthy that the accuracy of the results seems to have a larger correlation to the height along the foundation than to the operational condition of the turbine. In Figure 5.2, the strain time series for Detail *BB1A* (Node 1121) and *MPCH* (Node 1204) are plotted. It can be observed that, although the assurance criteria of these two signal are among the worst performers in Table 5.1, actually correlate to very well to the original signal, an offset is visible which is was already expected from the MAE scores.

Table 5.1: Assurance criteria for the SFI reconstruction of the strain signals for a noise level of 0 %. Each row represents one of the five considered operational conditions, and the columns show the results for reconstructed strains at different heights. The values in cells that are highlighted in red perform worse than cells highlighted in green. A definition of the load cases is given in Table 4.5.

noise level: 0 %		MAE							TRAC						
	Detail:	**BB1A**	**CW11**	**CW08**	**CW18**	**CW24**	**MPCH**	**CW36**	**BB1A**	**CW11**	**CW08**	**CW18**	**CW24**	**MPCH**	**CW36**
Load Case	**Height [m]:**	**8.5**	**5**	**-3**	**-20**	**-29.5**	**-33**	**-47.5**	**8.5**	**5**	**-3**	**-20**	**-29.5**	**-33**	**-47.5**
1		0.0183	0.0017	0.0023	0.0013	0.0076	0.0085	0.0036	1.0000	1.0000	1.0000	1.0000	1.0000	1.0000	1.0000
5		0.0193	0.0018	0.0014	0.0014	0.0085	0.0096	0.0040	1.0000	1.0000	1.0000	1.0000	1.0000	1.0000	1.0000
5_m		0.0188	0.0017	0.0025	0.0013	0.0075	0.0085	0.0037	1.0000	1.0000	0.9999	1.0000	1.0000	1.0000	1.0000
7		0.0146	0.0016	0.0047	0.0022	0.0070	0.0073	0.0033	1.0000	1.0000	0.9997	1.0000	0.9998	0.9999	1.0000
8		0.0163	0.0018	0.0065	0.0012	0.0046	0.0058	0.0030	1.0000	1.0000	0.9997	1.0000	0.9999	1.0000	1.0000

1: Idling *5: Run-up* *5_m: Run-up (Misaligned)* *7: Rated* *8: Cut-out*

Figures 5.3 and 5.4 show the distribution of moment and strain along the length of the foundation. From these figures it becomes apparent that the sections of the moment distribution above mudline and below 2.5D can be described by linear interpolation, the section between mudline and 2.5D below mudline cannot, D is the pile diameter. The erratic behaviour of the strain distribution can be explained by the changing geometry of

the foundation. In Appendix G.1, Figures G.1 and G.2 display that for a homogeneous foundation the moment and strain distributions become smooth, further Figure G.3 shows the influence of the varying foundation geometry on the conversion between moment and strain. The increased error for Details *CW24* and *MPCH* that can be observed in Table 5.1, is caused by the shift in the moment distribution at the mudline due to the lateral resistance of the soil. Especially from Figure 5.3 it can be hypothesized that for the sections that approach linearity, the current set-up is sufficient. The requirement for an accurate measurement system would be to have three sensors for each of the two regions for which a linear interpolation is valid, a higher sensor density would increase the accuracy in the region between mudline and 2.5D below mudline. The interpolation is solely base on the section forces presented in Figure 5.3 and the heights of the considered points along the foundation.

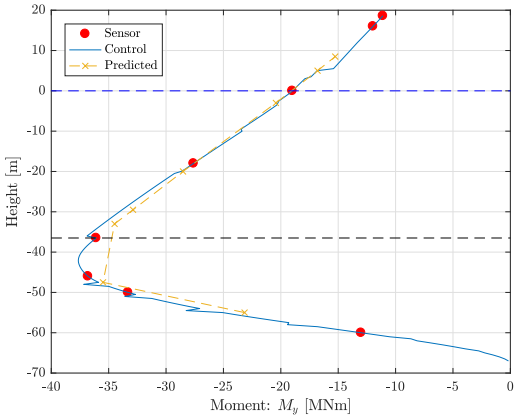

Figure 5.3: The bending moment found from the measurements for the SFI method are plotted along the height of the foundation with their related values for time = 268.94 s, LC 7.

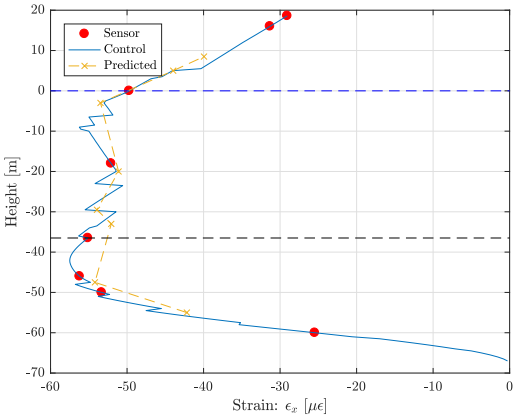

Figure 5.4: The measurement locations for the SFI method are plotted along the height of the foundation with their related values for time = 268.94 s, LC 7.

Introducing Noise to the Section Force Interpolation Strain Reconstruction

After the results for the noise free signals have been presented, now white noise is introduced to the signal according to Section 4.3.2. In the current form there are no inclusions in the algorithm that counteract the effect of noise and therefore the results match the expectations that accuracy decreases with increasing noise. Figures 5.5 and 5.6 show time histories for the strain reconstruction for increased noise levels. In Tables 5.2 and 5.3, the results for all LC's and details are presented. It may be observed that although the results are not completely off, it becomes harder to discern the trends observed in Table 5.1 for increased noise levels. Since no other manipulations than the interpolation are applied it is expected that the strain estimations follow the errors introduced by the corrupted input signal. From Figures 4.15, 4.17 and 4.19 it becomes clear that although the input signals are corrupted, they are not completely distorted. Furthermore, some averaging occurs during the interpolation as noise is distributed randomly over consecutive measurement points.

Table 5.2: Assurance criteria for the SFI reconstruction of the strain signals for a noise level of 5 %. Each row represents one of the five considered operational conditions, and the columns show the results for reconstructed strains at different heights. The values in cells that are highlighted in red perform worse than cells highlighted in green. A definition of the load cases is given in Table 4.5.

noise level: 5 %		MAE							TRAC						
	Detail:	**BB1A**	**CW11**	**CW08**	**CW18**	**CW24**	**MPCH**	**CW36**	**BB1A**	**CW11**	**CW08**	**CW18**	**CW24**	**MPCH**	**CW36**
Load Case	**Height [m]:**	**8.5**	**5**	**-3**	**-20**	**-29.5**	**-33**	**-47.5**	**8.5**	**5**	**-3**	**-20**	**-29.5**	**-33**	**-47.5**
1		0.0205	0.0132	0.0132	0.0163	0.0136	0.0162	0.0141	0.9987	0.9983	0.9984	0.9975	0.9984	0.9978	0.9982
5		0.0230	0.0148	0.0151	0.0118	0.0127	0.0143	0.0161	0.9980	0.9980	0.9981	0.9988	0.9991	0.9988	0.9977
5_m		0.0216	0.0112	0.0132	0.0135	0.0140	0.0163	0.0112	0.9990	0.9988	0.9985	0.9982	0.9984	0.9980	0.9987
7		0.0204	0.0134	0.0146	0.0191	0.0180	0.0201	0.0147	0.9974	0.9975	0.9972	0.9957	0.9963	0.9953	0.9975
8		0.0189	0.0196	0.0191	0.0141	0.0130	0.0145	0.0127	0.9969	0.9963	0.9958	0.9975	0.9977	0.9971	0.9976
		1: Idling			*5: Run-up*			*5_m: Run-up (Misaligned)*	*7: Rated*				*8: Cut-out*		

Table 5.3: Assurance criteria for the SFI reconstruction of the strain signals for a noise level of 10 %. Each row represents one of the five considered operational conditions, and the columns show the results for reconstructed strains at different heights. The values in cells that are highlighted in red perform worse than cells highlighted in green. A definition of the load cases is given in Table 4.5.

noise level: 10 %		MAE							TRAC						
	Detail:	**BB1A**	**CW11**	**CW08**	**CW18**	**CW24**	**MPCH**	**CW36**	**BB1A**	**CW11**	**CW08**	**CW18**	**CW24**	**MPCH**	**CW36**
Load Case	**Height [m]:**	**8.5**	**5**	**-3**	**-20**	**-29.5**	**-33**	**-47.5**	**8.5**	**5**	**-3**	**-20**	**-29.5**	**-33**	**-47.5**
1		0.0276	0.0261	0.0259	0.0325	0.0251	0.0300	0.0270	0.9948	0.9934	0.9937	0.9904	0.9939	0.9914	0.9928
5		0.0230	0.0154	0.0170	0.0286	0.0213	0.0234	0.0189	0.9977	0.9978	0.9974	0.9933	0.9969	0.9961	0.9970
5_m		0.0294	0.0263	0.0281	0.0211	0.0214	0.0257	0.0198	0.9936	0.9935	0.9927	0.9954	0.9953	0.9931	0.9959
7		0.0340	0.0288	0.0296	0.0363	0.0305	0.0347	0.0276	0.9878	0.9884	0.9885	0.9847	0.9887	0.9855	0.9907
8		0.0351	0.0312	0.0339	0.0446	0.0313	0.0315	0.0289	0.9911	0.9888	0.9877	0.9755	0.9875	0.9868	0.9877
		1: Idling			*5: Run-up*			*5_m: Run-up (Misaligned)*	*7: Rated*				*8: Cut-out*		

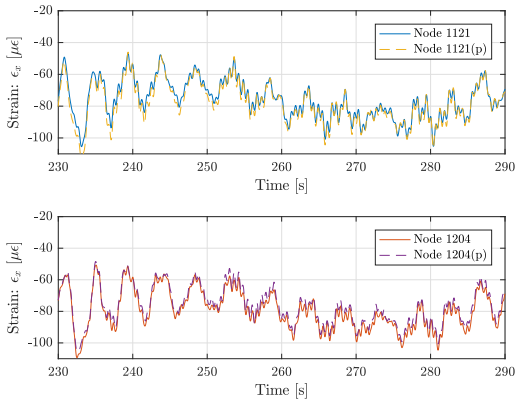

Figure 5.5: Strain time histories for Detail *BB1A* (Node 1121) and *MPCH* (Node 1204) in LC 5, where the signals denoted with *(*p) are the predicted signals utilising the SFI method, with a noise level of 5 %. Node 1121: MAE = 0.0230, TRAC = 0.9980 and Node 1204: MAE = 0.0143, TRAC = 0.9988.

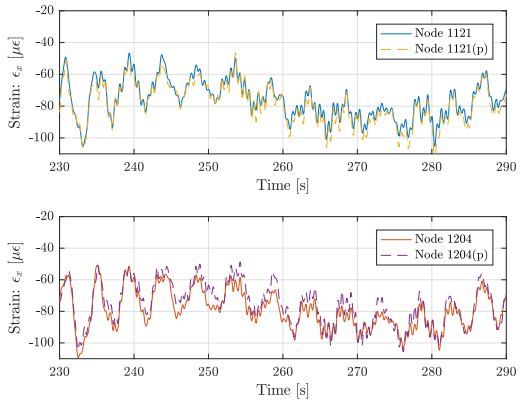

Figure 5.6: Strain time histories for Detail *BB1A* (Node 1121) and *MPCH* (Node 1204) in LC 5, where the signals denoted with *(*p) are the predicted signals utilising the SFI method, with a noise level of 10 %. Node 1121: MAE = 0.0230, TRAC = 0.9977 and Node 1204: MAE = 0.0234, TRAC = 0.9961.

5.2. Strain Reconstruction based on Multi-Band MDE

The Multi-Band approach for the MDE has been thoroughly discussed in Chapter 3, now the results for the selected load cases will be discussed. In Table 5.4 the mode shapes and sensor arrangements are displayed on which tests will be run, this table refers to the original settings as defined by Iliopoulos et al., see Appendix F, Figure F.1. Since a different turbine is used for the virtual measurements, i.e. the NREL 5 MW machine, the cases have been adapted to represent similar turbine conditions, see Figures C.1 and C.2 in Appendix C for the NREL 5 MW turbine characteristics. To adapt the operational cases, the boundary conditions for the varying case definitions were altered, e.g. for LC 7 the turbine should operate at rated rotational speed near the cut-out wind speed, the values for the rated rotational speed and cut-out wind speed were adjusted to match the NREL 5 MW turbine.

Table 5.4: Definition of the considered mode and sensor configurations based on the work by iliopoulos et al., in Table 4.5 the parameters describing the load cases are defined

	Case Definitions						**MDE Sensor/Mode Settings**					
	v_{wind}		RPM		Pitch		VLF band		LF band		HF band	
	min.	max.	min.	max.	min.	max.	0-0.2 Hz		0.2-0.5 Hz		0.5-2 Hz	
1: Idling	0	4	0	0	80	100	ϵ_{19m},ϵ_{66m}	$\phi_\epsilon^{QS,F}$,$\phi_\epsilon^{QS,M}$	α_{87m},α_{31m}	$\phi^{QS,F}$,ϕ^1	α_{87m}, α_{31m}, α_{19m}	ϕ^1, ϕ^2
5 & 5_m: RPM +- 9	7.5	8	8.8	9.2	0	0	ϵ_{19m},ϵ_{66m}	$\phi_\epsilon^{QS,F}$,$\phi_\epsilon^{QS,M}$	α_{87m},α_{31m}	$\phi^{QS,F}$,ϕ^1	α_{87m}, α_{31m}, α_{19m}	ϕ^1, ϕ^2, ϕ^3
7: RPM +- 12.1	19	21	11.9	13	16	19	ϵ_{19m},ϵ_{66m}	$\phi_\epsilon^{QS,F}$,$\phi_\epsilon^{QS,M}$	α_{87m},α_{31m}	$\phi^{QS,F}$,ϕ^1	α_{87m}, α_{31m}	ϕ^1, ϕ^2
8: Cut-Out	25	-	-	-	89	91	ϵ_{19m},ϵ_{66m}	$\phi_\epsilon^{QS,F}$,$\phi_\epsilon^{QS,M}$	α_{87m},α_{31m}	$\phi^{QS,F}$,ϕ^1	α_{87m}, α_{31m}, α_{19m}	ϕ^1, ϕ^2

Now the Multi-Band MDE method is applied to compute the full-field strain in the model presented in Chapter 4, as discussed in Chapter 3. Table 5.5 shows the assurance criteria for the selected load cases, here the settings have been implemented that are defined in Table 5.4. Opposed to the results obtained using SFI presented in Table 5.1, where it was noted that the accuracy was correlated to the height along the monopile, a strong correlation can be observed in Table 5.5 between the accuracy and the load cases. E.g. for LC's 5 and 5_m the accuracy is high for all heights, while for LC's 7 and 8 the MB-MDE method has a significantly lower accuracy. This can either be caused by the configuration of the multi-band MDE as proposed in Table 5.4 or it

can be caused by a more basic setting of the multi-band MDE: the cut-off frequencies. Considering the fact that the wave periods for LC's 7 and 8 are significantly higher than those for LC 1, 5 and 5_m. This could lead to part of the energy of the wave loading spilling into the QS band and quite possibly the QS mode is not able to handle the LF strains caused by this loading. First, Figures 5.7 through 5.9 show that very good results are obtained for Detail *CW08* under LC 5. Figures 5.10 trough 5.14 clearly show that the low accuracy presented for LC's 1 and 7 in Table 5.5 is due to the fact that the estimation signal miss high frequency content around 1.70 Hz, according Table 4.4 the 3rd eigenfrequency is at 1.74 Hz. Missing this content in the estimation indicates the lack of a third mode shape in the mode-and-sensor configuration of the HF band displayed in Table 5.4. These configurations shall be further investigated in Section 5.3. For LC 8 another observation is made from Figures 5.15 through 5.14, first it should be noted that there is hardly any quasi-static content in the response for this LC; as the wind speed is above rated the thrust force is low and the structure is mainly excited by the wave loading. furthermore Figure 5.14 shows that there also is not much content above 0.8 Hz, indicating that it is a valid assumption not to take the third mode into account, however it is also shown that not all HF content is properly estimated this may indicate that more sensors or an other arrangement is required. Finally it seems that some numerical issue causes large peaks in the HF band at 0.4 and 0.5 Hz.

Table 5.5: Assurance criteria for the MDE reconstruction of the strain signals for a noise level of 0 %, each row represents one of the five considered operational conditions, and the columns show the results for different levels. The values in cells that are highlighted in red perform worse than cells highlighted in green. A definition of the load cases is given in Table 4.5.

noise level: 0 %		MAE							TRAC						
	Detail:	**BB1A**	**CW11**	**CW08**	**CW18**	**CW24**	**MPCH**	**CW36**	**BB1A**	**CW11**	**CW08**	**CW18**	**CW24**	**MPCH**	**CW36**
Load Case	**Height [m]:**	**8.5**	**5**	**-3**	**-20**	**-29.5**	**-33**	**-47.5**	**8.5**	**5**	**-3**	**-20**	**-29.5**	**-33**	**-47.5**
1		0.0137	0.0149	0.0172	0.0148	0.0099	0.0080	0.0094	0.9978	0.9974	0.9968	0.9975	0.9987	0.9991	0.9990
5		0.0037	0.0038	0.0043	0.0054	0.0061	0.0065	0.0086	0.9996	0.9996	0.9995	0.9994	0.9993	0.9993	0.9992
5_m		0.0044	0.0052	0.0072	0.0055	0.0057	0.0060	0.0079	0.9995	0.9994	0.9992	0.9994	0.9994	0.9994	0.9994
7		0.0278	0.0299	0.0343	0.0298	0.0181	0.0135	0.0159	0.9873	0.9858	0.9828	0.9882	0.9943	0.9959	0.9955
8		0.0113	0.0149	0.0229	0.0173	0.0129	0.0125	0.0157	0.9959	0.9950	0.9924	0.9937	0.9939	0.9937	0.9920
		1: Idling			*5: Run-up*			*5_m: Run-up (Misaligned)*	*7: Rated*				*8: Cut-out*		

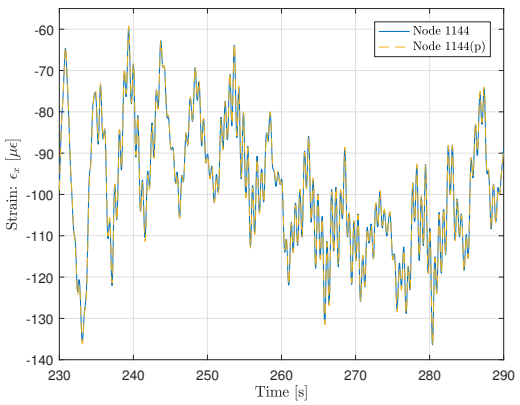

Figure 5.7: Strain time histories for Detail *CW08* (Node 1144) in LC 5, where the signal denoted with (p) is the predicted signal utilising the multi-band MDE method. Node 1144: MAE = 0.0043, TRAC = 0.9995

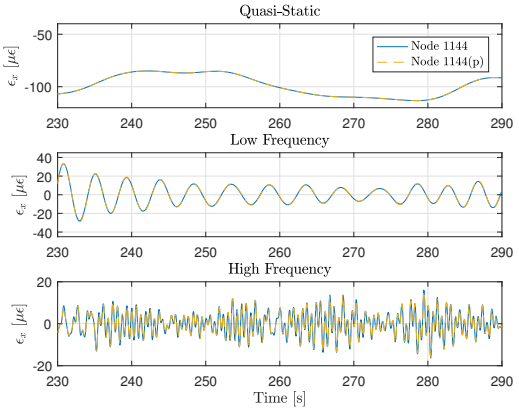

Figure 5.8: Strain time histories for Detail *CW08* (Node 1144) in LC 5, where the signals denoted with (p) are the predicted signals utilising the multi-band MDE method. The signal is displayed here in the separated responses for the QS, LF and HF band

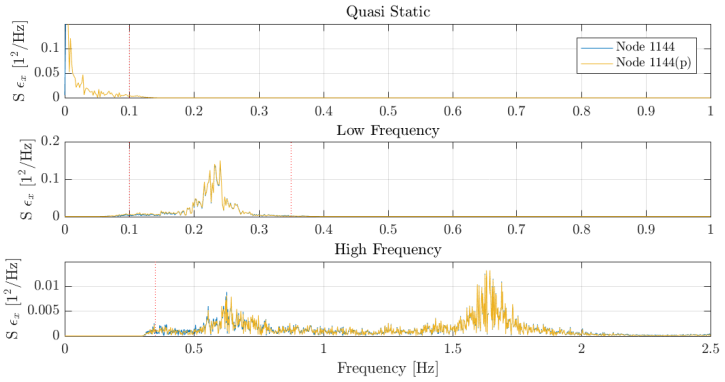

Figure 5.9: Frequency domain representation of the strain for Detail *CW11* (Node 1144) in LC 5, where the signals denoted with *(*p) are the predicted signals utilising the multi-band MDE method. The signal is displayed here in the separated responses for the QS, LF and HF band

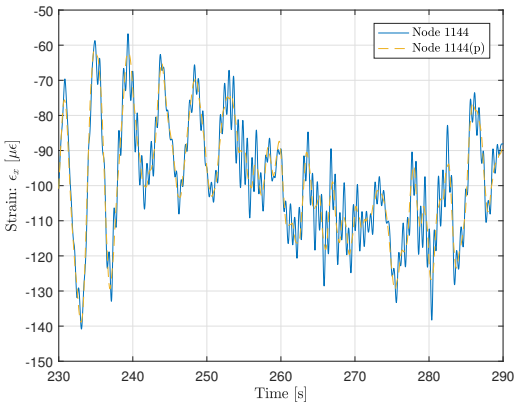

Figure 5.10: Strain time histories for Detail *CW08* (Node 1144) in LC 1, where the signal denoted with *(*p) is the predicted signal utilising the multi-band MDE method. Node 1144: MAE = 0.0172, TRAC = 0.9968

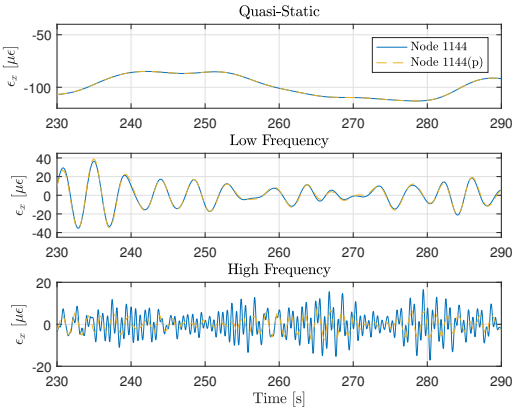

Figure 5.11: Strain time histories for Detail *CW08* (Node 1144) in LC 1, where the signals denoted with *(*p) are the predicted signals utilising the multi-band MDE method. The signal is displayed here in the separated responses for the QS, LF and HF band

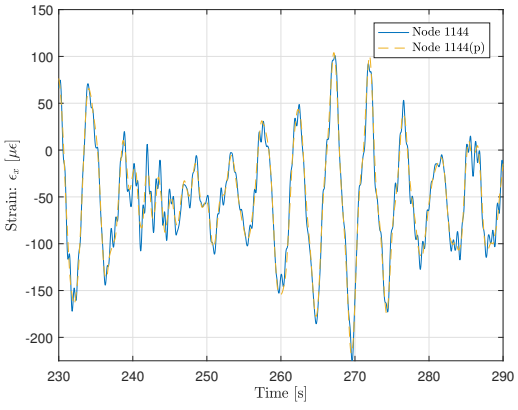

Figure 5.12: Strain time histories for Detail *CW08* (Node 1144) in LC 7, where the signal denoted with *(*p) is the predicted signal utilising the multi-band MDE method. Node 1144: MAE = 0.0343, TRAC = 0.9828

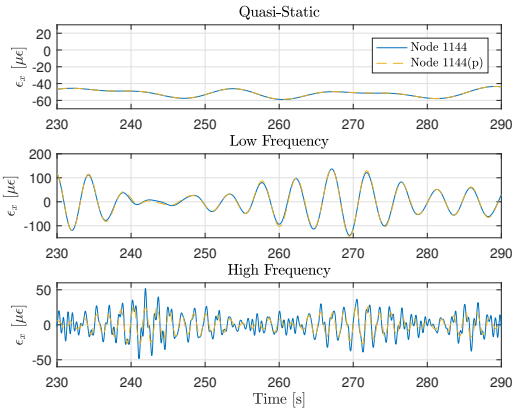

Figure 5.13: Strain time histories for Detail *CW08* (Node 1144) in LC 7, where the signals denoted with *(*p) are the predicted signals utilising the multi-band MDE method. The signal is displayed here in the separated responses for the QS, LF and HF band

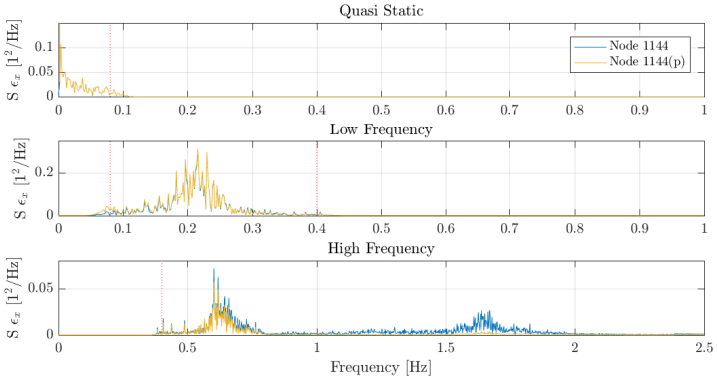

Figure 5.14: Frequency domain representation of the strain for Detail *CW08* (Node 1144) in LC 7, where the signals denoted with *(*p) are the predicted signals utilising the multi-band MDE method. The signal is displayed here in the separated responses for the QS, LF and HF band

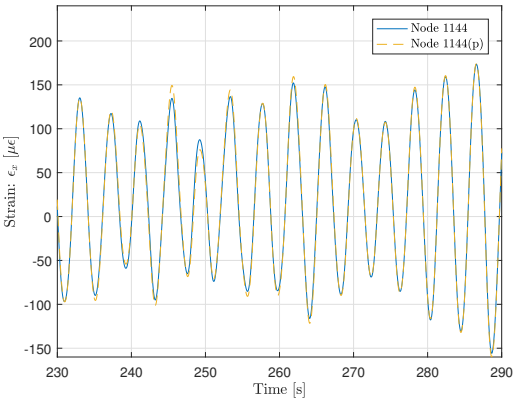

Figure 5.15: Strain time histories for Detail *CW08* (Node 1144) in LC 8, where the signal denoted with *(*p) is the predicted signal utilising the multi-band MDE method. Node 1144: MAE = 0.0229, TRAC = 0.9924

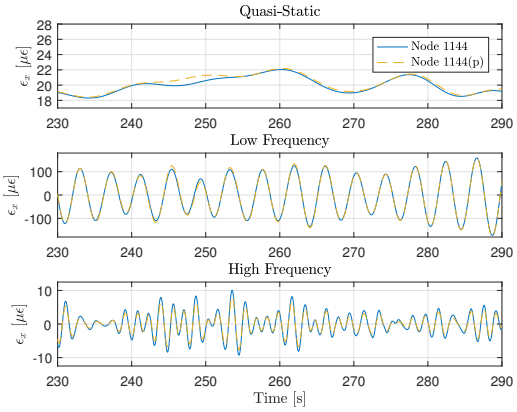

Figure 5.16: Strain time histories for Detail *CW08* (Node 1144) in LC 8, where the signals denoted with *(*p) are the predicted signals utilising the multi-band MDE method. The signal is displayed here in the separated responses for the QS, LF and HF band

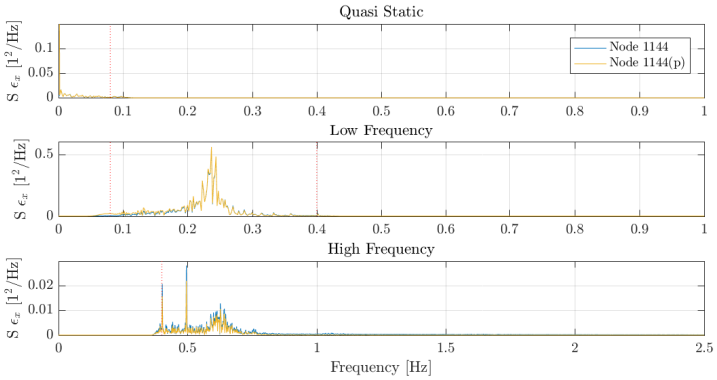

Figure 5.17: Frequency domain representation of the strain for Detail *CW08* (Node 1144) in LC 8, where the signals denoted with *(*p) are the predicted signals utilising the multi-band MDE method. The signal is displayed here in the separated responses for the QS, LF and HF band

Introducing Noise to the Multi-Band MDE Strain Reconstruction

By inspecting Tables 5.6 and 5.7 it can be observed that the MAE values increase dramatically and that the deviation in the TRAC value strongly increases, implying that the accuracy of results computed with the LS estimator, on which the MDE technique is based, are very sensitive to measurement noise. In Figures 5.18 and 5.20 the reconstructed strain signal for noise levels of 0, 5 and 10 % are presented, respectively.

The MDE is sensitive to noise because of the decomposition step, only a few measurements are taken from which the modal coordinates are estimated. If the modal coordinates are corrupted, the errors here will be amplified by the modal expansion. Furthermore, the LS estimator is based on the assumption that the error variance in all input signals is equal, often this assumption is violated and thus algorithms should be used that can account for these variations. In Section 5.4 one of these algorithms will be tested.

Table 5.6: Assurance criteria for the MDE reconstruction of the strain signals for a noise level of 5 %, each row represents one of the five considered operational conditions, and the columns show the results for different levels. Cells that are highlighted in red perform worse than cells highlighted in green. A definition of the load cases is given in Table 4.5.

noise level: 5 %		MAE							TRAC						
	Detail:	**BB1A**	**CW11**	**CW08**	**CW18**	**CW24**	**MPCH**	**CW36**	**BB1A**	**CW11**	**CW08**	**CW18**	**CW24**	**MPCH**	**CW36**
Load Case	**Height [m]:**	**8.5**	**5**	**-3**	**-20**	**-29.5**	**-33**	**-47.5**	**8.5**	**5**	**-3**	**-20**	**-29.5**	**-33**	**-47.5**
1		0.0392	0.0382	0.0361	0.0305	0.0309	0.0321	0.0399	0.9845	0.9855	0.9874	0.9915	0.9911	0.9902	0.9833
5		0.0317	0.0308	0.0288	0.0247	0.0255	0.0268	0.0346	0.9917	0.9923	0.9934	0.9953	0.9948	0.9941	0.9899
5_m		0.0324	0.0312	0.0284	0.0180	0.0198	0.0224	0.0349	0.9898	0.9906	0.9922	0.9964	0.9959	0.9949	0.9877
7		0.0562	0.0537	0.0483	0.0344	0.0364	0.0406	0.0614	0.9557	0.9599	0.9682	0.9848	0.9825	0.9789	0.9556
8		0.0693	0.0642	0.0515	0.0262	0.0421	0.0491	0.0704	0.9477	0.9548	0.9695	0.9903	0.9791	0.9721	0.9426
		1: Idling			*5: Run-up*			*5_m: Run-up (Misaligned)*	*7: Rated*				*8: Cut-out*		

Table 5.7: Assurance criteria for the MDE reconstruction of the strain signals for a noise level of 10 %, each row represents one of the five considered operational conditions, and the columns show the results for different levels. Cells that are highlighted in red perform worse than cells highlighted in green. A definition of the load cases is given in Table 4.5.

noise level: 10 %		MAE							TRAC						
	Detail:	**BB1A**	**CW11**	**CW08**	**CW18**	**CW24**	**MPCH**	**CW36**	**BB1A**	**CW11**	**CW08**	**CW18**	**CW24**	**MPCH**	**CW36**
Load Case	**Height [m]:**	**8.5**	**5**	**-3**	**-20**	**-29.5**	**-33**	**-47.5**	**8.5**	**5**	**-3**	**-20**	**-29.5**	**-33**	**-47.5**
1		0.0743	0.0716	0.0657	0.0550	0.0585	0.0614	0.0769	0.9438	0.9486	0.9584	0.9728	0.9676	0.9629	0.9366
5		0.0642	0.0622	0.0577	0.0472	0.0484	0.0513	0.0690	0.9611	0.9639	0.9700	0.9820	0.9805	0.9776	0.9580
5_m		0.0670	0.0651	0.0604	0.0431	0.0426	0.0453	0.0619	0.9590	0.9614	0.9667	0.9806	0.9816	0.9795	0.9612
7		0.0807	0.0760	0.0650	0.0406	0.0510	0.0590	0.0913	0.9146	0.9247	0.9454	0.9794	0.9694	0.9595	0.9064
8		0.1230	0.1147	0.0929	0.0333	0.0553	0.0674	0.1050	0.8506	0.8684	0.9112	0.9863	0.9622	0.9435	0.8622
		1: Idling			*5: Run-up*			*5_m: Run-up (Misaligned)*	*7: Rated*				*8: Cut-out*		

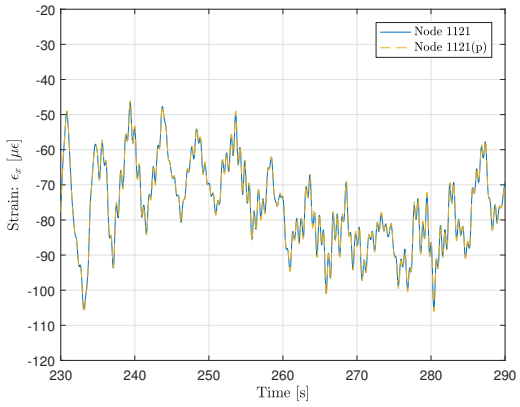

Figure 5.18: Strain time histories for Detail *BB1A* (Node 1121) in LC 5, where the signal denoted with *(*p) is the predicted signal utilising the multi-band MDE method. Node 1121: MAE = 0.0037, TRAC = 0.9996

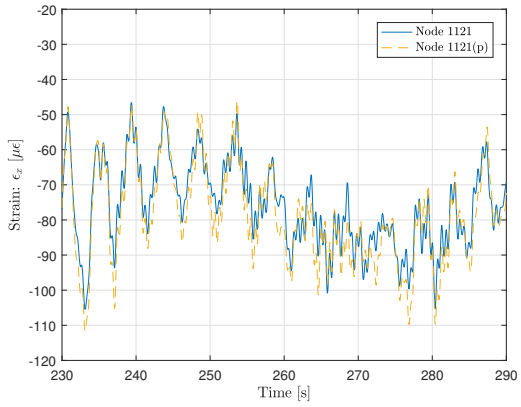

Figure 5.19: Strain time histories for Detail *BB1A* (Node 1121) in LC 5, where the signals denoted with *(*p) are the predicted signals utilising the multi-band MDE method. Node 1121: MAE = 0.0317, TRAC = 0.0.9917

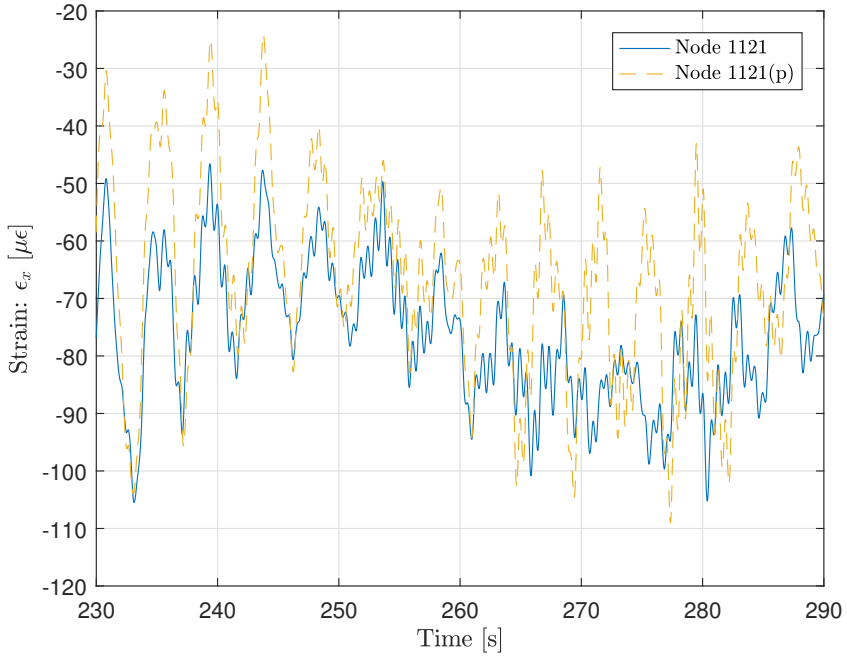

Figure 5.20: Strain time histories for Detail *BB1A* (Node 1121) in LC 5, where the signals denoted with *(*p) are the predicted signals utilising the multi-band MDE method. Node 1121: MAE = 0.0642, TRAC = 0.9611

5.3. Multi-Band MDE Configuration Sensitivity Analysis

As proposed in the introduction of this chapter, a number of different configurations of modes and sensors can be implemented for the MB-MDE. In Section 5.2 it was already presented that the configurations introduced in Table 5.4 may not be optimal with respect to the accuracy of the strain estimation results. It was suggested that mode 3 should also be taken into account for LC's 1 and 7 and that a different sensor arrangement might increase the accuracy for LC 8. To test which configurations are optimal for each load case, a sensitivity analysis is performed on the configurations for HF band. It is assumed here that the optimal settings for the QS and LF band are identical for every load case. Table 5.8 shows 48 possible configurations for the HF band, for the case in which up to four modes can be used. The minimum number of accelerometers follows directly from the number of considered modes.

Strain estimations were performed using the 48 configurations for all 5 load cases under noise levels of 0 and 5 %. For the current analysis, not only the MAE and TRAC will be used as criteria, but the MAE_D is introduced as well. Where, the MAE and TRAC are used to directly quantify the accuracy of the reconstruction of the strain time histories, MAE_D measures the accuracy of the fatigue calculation related to these time histories, Equation 5.1. In Appendix G, Tables G.1 and G.2 are presented to give an impression of the used data. The assurance criteria are computed for all locations presented in Table 4.6, but to quantify the performance over the entire foundation for a specific configuration and load case, the average and standard deviations are given for each criterion.

$$\text{MAE}_\text{D} = \frac{|D_{MB-MDE} - D_{original}|}{D_{original}} \cdot 100 \tag{5.1}$$

Where, MAE_D is the error in the damage, D_{MB-MDE} is the damage calculated from the strain time history reconstructed through the Multi-Band MDE and $D_{original}$ is the damage computed from the control time history for the strain. The strain to stress conversion is performed with Hooke's Law under the assumption that the structure is in plane stress state (Equation 2.2). The method used for the fatigue computation has been presented in Appendix E.1.

The results from the sensitivity analysis of the configurations for the HF band show that there is a big spread in the performance of the investigated configurations, in Appendix G.2 two examples are given of the result tables that were generated for the 5 considered LC's and 2 noise levels. In general it can be observed that at

Table 5.8: Total of 48 possible mode-and-sensor configurations for the sensitivity analysis of the HF band of the Multi-Band MDE, these configurations were run for all 5 LC's, with noise levels of 0 and 5 %.

Modes	**# of Sensors**	**# of Options**
1	1	4
1	2	6
1	3	4
1	4	1
1 & 2	2	6
1 & 2	3	4
1 & 2	4	1
2 & 3	2	6
2 & 3	3	4
2 & 3	4	1
1, 2 & 3	3	4
1, 2 & 3	4	1
2, 3 & 4	3	4
2, 3 & 4	4	1
1, 2, 3, & 4	4	1

least Mode 1 and 2 have to be taken into account for the HF band, with at least two sensors to obtain a good results; including Mode 3 gives even better results. On the other hand if only Mode 2 and 3 are selected it is found that the results are accurate as well, particularly for the error in the damage. Which leads to an other observation that emerges from Table G.2, namely that the configuration with the best score with respect to the MAE and TRAC, does not have the lowest error in fatigue damage, which could be related to the non-linear character of fatigue damage. This notion requires further investigation and thus the configurations with the best MAE and TRAC and the lowest error in fatigue damage are selected (bold face in Table G.2) and have been presented in Tables 5.9 and 5.10, respectively. It should be noted that the configurations are only varied for the HF band, the configurations for the QS and LF bands are kept equal for all LC's.

Table 5.9 shows the results for Configuration [*Mode: 1,2&3, Sensor: 87,66,34&19m*] per height along the foundation, there is clearly a relation visible between the MAE and TRAC values and MAE_D. However in Table 5.10, Configuration [*Mode: 2&3, Sensor: 87,66&19m*], a distinctly different pattern is shown, where the MAE and TRAC values seem to be incongruent with the fatigue results. Thus Details *CW18* and *CW11* will be investigated, these positions are selected as for *CW18* both configurations perform more or less equal on all criteria. However, for *CW11* both configurations score relatively poor in MAE and TRAC values, but the fatigue damage result is far more accurate for Configuration [*Mode: 1,2&3, Sensor: 87,66,34&19m*]. First of all, the time and frequency domain figures (Figures 5.21, 5.22, 5.25 and 5.26) do not show any large differences which is expected based on the similarity of the MAE and TRAC values. Figures 5.23 and 5.24 show the stress cycle histograms for Detail *CW18* obtained using rainflow counting, in these figures it can be observed that there are differences between the predicted and control cycles for both configurations. Although both configurations seem to predict the general trend well, Figure 5.23 shows that the highest three stress cycles are constantly underestimated. From these figures a difference in the MAE_D of 1 percentage point (pp) seems reasonable, all the more because the error is smaller for Configuration [*Mode: 1,2&3, Sensor: 87,66,34&19m*], which also has better MAE and TRAC scores. However, for Detail *CW11* a different trend emerges as the MAE and TRAC scores are slightly worse for Configuration [*Mode: 2&3, Sensor: 87,66&19m*] than for Configuration [*Mode: 1,2&3, Sensor: 87,66,34&19m*] but the MAE_D is significantly smaller by a difference of 14 pp. Figures 5.27 and 5.28 show that in the high amplitude cycles, 14 N/mm^2 and up, there is a large difference between the two estimates, the cycles found from the stress range obtained with Configuration [*Mode: 1,2&3, Sensor: 87,66,34&19m*] show a large underestimation in this region. However, due to the non-linear behaviour of S-N curves used to translate stress to fatigue damage, it is expected that this region has the most influence.

Tables similar to Tables Table G.1 and G.1 have been set up for all load cases and for noise levels of both 0 and 5 %. The results show that for the cases without noise the damage estimation is strongly influenced by the operational state of the turbine. If the OWT is generating energy, i.e. LC 5, 5_m and 7, the configurations providing the best fatigue estimates contain the first three modes. If the turbine is off, only the first

Table 5.9: Assurance criteria for the Configuration [*Mode: 1,2&3, Sensor: 87,66,34&19m*] for LC 1 with a noise level of 5 %.

Mode: 1,2&3, Sensor: 87,66,34&19m						
Detail	*Height [M]*	**MAE**	**TRAC**	$\mathbf{D_{original}}$	$\mathbf{D_{MBMDE}}$	$\mathbf{MAE_D}$ **[%]**
BB1A	*8.5*	0.0371	0.9860	5.66E-09	4.68E-09	17.1836
CW11	*5*	0.0358	0.9872	3.62E-09	3.06E-09	15.3891
CW08	*-3*	0.0328	0.9896	2.03E-08	1.81E-08	10.8541
CW18	*-20*	0.0278	0.9931	9.27E-09	8.94E-09	3.5562
CW24	*-29.5*	0.0302	0.9916	1.25E-08	1.29E-08	2.8472
MPCH	*-33*	0.0318	0.9904	5.99E-10	6.34E-10	5.8433
CW36	*-47.5*	0.0396	0.9835	4.58E-09	5.48E-09	19.7618
mean		0.0336	0.9888			10.7765
standard deviation		0.0041	0.0034			6.8607

Table 5.10: Assurance criteria for the Configuration [*Mode: 2&3, Sensor: 87,66&19m*] for LC 1 with a noise level of 5 %.

Mode: 2&3, Sensor: 87,66&19m						
Detail	*Height [M]*	**MAE**	**TRAC**	$\mathbf{D_{original}}$	$\mathbf{D_{MBMDE}}$	$\mathbf{MAE_D}$ **[%]**
BB1A	*8.5*	0.042567	0.981402	5.66E-09	5.42E-09	4.147
CW11	*5*	0.042059	0.982079	3.62E-09	3.57E-09	1.183
CW08	*-3*	0.040487	0.983649	2.03E-08	2.13E-08	5.057
CW18	*-20*	0.031866	0.990064	9.27E-09	9.67E-09	4.315
CW24	*-29.5*	0.030869	0.991114	1.25E-08	1.31E-08	4.782
MPCH	*-33*	0.031911	0.99032	5.99E-10	6.39E-10	6.532
CW36	*-47.5*	0.041497	0.981695	4.58E-09	5.55E-09	21.127
mean		0.0373	0.9858			6.7350
standard deviation		0.0054	0.0045			6.5471

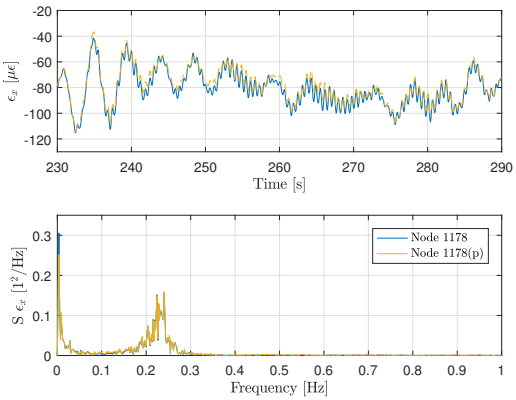

Figure 5.21: Strain reconstruction using the Multi-Band MDE, with a noise level of 5 % and Configuration [*Mode: 1,2&3, Sensor: 87,66,34&19m*] for Detail *CW18* and LC 1. Top Time domain, Bottom: Frequency domain.

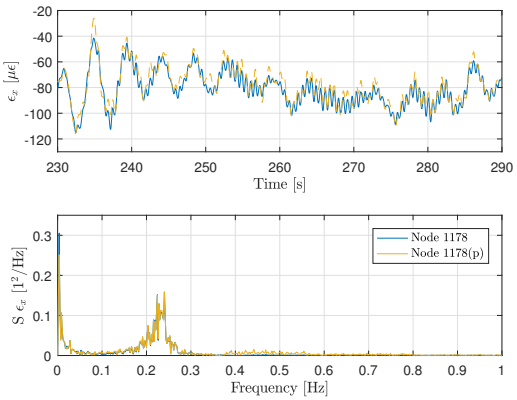

Figure 5.22: Strain reconstruction using the Multi-Band MDE, with a noise level of 5 % and Configuration [*Mode: 2&3, Sensor: 87,66&19m*] for Detail *CW18* and LC 1. Top Time domain, Bottom: Frequency domain.

two modes are required to obtain good fatigue predictions. If there is noise on the input signals this distinct relation seems to become less obvious. Further, the results show that if the input is contaminated with noise, the configuration that scores the highest MAE and TRAC values changes from *Mode: 1,2,3&4, Sensor: 87,66,34&19m* to *Mode: 1,2&3, Sensor: 87,66,34&19m*. Which can be caused by the fact that the energy exciting the fourth mode is below the noise floor in the signal and is no longer picked up properly. From the tables of results for all configurations the best are selected for the 5 % noise situation and these configurations are presented in Table 5.11, it is noted here that the results are similar to the configurations presented in Table 5.4. However, the data shows that including more sensors increases the quality of the output of the Multi-Band MDE. Further, in the current work it is found that better results are obtained if only two modes are taken into

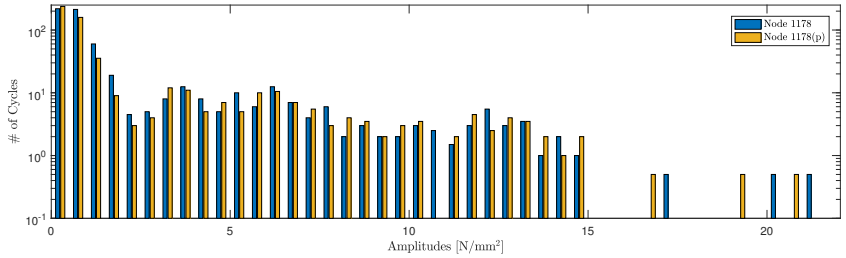

Figure 5.23: Stress cycles from the Rainflow counting for the reconstructed stress history using the Multi-Band MDE, with a noise level of 5 % and Configuration [*Mode: 1,2&3, Sensor: 87,66,34&19m*] for Detail *CW18* and LC 1.

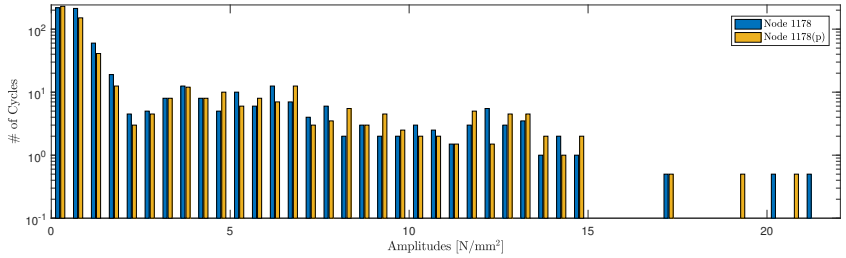

Figure 5.24: Stress cycles from the Rainflow counting for the reconstructed stress history using the Multi-Band MDE, with a noise level of 5 % and Configuration [*Mode: 2&3, Sensor: 87,66&19m*] for Detail *CW18* and LC 1.

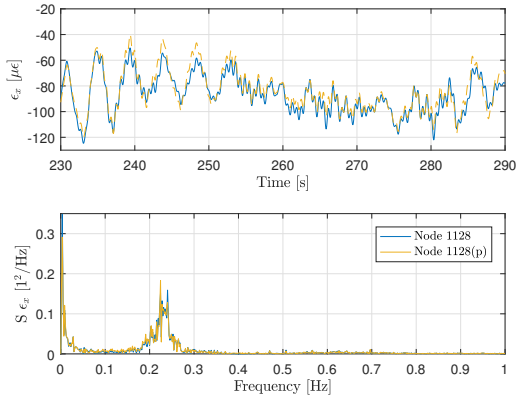

Figure 5.25: Strain reconstruction using the Multi-Band MDE, with a noise level of 5 % and Configuration [*Mode: 1,2&3, Sensor: 87,66,34&19m*] for Detail *CW11* and LC 1. Top Time domain, Bottom: Frequency domain.

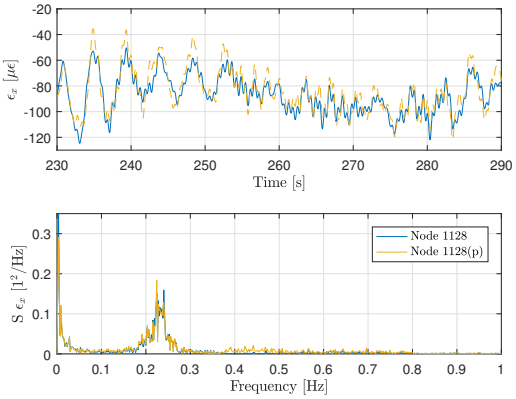

Figure 5.26: Strain reconstruction using the Multi-Band MDE, with a noise level of 5 % and Configuration [*Mode: 2&3, Sensor: 87,66&19m*] for Detail *CW11* and LC 1. Top Time domain, Bottom: Frequency domain.

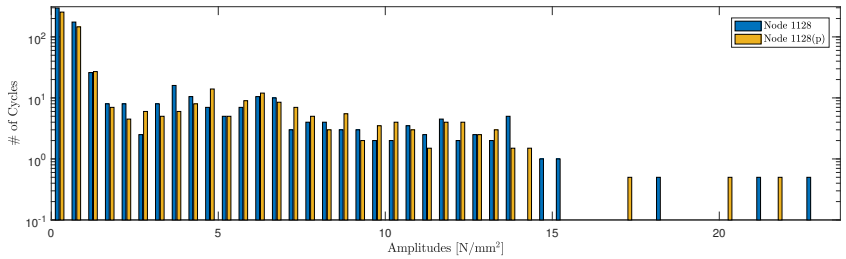

Figure 5.27: Stress cycles from the Rainflow counting for the reconstructed stress history using the Multi-Band MDE, with a noise level of 5 % and Configuration [*Mode: 1,2&3, Sensor: 87,66,34&19m*] for Detail *CW11* and LC 1.

account for LC 8, but opposing to the result from Iliopoulos this is not the case for LC 1.

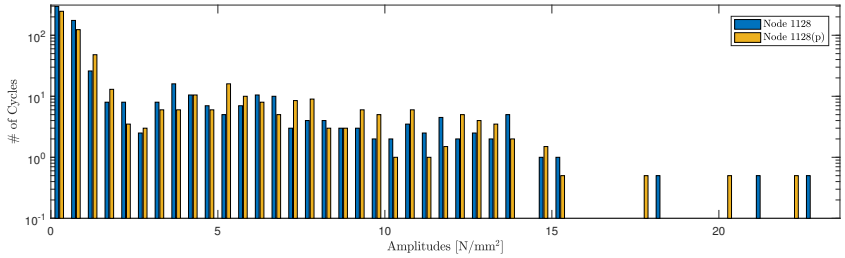

Figure 5.28: Stress cycles from the Rainflow counting for the reconstructed stress history using the Multi-Band MDE, with a noise level of 5 % and Configuration [*Mode: 2&3, Sensor: 87,66&19m*] for Detail *CW11* and LC 1.

Table 5.11: Definition of the optimal mode and sensor configurations for the HF band found in this thesis, the configurations for the QS and LF band are kept identical to the configurations presented in Table 5.4. In Table 4.5 the parameters describing the load cases are defined.

	Case Definitions						**MDE Sensor/Mode Settings**					
	v_{wind}		RPM		Pitch		VLF band		LF band		HF band	
	min.	max.	min.	max.	min.	max.	0-0.2 Hz		0.2-0.5 Hz		0.5-2 Hz	
1: Idling	0	4	0	0	80	100	ϵ_{19m},ϵ_{66m}	$\phi_{\epsilon}^{QS,F}$,$\phi_{\epsilon}^{QS,M}$	α_{87m},α_{31m}	$\phi^{QS,F}$,ϕ^{1}	α_{87m}, α_{66m}, α_{31m}, α_{19m}	ϕ^{1}, ϕ^{2}, ϕ^{3}
5 & 5$_m$: RPM +- 9	7.5	8	8.8	9.2	0	0	ϵ_{19m},ϵ_{66m}	$\phi_{\epsilon}^{QS,F}$,$\phi_{\epsilon}^{QS,M}$	α_{87m},α_{31m}	$\phi^{QS,F}$,ϕ^{1}	α_{87m}, α_{66m}, α_{31m}, α_{19m}	ϕ^{1}, ϕ^{2}, ϕ^{3}
7: RPM +- 12.1	19	21	11.9	13	16	19	ϵ_{19m},ϵ_{66m}	$\phi_{\epsilon}^{QS,F}$,$\phi_{\epsilon}^{QS,M}$	α_{87m},α_{31m}	$\phi^{QS,F}$,ϕ^{1}	α_{87m}, α_{66m}, α_{31m}, α_{19m}	ϕ^{1}, ϕ^{2}, ϕ^{3}
8: Cut-Out	25	-	-	-	89	91	ϵ_{19m},ϵ_{66m}	$\phi_{\epsilon}^{QS,F}$,$\phi_{\epsilon}^{QS,M}$	α_{87m},α_{31m}	$\phi^{QS,F}$,ϕ^{1}	α_{66m}, α_{31m}, α_{19m}	ϕ^{1}, ϕ^{2}

5.4. Testing the weighted Least-Squares Extension on the MDE

The weighted Least-Squares algorithm, introduced in Section 3.3, is applied here to investigated its ability to reduce the sensitivity of the MDE to noise. Load case 5 is considered for this test and the MB-MDE is run with Configuration [*Mode: 1,2&3, Sensor: 87,66,34&19m*], as well as for the regular full band MDE. To inspect the influence of the wLS on the full band MDE, a displacement estimation based on unfiltered displacement input signals is inspected. Also a displacement estimation based on filtered displacement measurements is performed, in this case the input signals have been run through the same filters as the strain and acceleration measurement signals for the MB-MDE. Finally, to compare the MB-MDE and the full band results, a displacement estimation was also performed based displacement and acceleration input. The tests were run for noise levels of 5 and 10 % and the results are presented in Tables 5.12 and 5.13, respectively. From Table 5.12 it becomes apparent that for the full band MDE the wLS does increase the accuracy of the results. Further inspection of this table shows that filtering the input data results in a larger increase in the accuracy of the full band MDE than applying the wLS. A low pass AA filter is applied before the signal is filtered into the respective QS, LF and HF bands, this AA filter also removes any very high frequency noise in the signal, this could positively influence the estimation results. Finally, it can be observed from Table 5.12 that for the MB-MDE the results are not significantly affected. In Table 5.13 is displayed that for higher noise levels the wLS actually decreases the accuracy of the MDE. This could be related to the inherent weakness of the wLS estimator; since the weights describe the trustworthiness of the signal, but do not consider how important the sensor data is for the estimation. Therefore the most relevant sensor for a specific load case might, due to high error variance, not be taken into account at all, thus lowering the quality of the final results. In Figures 5.29 and 5.30 the reconstructed displacement and strain for the Multi-Band MDE are plotted. For these results no distinction between the computed values with and without the wLS addition can be observed. To gain insight in the algorithm of the wLS the weights that are introduced in the computations for Table 5.13 are displayed in Figures 5.31 through 5.33, Figure 5.34 shows the position of the related sensors.

Table 5.12: MAE and TRAC assurance criteria for the displacement reconstruction with the LS and wLS algorithms for a signal with a noise level of 5 %, the algorithms are tested for the full band MDE, the full band MDE with a filtered signal and the Multi-Band MDE methods, cells highlighted in green contain values that outperform their direct counterpart.

noise level: 5 %		MAE							TRAC						
	Detail:	**BB1A**	**CW11**	**CW08**	**CW18**	**CW24**	**MPCH**	**CW36**	**BB1A**	**CW11**	**CW08**	**CW18**	**CW24**	**MPCH**	**CW36**
Cases:	**Height [m]:**	**8.5**	**5**	**-3**	**-20**	**-29.5**	**-33**	**47.5**	**8.5**	**5**	**-3**	**-20**	**-29.5**	**-33**	**47.5**
Regular MDE	*LS*	0.03938	0.04675	0.06574	0.10775	0.13050	0.13850	0.17744	0.98793	0.98307	0.96672	0.91147	0.87099	0.85439	0.76210
	wLS	0.03927	0.04662	0.06555	0.10743	0.13012	0.13810	0.17691	0.98799	0.98316	0.96693	0.91206	0.87186	0.85537	0.76365
Regular MDE (filtered)	*LS*	0.03834	0.04537	0.06339	0.10265	0.12387	0.13167	0.16997	0.98812	0.98336	0.96739	0.91344	0.87389	0.85764	0.76717
	wLS	0.03823	0.04524	0.06320	0.10234	0.12350	0.13128	0.16946	0.98818	0.98346	0.96759	0.91402	0.87474	0.85860	0.76869
Multi-Band MDE	*LS*	0.02586	0.02698	0.02951	0.03399	0.03611	0.03689	0.04070	0.99419	0.99368	0.99242	0.98985	0.98845	0.98791	0.98498
	wLS	0.02586	0.02698	0.02951	0.03398	0.03611	0.03688	0.04070	0.99419	0.99368	0.99242	0.98985	0.98845	0.98791	0.98498

Table 5.13: MAE and TRAC assurance criteria for the displacement reconstruction with the LS and wLS algorithms for a signal with a noise level of 10 %, the algorithms are tested for the full band MDE, the full band MDE with a filtered signal and the Multi-Band MDE methods, cells highlighted in green contain values that outperform their direct counterpart.

noise level: 10 %		MAE							TRAC						
	Detail:	**BB1A**	**CW11**	**CW08**	**CW18**	**CW24**	**MPCH**	**CW36**	**BB1A**	**CW11**	**CW08**	**CW18**	**CW24**	**MPCH**	**CW36**
Cases:	**Height [m]:**	**8.5**	**5**	**-3**	**-20**	**-29.5**	**-33**	**47.5**	**8.5**	**5**	**-3**	**-20**	**-29.5**	**-33**	**47.5**
Regular MDE	*LS*	0.06262	0.07231	0.09745	0.15304	0.18310	0.19366	0.24532	0.96672	0.95585	0.92074	0.81188	0.73929	0.71102	0.56826
	wLS	0.06757	0.07738	0.10269	0.15879	0.18946	0.20026	0.25304	0.96260	0.95110	0.91451	0.80336	0.73030	0.70200	0.56004
Regular MDE (filtered)	*LS*	0.06076	0.06997	0.09363	0.14553	0.17364	0.18403	0.23520	0.96706	0.95628	0.92144	0.81312	0.74067	0.71242	0.56946
	wLS	0.06589	0.07523	0.09919	0.15186	0.18057	0.19117	0.24338	0.96301	0.95162	0.91534	0.80479	0.73189	0.70361	0.56146
Multi-Band MDE	*LS*	0.05299	0.05552	0.06130	0.07159	0.07647	0.07822	0.08676	0.97589	0.97357	0.96783	0.95605	0.94976	0.94737	0.93486
	wLS	0.05299	0.05552	0.06130	0.07160	0.07648	0.07823	0.08677	0.97589	0.97357	0.96782	0.95604	0.94975	0.94736	0.93485

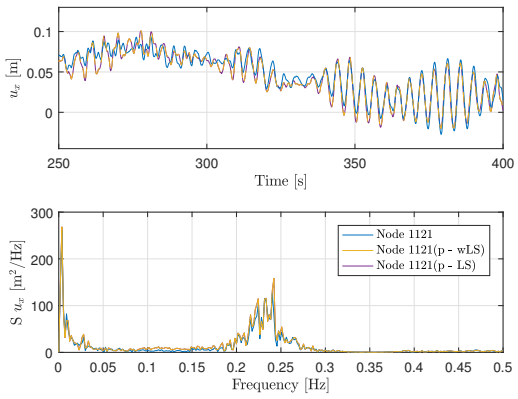

Figure 5.29: Displacement reconstruction for the Multi-Band MDE, with a noise level of 10 %. Top Time domain, Bottom: Frequency domain.

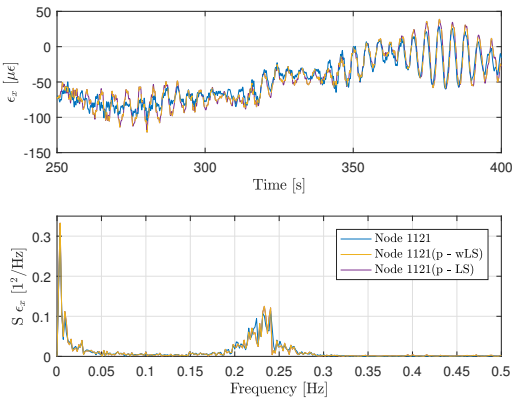

Figure 5.30: Strain reconstruction for the Multi-Band MDE, with a noise level of 10 %. Top Time domain, Bottom: Frequency domain.

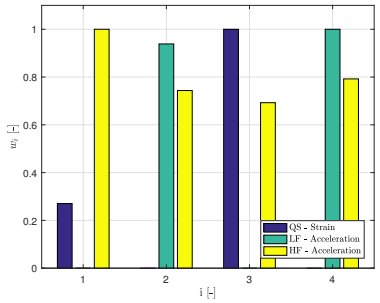

Figure 5.31: Normalised weights for the Multi-Band MDE strain reconstruction, for a noise level of 10 %.

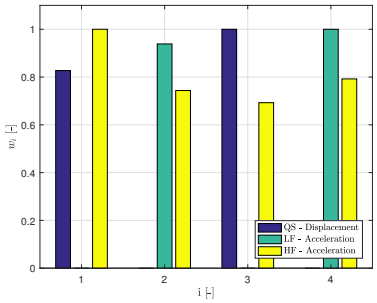

Figure 5.32: Normalised weights for the Multi-Band MDE displacement reconstruction, for a noise level of 10 %.

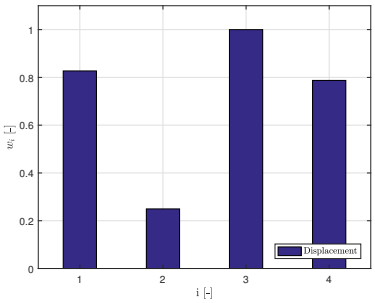

Figure 5.33: Normalised weights for the full band MDE displacement reconstruction, for a noise level of 10 %.

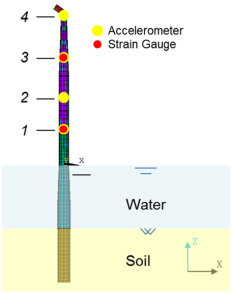

Figure 5.34: The notation of the weights presented in Figures 5.33 through 5.31 is related to the sensor positions according to the numbering presented here. For-Aft: 1 to 4 and Side-Side: 5 to 8.

5.5. Comparison Between Section Force Interpolation and Multi-Band Modal Decomposition & Expansion Methods

In this section a comparison is made between the SFI and MB-MDE methods with respect to the stress estimation and the fatigue damage computation, the goal is to assess which method would be better suited for a fatigue damage monitoring system on an OWT. For the MB-MDE the optimal configurations, determined in Section 5.3, are implemented. Thus, Configuration [*Mode: 1,2&3, Sensor: 87,66,34&19m*] was used for all LC's, but LC 8. To estimate the strains for LC 8, Configuration [*Mode: 1&2, Sensor: 66,34&19m*] was implemented, in accordance with Table 5.11. Since in Section 5.1 was already determined that Detail *BB1A* was an outlier for the SFI strain reconstruction, it is chosen not to take this detail into account for the current comparison. Table 5.14 shows that the MB-MDE and SFI methods are both able to score very good values for the MAE and TRAC values for a situation without measurement noise. In this Table 5.14 error statistics are presented, the values displayed here do not represent the mean and standard deviation values of the actual strain signals, but relate to the assurance criteria over the length of the foundation. From Table 5.14 it can be observed that the MAE values for the SFI have a relatively high standard deviation, this should be related to an observation made in Section 5.1: the SFI results do not seem to be influenced by load cases as much as by height. This causes large differences in the quality of the strain estimation for the considered details for a specific load case and results in a high standard deviation in the assurance criteria. For the MB-MDE a stronger correlation exists between the load case and the quality of the strain estimation results for the entire foundation.

Even more, in Figures 5.35 through 5.38 it can be clearly observed that both the strain estimation and the rainflow stress cycle histogram from the MB-MDE estimation are more accurate than the results for the SFI method. The difference is likely to originate from the fact that the MB-MDE is able to reconstruct more complex structural response than the linear interpolation, because of the use of mode shape superposition. However, both methods do not deliver the 2 % accuracy norm required by Van Oord. Table 5.15 further shows that the SFI method scores well in the region between the top of the pile and about $2D$ above the mudline; the MB-MDE scores better in the region from D above the mudline to $2D$ below the mudline, where D is the pile diameter. From Figure 5.3 it can be observed that the region the mudline and $2D$ below the mudline is where the moment distribution has a peak and shows non-linear behaviour.

The difference in the results between the SFI and MB-MDE, for input signals contaminated with measurement noise, can be explained by the relative insensitivity and sensitivity to measurement noise of the SFI and MDE respectively as discussed in Sections 5.1 and 5.2.

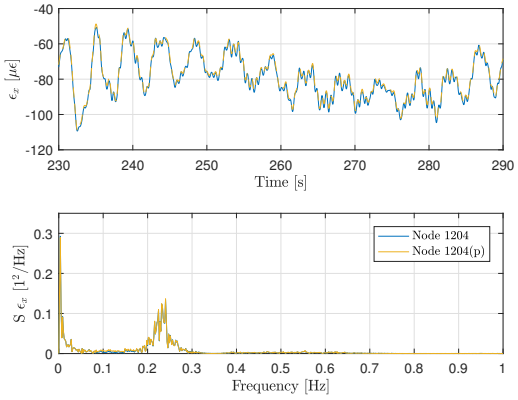

Figure 5.35: Strain reconstruction using the Multi-Band MDE, with a noise level of 0 % and Configuration [*Mode: 1,2&3, Sensor: 87,66,34&19m*] for Detail *MPCH*. Top Time domain, Bottom: Frequency domain.

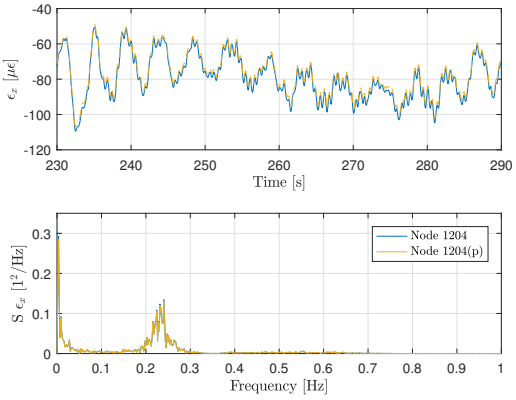

Figure 5.36: Strain reconstruction using the SFI, with a noise level of 0 %, for Detail *MPCH*. Top Time domain, Bottom: Frequency domain.

Table 5.14: Comparison between SFI and Multi-Band MDE strain reconstructions.

	MAE				**TRAC**				**MAE_D**			
	SFI		**MB-MDE**		**SFI**		**MB-MDE**		**SFI**		**MB-MDE**	
noise level: 0 %	**mean**	**std**	**mean**	**std**	**mean**	**std**	**mean**	**std**	**mean**	**std**	**mean**	**std**
1	0.0042	0.0031	0.0067	0.0009	1.0000	0.0000	0.9992	0.0001	5.4825	3.7492	4.4896	2.1786
5	0.0044	0.0037	0.0063	0.0015	1.0000	0.0000	0.9994	0.0001	5.4664	3.6006	3.5871	1.4403
5_m	0.0042	0.0031	0.0066	0.0010	1.0000	0.0000	0.9993	0.0001	5.7335	3.7669	4.2080	2.1483
7	0.0043	0.0024	0.0135	0.0027	0.9999	0.0001	0.9955	0.0012	5.5352	3.3824	3.5952	1.6559
8	0.0038	0.0022	0.0160	0.0038	0.9999	0.0001	0.9935	0.0011	5.2032	3.6685	7.8826	3.3761
noise level: 2 %												
1	0.0059	0.0021	0.0163	0.0021	0.9998	0.0001	0.9972	0.0006	5.4017	2.4302	6.7323	2.9035
5	0.0076	0.0036	0.0109	0.0019	0.9997	0.0002	0.9987	0.0004	6.0906	3.2260	6.7345	3.2039
5_m	0.0074	0.0029	0.0113	0.0028	0.9996	0.0003	0.9984	0.0006	6.9443	3.9353	10.0417	3.6112
7	0.0076	0.0015	0.0182	0.0023	0.9994	0.0001	0.9939	0.0016	5.7993	2.7441	2.5653	1.2769
8	0.0080	0.0012	0.0277	0.0079	0.9994	0.0002	0.9882	0.0046	5.7162	4.0591	16.8010	6.5121
noise level: 5 %												
1	0.0144	0.0014	0.0330	0.0042	0.9981	0.0004	0.9893	0.0034	4.9288	3.3705	9.7086	6.2904
5	0.0141	0.0016	0.0277	0.0038	0.9984	0.0005	0.9938	0.0020	2.9584	3.8367	28.8034	14.2651
5_m	0.0132	0.0019	0.0235	0.0072	0.9984	0.0003	0.9941	0.0034	11.3658	4.3408	22.3261	13.0886
7	0.0167	0.0028	0.0414	0.0123	0.9966	0.0009	0.9764	0.0122	2.9705	3.3669	29.1997	22.0097
8	0.0155	0.0031	0.0506	0.0158	0.9970	0.0008	0.9681	0.0171	5.3644	2.1837	27.7318	16.2374
noise level: 10 %												
1	0.0278	0.0029	0.0642	0.0084	0.9926	0.0014	0.9588	0.0134	13.2606	7.4803	26.4539	24.7695
5	0.0208	0.0048	0.0534	0.0088	0.9964	0.0016	0.9745	0.0096	11.4664	13.4082	16.7522	7.9317
5_m	0.0238	0.0034	0.0495	0.0095	0.9943	0.0014	0.9758	0.0089	17.2619	5.4027	42.7627	20.7908
7	0.0313	0.0035	0.0607	0.0195	0.9878	0.0022	0.9517	0.0279	9.5263	7.6520	41.7993	26.0157
8	0.0336	0.0056	0.0781	0.0314	0.9857	0.0050	0.9223	0.0506	8.9916	4.7972	48.1510	19.2220

1: Idling *5: Run-up* *5_m: Run-up (Misaligned)* *7: Rated* *8: Cut-out*

Table 5.15: The assurance criteria results for the damage estimation from the strain reconstructions based on the SFI (left) and MB-MDE (right), Detail*BB1A* has been left out. The *mean* and *std* columns are identical to the MAE_D columns for a noise level of 0 % in Table5.14

noise level: 0 %	**SFI**								**MB-MDE**							
	MAE_D								**MAE_D**							
Detail:	**CW11**	**CW08**	**CW18**	**CW24**	**MPCH**	**CW36**	*mean*	*std*	**CW11**	**CW08**	**CW18**	**CW24**	**MPCH**	**CW36**	*mean*	*std*
Height [m]:	**5**	**-3**	**-20**	**-29.5**	**-33**	**-47.5**			**5**	**-3**	**-20**	**-29.5**	**-33**	**-47.5**		
1	1.9237	3.0308	1.3134	9.7991	11.3544	5.4734	5.4825	3.7492	6.3500	9.0150	5.7581	1.2766	0.0560	4.4821	4.4896	2.1786
5	1.9968	2.1066	1.8641	9.9736	11.4315	5.4260	5.4664	3.6006	3.9146	5.6496	5.1450	2.6455	1.1729	2.9951	3.5871	1.4403
5_m	2.0780	2.0211	1.9471	10.8549	11.9128	5.5869	5.7335	3.7669	4.4810	8.2150	5.0261	0.4146	1.2545	5.8566	4.2080	2.1483
7	2.4716	0.0663	2.5933	10.6096	11.5756	5.8949	5.5352	3.3824	6.6587	6.6042	3.7572	0.5005	0.4091	3.6418	3.5952	1.6559
8	1.7557	6.4366	0.3008	7.2094	9.8834	5.6335	5.2032	3.6685	5.4121	13.1153	12.9336	7.2161	4.7662	3.8521	7.8826	3.3761

1: Idling *5: Run-up* *5_m: Run-up (Misaligned)* *7: Rated* *8: Cut-out*

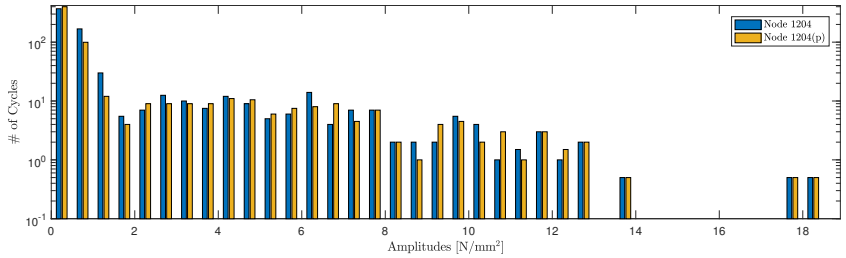

Figure 5.37: Stress cycles from the Rainflow counting for the reconstructed stress history using the Multi-Band MDE, with a noise level of 0 % and Configuration [*Mode: 1,2&3, Sensor: 87,66,34&19m*] for Detail *MPCH*.

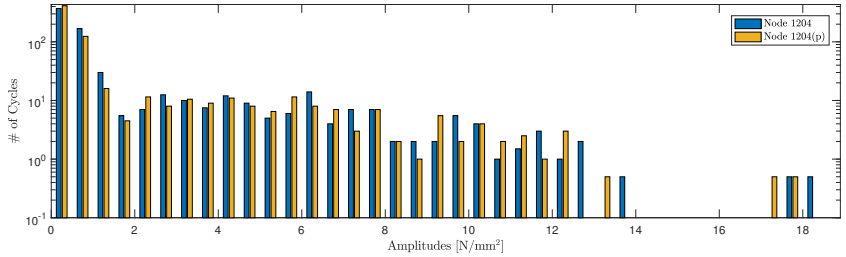

Figure 5.38: Stress cycles from the Rainflow counting for the reconstructed stress history using the SFI, with a noise level of 0 % for Detail *MPCH*.

Conclusions

To further decrease the cost of energy produced by an Offshore Wind Turbine, an investigation into two techniques aimed at fatigue damage monitoring has been presented. By 2016, 80 % of all installed OWT's in Europe utilised a monopile foundation; therefore the focus of this work is on monitoring damage accumulation in these specific structures.

Observations of the actual fatigue damage accumulation could enable wind park owners to continue operation even passed the original design life of the structures. The estimation of in-service strains and thus stresses, necessary as input for the fatigue calculations, is relevant for the entire industry. The objective of this thesis was to:

"Verify and compare techniques for the estimation of in-service strains in offshore wind support structures from a limited set of sensors, for use in fatigue damage monitoring."

Throughout this work investigations have been presented to establish the validity of strain estimation techniques for Offshore Wind Turbines.

Conclusions

Two distinct estimation techniques were presented and for both conclusions can be drawn:

- Section Force Interpolation is a simple and robust estimation method for the operational strain in an offshore wind turbine foundation. The challenge for this method lies in the measurement system, that is required to be driven into the soil along with the pile;
- The Multi-Band Modal Decomposition and Expansion technique is very effective in the prediction of the full-field strain response of the structure, but high noise levels can strongly reduce the quality of the results.

SFI Strain Reconstruction

The strain reconstruction based on Section Force Interpolation has the potential to give accurate estimations of the strain in the foundation, using a very simple and robust method. Under the condition that strain sensors are calibrated properly; the reconstructed signals are good estimates of the original signal, even for high levels of noise, showing no sign of drift in the results and keeping a strong correlation with the frequencies found in the uncorrupted strains. Obtaining the strain measurements necessary for this reconstruction method does introduce a complicating factor as measurements along the length of the foundation are required.

Behaviour of the moment distribution along the length of the foundation is shown to be linear in the sections above mudline and below $2.5D$, the section between mudline and $2.5D$ below mudline cannot be approached by a linear relation, D is the pile diameter. Thus, for strain reconstruction, with 3 sensors covering each linear region already a decent estimation will be obtained for those areas, however to properly measure the peak moment it is advisable to install at least 2 sensors between 1 and $2D$ below the mudline. Thus a measurement system with 8 sensors would results in more accurate results than presented in this work.

Multi-Band MDE Strain Reconstruction

It was found that the Multi-Band Modal Decomposition and Expansion method for full-field strain estimation suggested by Illiopoulos et al. shows accurate results for simulations on a FEM model of an OWT foundation excited by irregular waves and wind loads [38]. The multi-band approach allows for the use of both strain gauges and accelerometers, enabling the method to predict both quasi-static and dynamic response.

During the sensitivity analysis of the MB-MDE it was found that the sensor Configuration [*Mode: 1,2&3, Sensor: 87,66,34&19m*] provides the best accuracy under LC's 1 trough 7 and [*Mode: 1&2, Sensor: 66,34&19m*] is the optimal configuration for LC 8. The configurations for LC 1 and 7 differ significantly from the previous suggested configurations in the work on Multi-Band MDE by Iliopoulos et al.[38]; however, the fact that the other research was performed on a different structure is expected to be the main reason for this dissimilarity.

Introducing the wLS algorithm to the Multi-Band MDE method did not result in significant improvement of the strain estimation results for the investigated load cases. The filtering required for the Multi-Band method already decreases the effect of noise on the signal and applying the MB-MDE strongly decreases the influence of measurement noise on the estimation results.

Strain Reconstruction: SFI vs. Multi-Band MDE

For noise levels of 0 % both methods perform very well, if measurement noise is introduced the results computed with the Multi-Band MDE become less accurate and show large amplitude and phase errors for noise levels of 5 and 10 %, while for the SFI method only limited amplitude errors are observed. Thus with respect to fatigue computation based on input signals contaminated with measurement noise, the SFI method gives better results.

Recommendations

From the insights gained during the work on this thesis, some recommendations have come forward. These suggestions focus on the Multi-Band MDE and on the general measurement system set-up. Finally, some recommendations regarding further research are given.

Recommendations for application of the Multi-Band MDE

The accuracy of the MDE is strongly dependent on the relation between the mode shapes and the measurement data. Thus if a system based on modal decomposition is implemented for offshore structures it is highly recommended to include an extensive operational modal analysis system along with the estimation system. In this way an automatic selection of the utilised mode shapes and configurations can be based on the operational conditions of the turbine. As the error in the estimation of fatigue damage computation should be narrowed down to less than 2 %, it is essential that the system always operates in the optimal configuration.

Recommendations for Measurement Systems

Fibre-Bragg Grating strain sensor should be utilised for the measurement of strain, especially if measurements are to be performed below water level or the mudline. For these locations pre-installed multiplexed FBG strain sensors should be used, due to their minimal weight and size these sensors have increased chances of survival during pile-driving; driving shoes and covers to protect these sensors can also be minimalised with respect to a system based on regular strain gauges. Furthermore, these sensors are expected to have better durability properties than electrical strain sensors.

A more robust calibration for in-service strain sensors is required, preferably one that is not negatively affected by environmental conditions. The 360°rotation of the RNA is a good calibration method under calm weather conditions, however it only takes into account measurements at that instant in time. If this method is implemented it is advised to apply this calibration on on a regular basis to counter the effects of only measuring for a an instant in time.

In this thesis, use was made of a case-by-case selection of configurations. This, as well as further studies regarding the effects of operational conditions on the structural response, can only be performed effectively if the SCADA data is saved together with the structural responses. In this process it is imperative for post-processing that both are given the same time-stamps.

Although the effectiveness and conclusions from the fatigue measurement system will only become available after years of measuring, the preliminary results of a test set-up will lead to confidence in usefulness of the measurement output. However, a database of multiple foundations across wind farms could increase the reliability of predictions by increasing the sample size. Further an inclusion of SCADA data to the fatigue life

prediction will take information about the relation between the environmental conditions and the measured fatigue into account and will thus put the fatigue measurements in perspective, this could drive down the uncertainty of the predictions.

Recommendations for Further Research

In the current research it has been chosen to investigate MDE configurations that were identical for both the For-Aft and the Side-Side directions. As the the structural response in the SS direction shows far less high frequency content, it might be interesting to investigate the influence of selecting different configurations for the reconstruction of the SS response than for the response in the FA direction.

One of the conclusions of this thesis is that the Multi-Band MDE is a very good strain estimation tool for noise-free input, thus research in extending the method to input containing measurement noise could lead to interesting results. This thesis proved that, for the investigated load cases, the weighted LS algorithm is not a valuable extension to the Multi-Band MDE method, however a multitude of other estimation algorithms has been designed. Kalman-type state estimators allow for regularisation regarding both model and measurement errors, giving the algorithms more information to find the optimal solutions. Model errors present themselves as errors in the utilised mode shapes and measurement errors are introduced by noise on the measurement signal or ill-calibrated sensors.

The filtering method used in this thesis,where both the estimated and control values were filtered to obtain equal phase distortions, is chosen to simulate the method proposed by Iliopoulos et al. [38]. However zero-phase filtering techniques are available which allow for a direct comparison between the estimated and control signals. Furthermore, the higher-order filters could be used to ensure a sharper drop-off beyond the cut-off frequencies, this may require to apply some additional manipulations like windowing to counter the transients introduced by higher order filters.

Bibliography

[1] IEC 61400-13. Wind turbines - part 13: Measurements of mechanical loads. Technical report, IEC, 2015.

[2] IEC 61400-3. Wind turbines - part 3: Design requirements for offshore wind turbines. Technical report, IEC, 2009.

[3] O. Adedipe, F. Brennan, and A. Kolios. Review of corrosion fatigue in offshore structures: Present status and challenges in the offshore wind sector. *Renewable and Sustainable Energy Reviews*, 61:141–154, 2016.

[4] M. López Aenlle, L. Hermanns, P. Fernández, and A. Fraile. Stress estimation in a scale model of a symmetric two story building. In *Proc. 5th IOMAC*, 2013.

[5] ANSYS. Ansys help. Software Documentation, 2016.

[6] P. Avitable and P. Pingle. Prediction of full field dynamic strain from limited sets of measured data. *Shock and Vibration*, 19:765–785, 2012.

[7] H. Bang, S. Ko, M. Jang, and H. Kim. Shape estimation and health monitoring of wind turbine tower using an fbg sensor array. In *Proc. of the 2012 IEEE International Instrumentation and Measurement Technology Conference*, pages 496–500, 2012.

[8] M. Benedetti, V. Fontanari, and D. Zonta. Structural health monitoring of wind towers: Remote damage detection using strain sensors. *Smart Materials and Structures*, 20, 2011.

[9] M. Benedetti, V. Fontanari, and L. Battisti. Structural health monitoring of wind towers: Residual fatigue life estimation. *Smart Materials and Structures*, 22(4), 2013.

[10] S. Bhattacharya. Challenges in design of foundation for offshore wind turbines. *Institution of Engineering and Technology Journal*, pages 1–9, 2014.

[11] A. Bossanyi. Theory manual - gh bladed. Technical report, Garrad Hassan and Partners Ltd., 2010.

[12] A. Brandt. *Noise and Vibration Analysis: Signal Analysis and Experimental Procedures*. John Wiley & Sons, 2011.

[13] R. Brincker, L. Zhang, and P. Andersen. Modal identification of output-only systems using frequency domain decomposition. *Smart Materials and Structures*, 10:441–445, 2001.

[14] T. Camp, M. Morris, R. van Rooij, J. van der Tempel, M. Zaaijer, A. Henderson, K. Argyriadis, S. Schwartz, H. Just, W. Grainger, and D. Pearce. Design methods for offshore wind turbines at exposed sites: Final report. Technical report, Garrad Hassan and Partners Ltd., 2003.

[15] D. Coronado and K. Fischer. Condition monitoring of wind turbines: State of the art, user experiences and recommendation. Technical report, Fraunhofer Institute for Wind Energy and Energy System Technology, 2015.

[16] M. Damgaard, L. Ibsen, L. Andersen, and J. Andersen. Cross-wind modal properties of offshore wind turbines identified by full scale testing. *Journal of Wind Engineering and Industrial Aerodynamics*, 116: 94–108, May 2013.

[17] J. Van der Tempel. *Design of Support Structures for Offshore Wind Turbines (Doctoral dissertation)*. PhD thesis, Delft University of Technology, 2006.

[18] C. Devriendt, F. Magalhães, W. Weijtjens, G. De Sitter, Á. Cunha, and P. Guillaume. Structural health monitoring of offshore wind turbines using automated operational modal analysis. *Structural Health Monitoring*, 13(6):644–659, 2014.

[19] L. Eliassen, E. Sæta, and J. Krokstad. Measurement campaign of a large rotor wind turbine. *Energy Procedia*, 80:189–167, 2015.

[20] P. Faulkner and M. Hassel. Structural health monitoring systems on offshore wind turbine structures. In *Proc. of EWEA 2013*, 2013.

[21] P. Faulkner, P. Cutter, and A. Owens. Structural health monitoring systems in difficult environments - offshore wind turbines. In *Proc. European Workshop on Structural Health Monitoring-VI*, page 1–7, 2012.

[22] FBGS. Fbg - fiber bragg grating principle. `http://www.fbgs.com/technology/fbg-principle/`, 2017. [FBGS Draw Tower Gratings; Online; accessed 20-1-2017].

[23] T. Fischer, W. de Vries, and B. Schmidt. Upwind wp4 design basis - k13 shallow water site. Technical report, UpWind, April 2010.

[24] K. Freeman, G. Hundleby, C. Nordstrom, A. Roberts, B. Valpy amd C. Willow, P. Totaro, M. Ayuso, and F. Boshell. Innovation outlook - offshore wind. Technical report, IRENA, 2016.

[25] T. Gangopadhyay, M. Majumder, A. Chakraborty, A. Dikshit, and D. Bhattacharya. Fibre bragg gratings strain sensor and study of its packaging material for use in critical analysis on steel structure. *Sensors and Actuators A: Physical*, 150:78–86, 2009.

[26] DNV GL. Study on uk offshore wind variability. Technical report, The Crown Estate Commissioners, 2016.

[27] N. Gordon, D. Salmond, and A. Smith. Novel approach to nonlinear/non-gaussian bayesian state estimation. *Radar and Signal Processing, IEE Proceedings F*, 140(2):107–103, May 1993.

[28] GWEC. Global wind report - annual market updat 2016. Technical report, GWEC, 2016.

[29] G.Welch and G. Bishop. An introduction to the kalman filter. Technical report, University of North Carolina at Chapel Hill, 2006.

[30] H. Han, J. Wang, X. Meng, and H. Liu. Analysis of the dynamic response of a long span bridge using gps/accelerometer/anemometer under typhoon loading. *Engineering Structures*, 122:238–250, September 2016.

[31] M. Hansen. *Aerodynamics of Wind Turbines*. Earthscan, London, United Kingdom, 2008.

[32] M. Hansen, P. FuglSang, K. Thomson, and T. Knudsen. Two methods for estimating aeroelastic damping of operational wind turbine modes from experiments. *Wind Energy*, 9:179–191, January 2006.

[33] H. Hjelm, R. Brincker, J.Graugaard-Jensen, and K.Munch. Determination of stress histories in structures by natural input modal analysis. In *Proc. IMAC-XXIII*, 2005.

[34] A. Ho and A. Mbistrova. The european offshore wind industry - key trends and statistics 2016. Technical report, WindEurope, Januari 2017.

[35] K. Hoffmann. *An Introduction to Stress Analysis and Transducer Design using Strain Gauges*. HBM, 2012.

[36] W. Hu, S. Thöns, R. Rohrmann, S. Said, and W. Rücker. Vibration-based structural health monitoring of a wind turbine system. part I: Resonance phenomenon. *Engineering Structures*, 89:260–272, 2015.

[37] A. Iliopoulos, R. Shirzadeh, W. Weijtjens, P. Guillaume, D. Van Hemelrijck, and C. Devriendt. A modal decomposition and expansion approach for prediction of dynamic responses on a monopile offshore wind turbine using a limited number of vibration sensors. *Mechanical Systems and Signal Processing*, 68-69:84–104, 2016.

[38] A. Iliopoulos, W. Woutjens, D. Van Hemelrijck, and C. Devriendt. Fatigue assessment of offshore wind turbines on monopile foundations using multi-band modal expansion. *Wind Energy*, 2017.

[39] Columbia Research Laboratories Inc. Force balance sensor technology. `https://www.crlsensors.com/pdf/techpapers_forcebalance.pdf`, 2017. [CLR Sensors; Online; accessed 4-1-2017].

[40] C. Inglis. Stresses in a plate due to the presence of cracks and sharp corners. *Transactions of the Institute of Naval Architects*, 55:219–241, 1913.

[41] H. Jo and B. Spencer Jr. Multi-metric model based structural health monitoring. In *Proc. SPIE:9061*, pages 90611F–1 – 90611F–10, 2014.

[42] S. Julier and J. Uhlmann. A new extension of the kalman filter to nonlinear systems. In *Proc. of the International Symposium on Aerospace/Defense Sensing, Simulation and Controls*, page 32, 1997.

[43] J. Kaimal, J. Wyngaard, Y. Izumi, and O. Cote. Spectral characteristics of surface-layer turbulence. *Quarterly Journal of the Royal Meteorological Society*, 98:563–598, 1972.

[44] R. Kalman and R. Bucy. New results in linear filtering and preduction theory. *Journal of Basic Engineering*, 83(3):95–108, March 1961.

[45] D. Kammer. Sensor placement for on-orbit modal identification and correlation of large space structures. *Journal of Guidance, Control and Dynamics*, 14(2):251–259, 1996.

[46] D. Kaufer and P. Cheng. Validation of an integrated simulation method with high-resolution load measurements of the offshore wind turbine repower 5m at alpha ventus. *Journal of Ocean and Wind Energy*, 1(1):30–40, February 2014.

[47] T. Kleckers and B. Günther. Optical versus electrical strain gauges: A comparison. Technical report, HBM Measurements, 2007.

[48] J. Kormylo and V. Jain. Two-pass recursive digital filter with zero phase shift. *IEEE Transactions on Acoustics, Speech and Signal Processing*, 22(5):384–387, October 1974.

[49] C. Koukara. *Validated Loads Prediction Models for Offshore Wind Turbines for Enhanced Component Reliability (Doctoral dissertation)*. PhD thesis, Technical University of Denmark, 2014.

[50] M. Kühn. *Dynamics and Design Optimisation of Offshore Wind Energy Conversion Systems (Doctoral dissertation)*. PhD thesis, Delft University of Technology, 2001.

[51] P. Lako and M. Koyama. Wind power - technology brief. Technical report, IEA-ETSAP & IRENA, March 2016.

[52] Y. Lee, M. Barkey, and H. Kang. *Metal Fatigue Analysis Handbook*. Butterworth-Heinemann, 2012.

[53] I. Lotsberg. *Fatigue Design of Marine Structures*. Cambridge University Press, 32 Avenue of the Americas, New York, 2016.

[54] R. Lucena and J. Dos Santos. Structural health monitoring using time reversal and cracked rod spectral element. *Mechanical Systems and Signal Processing*, 79:86–98, 2016.

[55] K. Maes, A. Iliopoulos, W. Weijtjens, C. Devriendt, and G. Lombaert. Dynamic strain estimation for fatigue assesment of an offshore monopile wind turbine using filtering and modal expansion algorithms. *Mechanical Systems and Signal Processing*, 76-77:592–611, 2016.

[56] M. Majumder, T. Gangopadhyay, A. Chakraborty, K. Dasgupta, and D. Bhattacharya. Fibre bragg gratings in structural health monitoring - present status and applications. *Sensors and Actuators A: Physical*, 147: 150–164, 2008.

[57] S. Mariani and A. Ghisi. Unscented kalman filtering for nonlinear structural dynamics. *Nonlinear Dynamics*, 49:131–150, 2007.

[58] M. Martinez-Luengo, A. Kolios, and L. Wang. Structural health monitoring of offshore wind turbines: A review through the statistical pattern recognition paradigm. *Renewable and Sustainable Energy Reviews*, 64:91–105, 2016.

[59] MATLAB. Signal processing toolbox - user's guide. Technical report, MathWorks, 2016.

[60] M. Matsuishi and T. Endo. Fatigue of metals subjected to varying stress. Presented to Japan Society of Mechanical Engineers, 1968.

[61] M. Mieloszyk and W. Ostachowicz. An application of structural health monitoring system based on fbg sensors to offshore wind turbine support structure model. *Marine Structures*, 51:65–86, 2016.

[62] M. Miner. Cumulative damage in fatigue. *Journal of Applied Mechanics*, 67:A159–A164, 1945.

[63] J. Mottershead, M. Link, and M. Friswell. The sensitivity method in finite element model updating: A tutorial. *Mechanical Systems and Signal Processing*, 25(7):2275–2296, October 2011.

[64] Adam Nieslony. Rainflow counting algorithm. `https://nl.mathworks.com/matlabcentral/fileexchange/3026-rainflow-counting-algorithm`, 2014. [Rainflow Counting Algorithm that was implemented in Matlab; Online; accessed 11-01-2016].

[65] R. Palanisamy, S. Cho, H. Kim, and S. Sim. Experimental validation of alman filter-based strain estimation in structures subjected to non-zero mean input. *Smart Structures and Systems*, 15(2):489–503, 2015.

[66] C. Papadimitriou. Optimal sensor placement methodology for parametric identification of structural systems. *Journal of Sound and Vibration*, 278:923–947, 2004.

[67] C. Papadimitriou, C. Fritzen, P. Kraemer, and Ntotsios E. Fatigue predictions in entire body of metallic structures from a limited number of vibration sensors using kalman filtering. *Structural Control and Health Monitoring*, 18(5):554–573, 2011.

[68] B. Peeters, H. Van der Auweraer, P. Guillaume, and J. Leuridan. The polymax frequency-domain method: a new standard for modal parameter estimation? *Shock and Vibration*, 11:395–409, 2004.

[69] Rambøll. Gemini offshore wind farms - design report - design basis part c. Technical report, Rambøll Group A/S, July 2013. Document No.: 11533019/340_0001(5).

[70] Rambøll. Gemini offshore wind farms - drawing - monopile, position zec5. Technical report, Rambøll Group A/S, April 2014. Drawing No.: 113319-GM-WTG-PS-02-021.

[71] Rambøll. Gemini offshore wind farms - design report - attachment report. Technical report, Rambøll Group A/S, July 2015. Document No.: 11533019/340_0016(6).

[72] Rambøll. Gemini offshore wind farms - design report - mp-tp connection. Technical report, Rambøll Group A/S, November 2015. Document No.: 11533019/340_0005(3).

[73] Rambøll. Gemini offshore wind farms - design report - natural frequency analysis. Technical report, Rambøll Group A/S, November 2015. Document No.: 11533019/340_0003(3).

[74] Rambøll. Gemini offshore wind farms - design report - computer model. Technical report, Rambøll Group A/S, November 2015. Document No.: 11533019/340_0013(3).

[75] Rambøll. Gemini offshore wind farms - design report - time domain fatigue analysis. Technical report, Rambøll Group A/S, November 2015. Document No.: 11533019/340_0004(2).

[76] DNVGL RP-C203. Fatigue design of offshore steel structures. Technical report, DNV GL, 2014.

[77] S. Schafhirt, A. Page, G. Eiksund, and M. Muskulus. Influence of soil parameters on the fatigue lifetime of offshore wind turbines with monopile support structure. *Energy Procedia*, 94:347–356, 2016.

[78] R. Shirzadeh, C. Devriendt, M. Bidakhvidi, and P. Guillaume. Experimental and computational damping estimation of an offshore wind turbine on a monopile foundation. *Journal of Wind Engineering and Industrial Aerodynamics*, 120:96–106, 2013.

[79] Siemens. Swt4.0-130 gemini tower design document. Technical report, Siemens Wind Power A/S, June 2013. Document No.: OEN DES TLS12-40-6153-11.

[80] A. Smyth and M. Wu. Multi-rate kalman filtering for the data fusion of displacement and acceleration response measurements in dynamic system monitoring. *Mechanical Systems and Signal Processing*, 21: 706–723, 2007.

[81] H. Sohn. Effects of environmental and operational variability on structural health monitoring. *Philosophical Transactions of the Royal Society A*, 365(1851):539–560, 2007.

[82] S. Stiros. Errors in velocities and displacements deduced from accelerographs: An approach based on the theory of error propagation. *Soil Dynamics and Earthquake Engineering*, 28:415–420, 2008.

[83] L. Sun, H. Li, L. Ren, and Q. Jin. Dynamic response measurement of offshore platform model by fbg sensors. *Sensors and Actuators A: Physical*, 136:527–579, 2007.

[84] Y. Thong, M. Woolfson, J. Crowe, B. Hayes-Gill, and D. Jones. Numerical double integration of acceleration measurements in noise. *Measurement*, 36:73–92, 2004.

[85] P. Vardanega, G. Webb, P. Fidler, and C. Middleton. *Innovative Bridge Design Handbook*. Butterworth-Heinemann, The Boulevard, Langford Lane, Kidlington, Oxford OX5 1GB, UK, 2016.

[86] P. Veers. Three-dimensional wind simulation. Technical report, Sandia National Laboratories, 1988.

[87] W. Weijtjens, T. Verbelen, G. De Sitter, and C. Devriendt. Foundation structural healt monitoring of an offshore wind turbine - a full-scale case study. *Structural Health Monitoring*, 15(4):389–402, 2016.

[88] Q. Xia and F. Quail. Principles and validation of strain gauges shunt design for large dynamic strain measurement. *Sensors and Actuators A: Physical*, 241:124–134, 2016.

[89] J. Yi, J. Park, S. Han, and K. Lee. Modal identification of a jacket-type offshore structure using dynamic tilt responses and investigation of tidal effects on modal properties. *Engineering Structures*, 49:767–781, 2013.

[90] T. Yi, H. Li, and M. Gu. Optimal sensor placement for structural health monitoring based on multiple optimization strategies. *The Structural Design of Tall and Special Buildings*, 20:881–900, 2011.

[91] X. Zou, P. Thiruvenkatanathan, and A. Seshia. A high-resolution micro-electro-mechanical resonant tilt sensor. *Sensors and Actuators A: Physical*, 220:168–177, December 2014.

A

Basis of Design

A.1. Lumped States

Kühn describes that if the wave loads on the structure are inertia dominated, the stress range is roughly proportional to H_s [50]. The Keulegan Carpenter number can be used to determine the whether wave loads are drag or inertia dominated. The damage will be proportional to H_s^m and $\frac{1}{T_z}$, where H_s is the significant wave height in meters, m is the Wöhler constant and T_z is the zero crossing period. Thus H_s^m describes the amplitude of the loading and $1/T_z$ the number of cycles. Lumped values of the significant wave height and zero-crossing period can be computed through the following equations:

$$\hat{H}_{s,0} = \left(\frac{\sum_j p_j H_{s,j}^m}{\sum_j p_j} \right)^{\frac{1}{m}} \qquad \hat{T}_{z,0} = \frac{\sum_j p_j}{\sum_j \frac{p_j}{T_{z,j}}}$$

Where p_j is the probability of occurrence for a particular sea state. The lumped sea states computed with Kühn's method can drastically safe the amount of computing time required for an FLS analysis.

Table A.1: Lumped scatter diagram of K13 Shallow Water Site from the UpWind design basis [23], occurrence is Weibull fitted, cases that are used in this study are highlighted in green.

V [m/s]	**TI [%]**		**H_s [m]**	**T_p [s]**	**Peakedness**		**f [%]**	**occ./year [hrs]**
	Normal	Extreme			Fatigue [-]	Extreme [-]		
2	29.2	99.3	1.07	6.03	1.0	3.3	7.07	619.50
4	20.4	53.1	1.10	5.88	1.0	3.3	11.11	972.97
6	17.5	37.1	1.18	5.76	1.0	3.3	14.07	1232.33
8	16.0	30.0	1.31	5.67	1.0	3.3	14.96	1310.09
10	15.2	25.4	1.48	5.74	1.0	3.3	14.06	1231.75
12	14.6	22.3	1.70	5.88	1.0	3.3	11.97	1048.50
14	14.2	20.1	1.91	6.07	1.0	3.3	9.34	818.3
16	13.9	18.5	2.19	6.37	1.0	3.3	6.74	590.01
18	13.6	17.2	2.47	6.71	1.0	3.3	4.51	394.97
20	13.4	16.1	2.76	6.99	1.0	3.3	2.81	246.33
22	13.3	15.3	3.09	7.40	1.0	3.3	1.64	143.48
24	13.1	14.6	3.42	7.80	1.0	3.3	0.89	78.20
26	12.0	14.0	3.76	8.14	1.0	3.3	0.46	39.94
28	11.91	13.5	4.17	8.49	1.0	3.3	0.22	19.13
30	11.8	13.1	4.46	8.86	1.0	3.3	0.10	8.61
32	11.8	12.7	4.79	9.12	1.0	3.3	0.04	3.64
34-42	11.7	12.3	4.90	9.43	1.0	3.3	0.04	3.69

B

Gemini Design Documents

B.1. Primary Steel

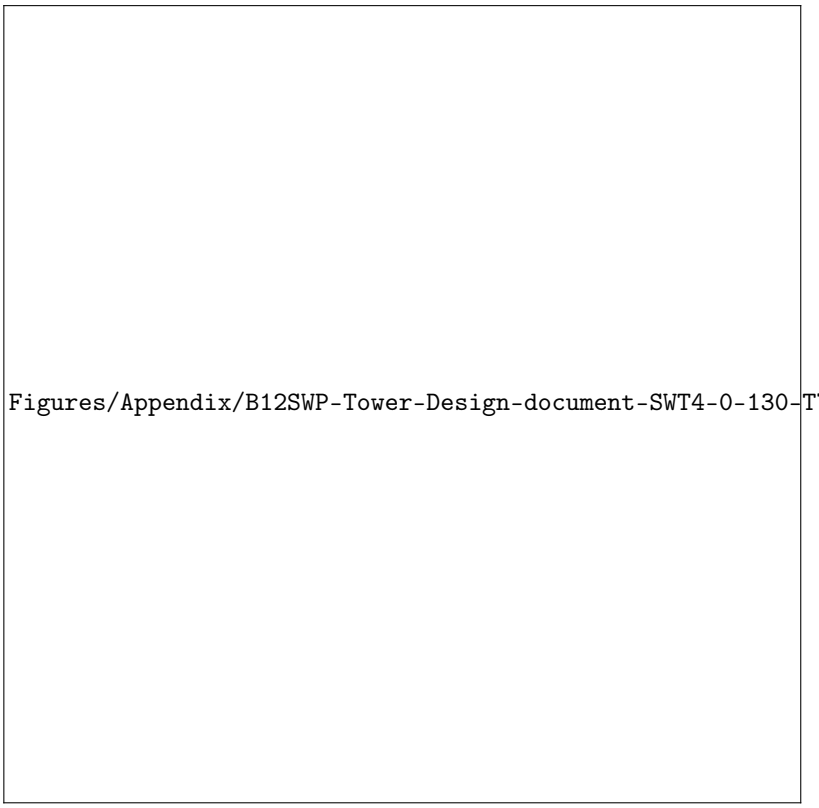

Figure B.1: Design document for the tower structure of the Siemens 4 MW wind turbine installed at Gemini. [79]

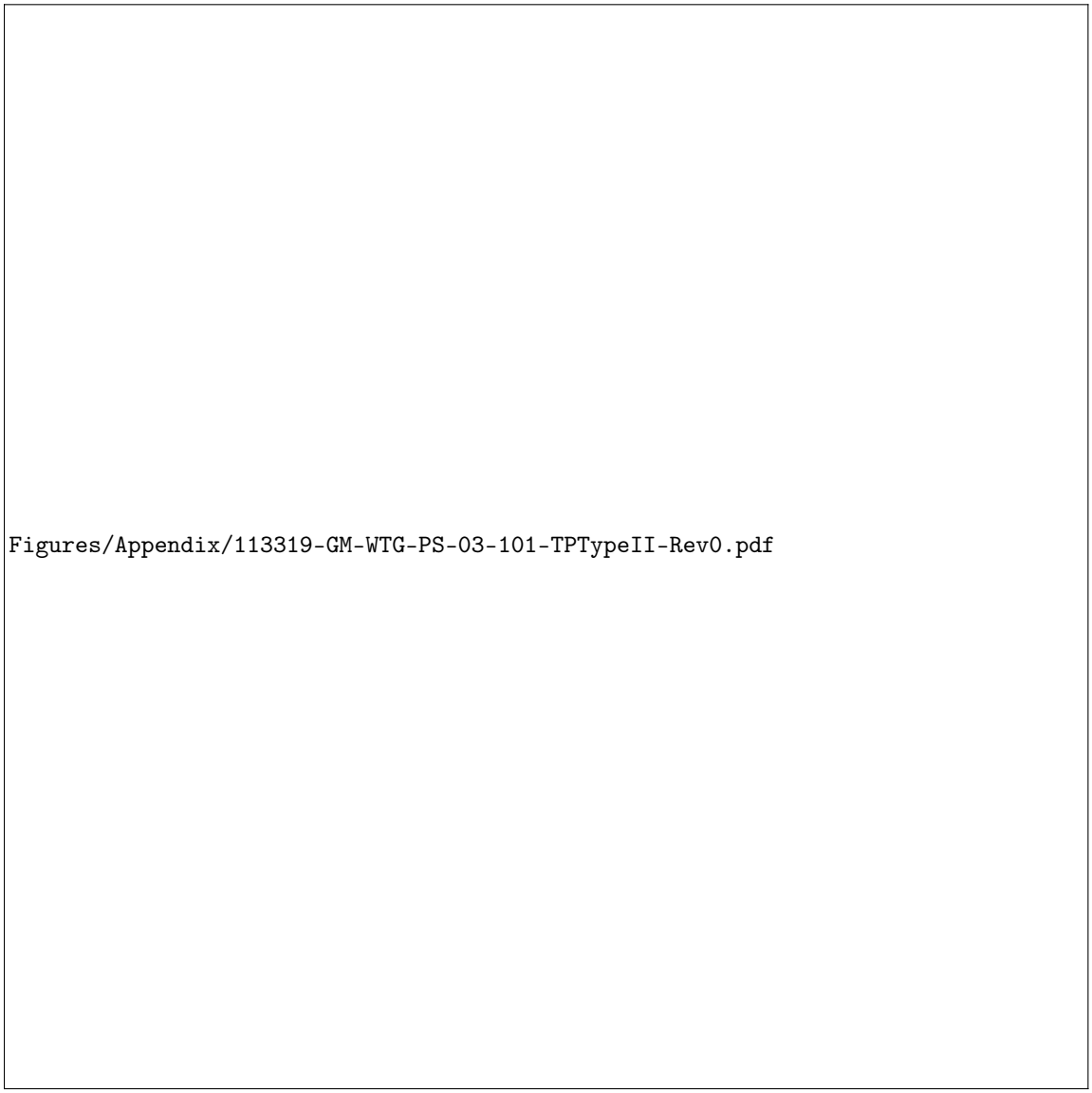

Figure B.2: Design drawing for the transition piece structure of the ZEC5 foundation. [70]

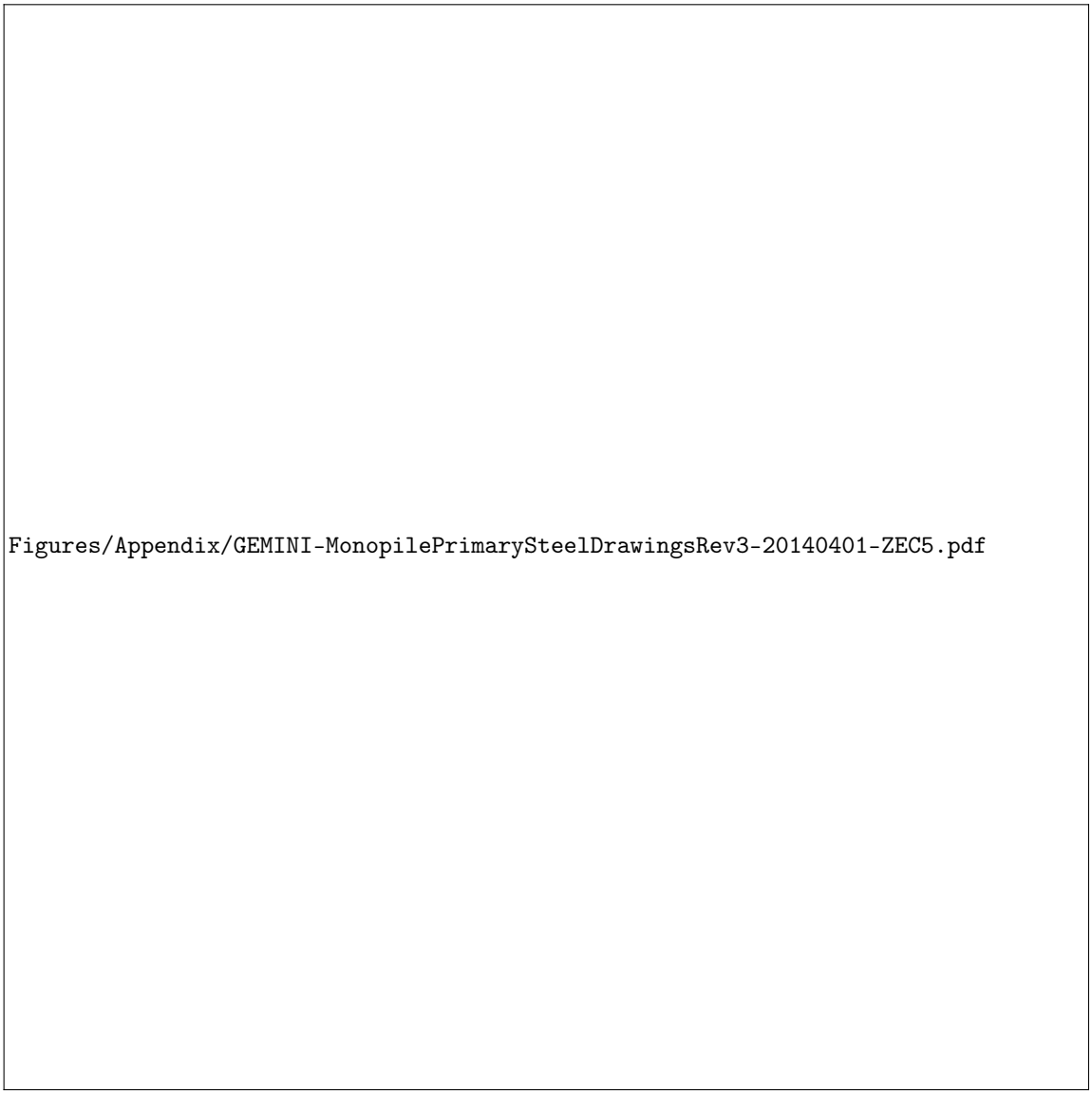

Figure B.3: Design drawing for the monopile structure of the ZEC5 foundation. [70]

B.2. Secondary Steel

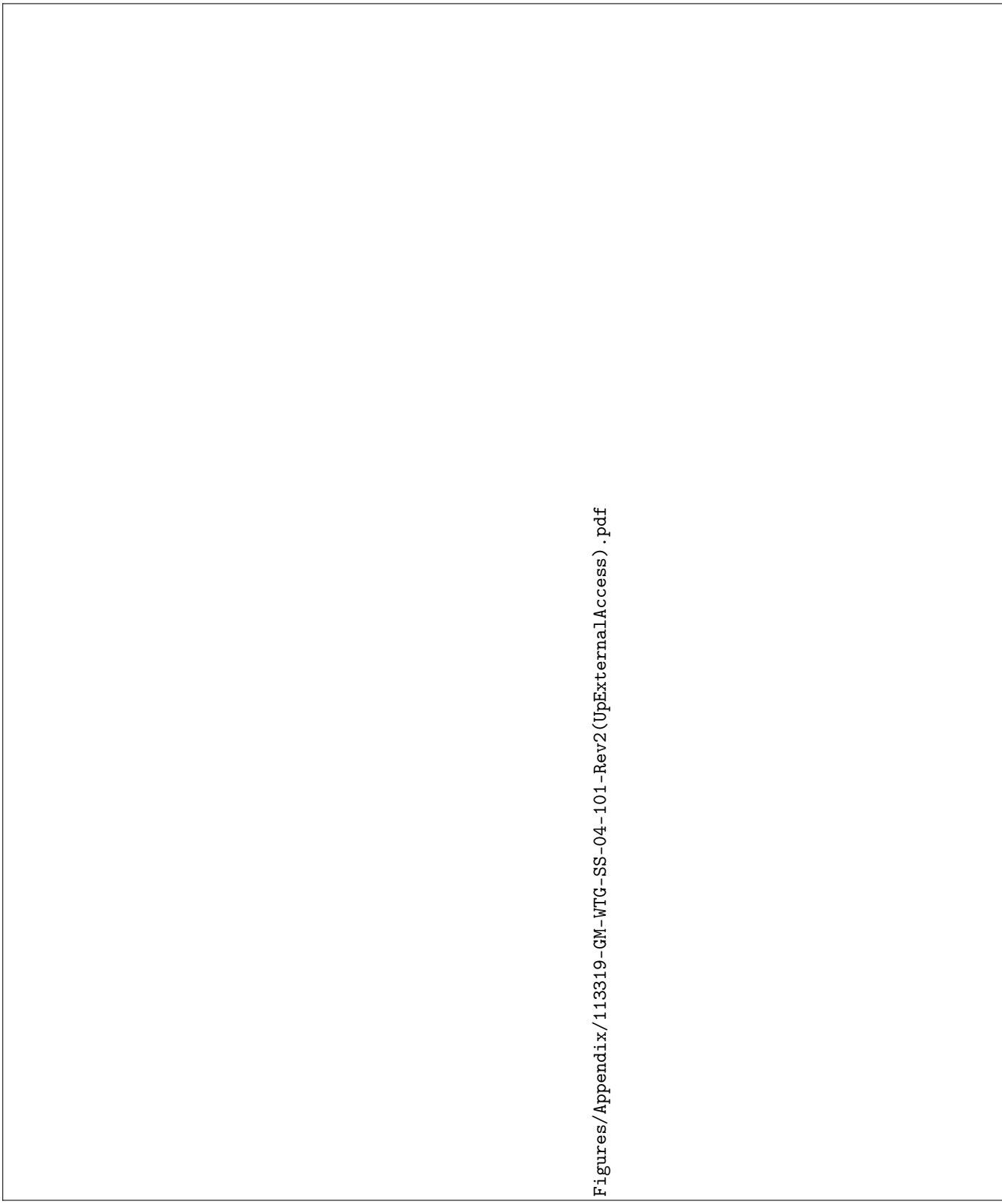

Figure B.4: Design drawing for the Upper External Access Ladder of the ZEC5 foundation.

B.3. Soil Parameters

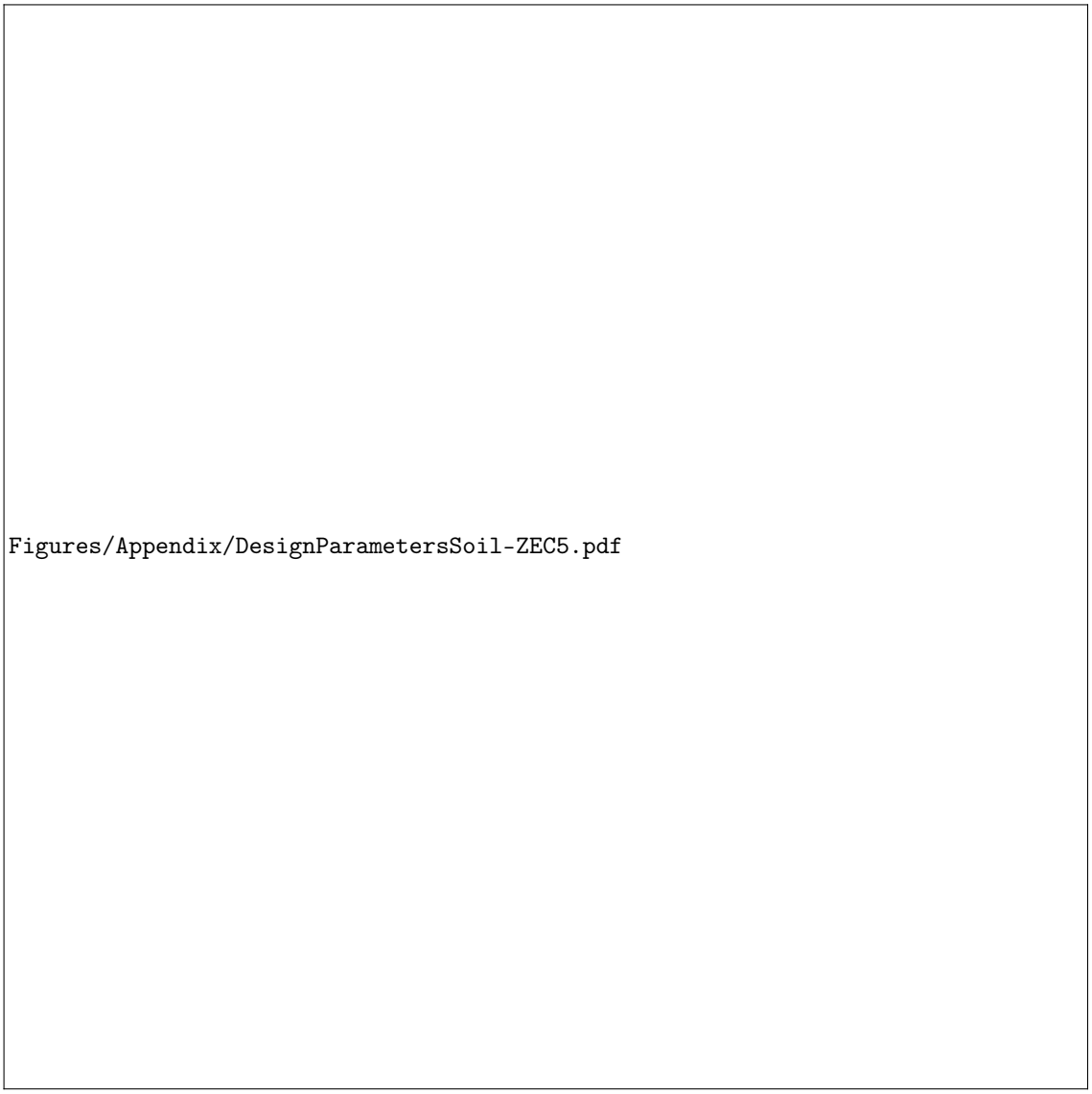

Figure B.5: Soil parameters for the ZEC5 foundation.

B.3.1. P-Y Curves

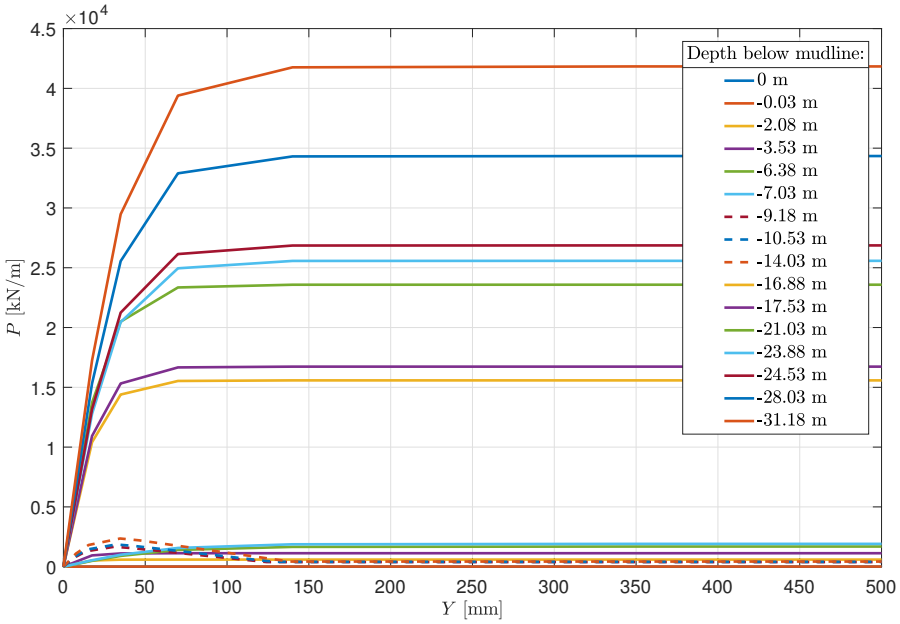

Figure B.6: $P - y$ curves at top of soil layers as defined in the report by Rambøll [71].

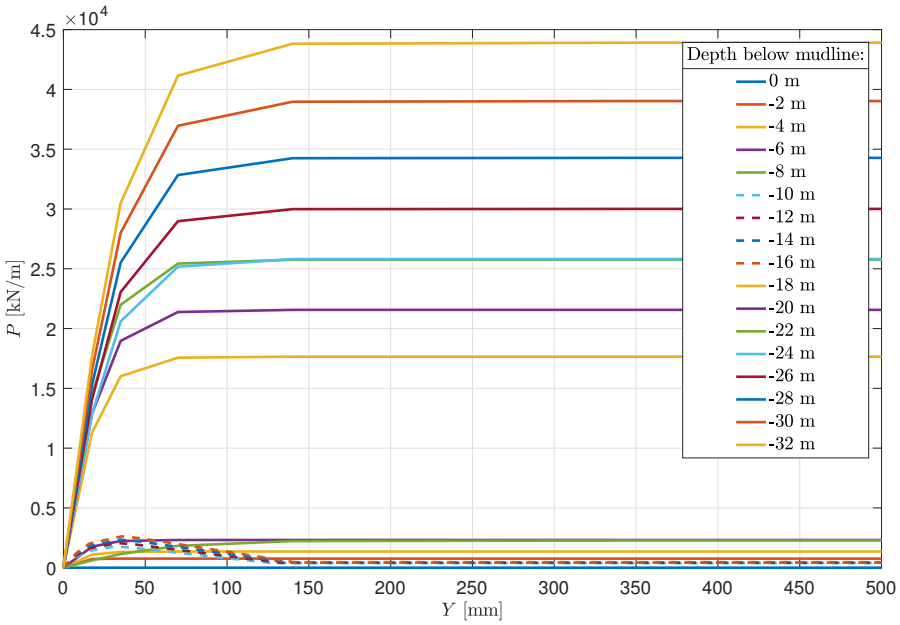

Figure B.7: Discrete $P - y$ curves at interpolated points (0.5 m interval).

C

Model Definition for Data Generation

C.1. Turbine Characteristics

Table C.1: Gross properties chosen for the NREL 5-MW baseline wind turbine

Item	Value	Unit
Rating	5	MW
Rotor Orientation	Upwind	-
Configuration	3	blades
Drivetrain	High speed, Multiple-stage gearbox	-
Cut-in/Rated/Cut-out wind speed	3/11.4/25	m/s
Cut-in/Rated rotor speed	6.9/12.1	rpm
Rated Tip Speed	80	m/s

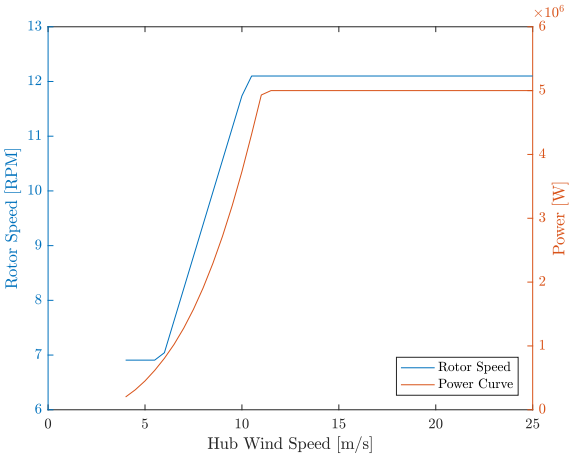

Figure C.1: Power curve for the NREL 5MW turbine, along with the rotor speeds

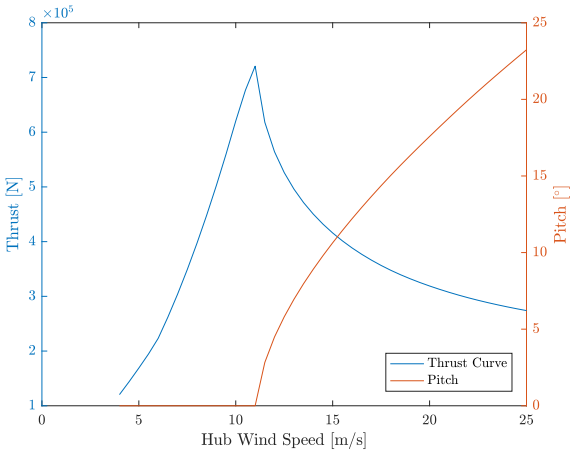

Figure C.2: Thrust curve for the NREL 5MW turbine, along with the pitch angle of the blades

C.2. RNA

C.2.1. Rotor

Table C.2: Overview of the Rotor specifications

Item	Value	unit	Symbol in Figure C.3
Blade length	61.64	m	
Blade mass	17723	kg	
Root length	1.5	m	L
Diameter	3.5	m	D
Drag coefficient	0	-	
Spinner diameter	3	m	S
Hub mass (incl. internals)	56780	kg	
Hub centre of mass	0	m	H
Rotor diameter	126	m	
Overhang	5	m	

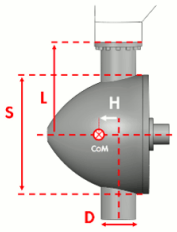

Figure C.3: Reference for the hub specifications from Bladed

C.2.2. Nacelle

Table C.3: Overview of the Hub specifications

Item	Value	unit	Symbol in Figure C.3
Length	6	m	
Height	2.5	m	
Width	2.5	m	
Drag coefficient	0	-	
Mass (incl. internals)	240000	kg	

C.3. Mass Totals

Table C.4: Overview of the mass totals for the Bladed Model (left) and ANSYS model (right)

Bladed				
Component	**Mass [kg]**	**C.o.G [m]**		
		x	**y**	**z**
Rotor	109950	-5.0	0	91.29
Nacelle	240000	-1.9	0	89.09
Tower				
Foundation				

ANSYS				
Component	**Mass [kg]**	**C.o.G [m]**		
		x	**y**	**z**
Rotor	109950	-5.0	0	91.29
Nacelle	240000	-1.9	0	89.09
Tower				
Foundation				

D

SCADA data from Data Generation

The plots presented here give an insight in the SCADA regarding the four wind and wave climates that are considered, it should be noted that while the rotor speed for a wind speed of 2 m/s is not zero it is lower than the cut-in speed of 6.9 rpm, see Table C.2. Furthermore, it was chosen to present the wave climates in the frequency domain as it gives a clearer overview of the amplitude distributions, which is obscured by the random phase angles in the time domain.

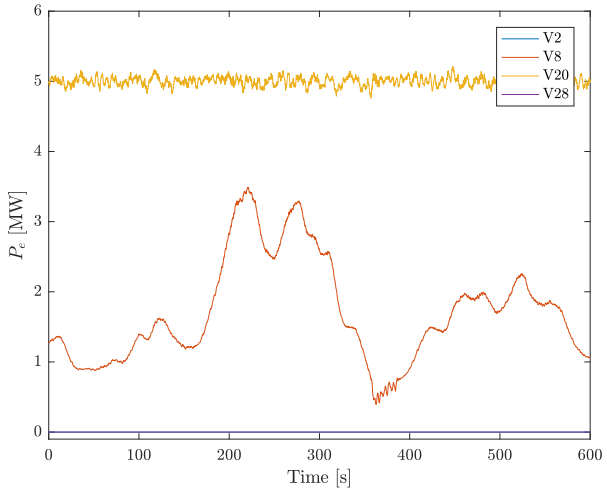

Figure D.1: Comparison of the hub height wind speed time history for different wind speeds considered.

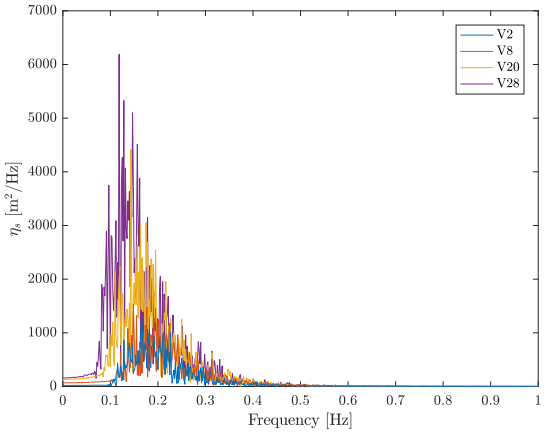

Figure D.2: Frequency domain representation of the time history for the surface elevation for different wind speeds considered.

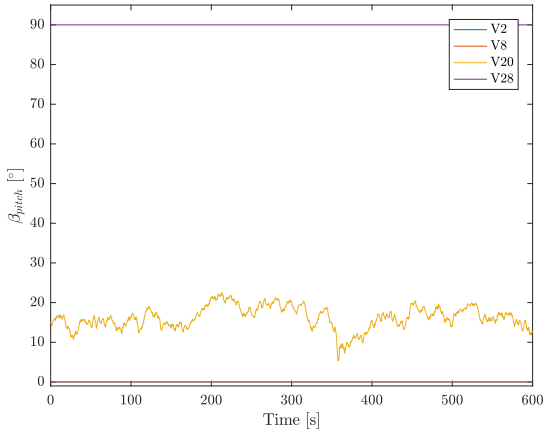

Figure D.3: Comparison of blade pitch time history for the different wind speeds considered

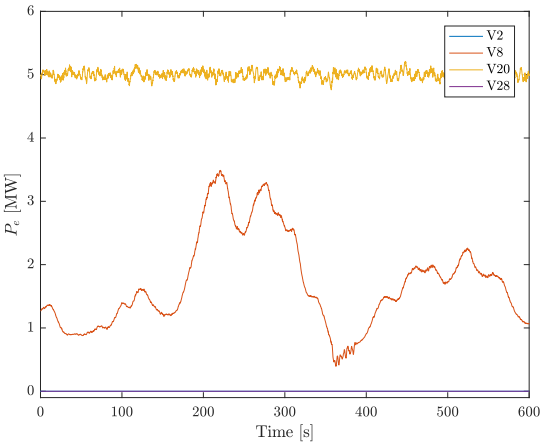

Figure D.4: Comparison of the generated power time history for different wind speeds considered.

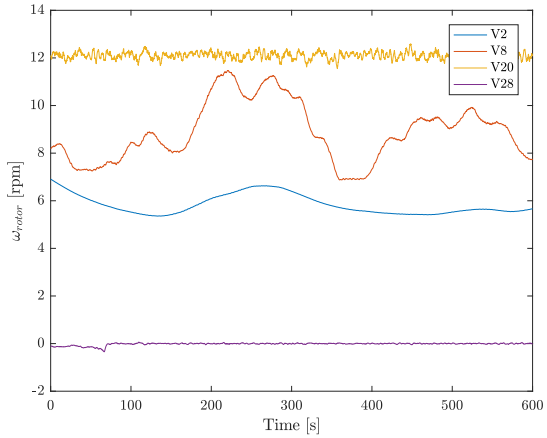

Figure D.5: Comparison of blade rotor speed time history for the different wind speeds considered

E

Validation of Computational Tools

E.1. Fatigue Damage and Sensitivity to Stress Ranges

In a fatigue analysis from estimated stress it is extremely important to make accurate estimations of the stress history that is taken as input. This section will elaborate on the reason why and show that even computed signals that seem to match the original signal well can give a wrong image of the actual fatigue damage that has been inflicted.

First of all the S-N design curve has to be discussed. S-N curves are essentially stress-life diagrams, where stress range versus cycles to failure are set out. The curves have been set up through experimental work, where a relation between the stress range $\Delta\sigma_i$ of a cycle, i.e. loading an unloading, and the number of cycles to failure N_i was determined. Then a regression curve is fitted trough the empirical data of specimen that were subjected to stress cycles until they failed or until the number of cycles passed a limit for which it was judged reasonable to stop testing. Design codes (e.g. DNV-GL RP-C203 [76]) often contain several different S-N design curves for different details of a structure, depending on technological factors, local geometry and load direction; since safety margins are introduced, using the design curves leads to a failure probability of 2.3 % after N_i cycles. Equation E.1 shows the relation between the stress ranges and number of cycles. Where N is the number of cycles to failure, $\Delta\sigma$ is the amplitude of the the stress cycles, m is the Wöhler exponent and A is a constant. A is a constant for each S-N curve, but depends on the type of detail the S-N curve is set up for. Equation E.2 is the same relation but now $\Delta\sigma$ is a function of N, m and A. On a log-log scale this can be drawn as a straight line (see Figure E.1). However, to fit the measured results a fatigue limit is introduced, this means that for low amplitude stress cycles the slope of the curve is changed to represent a lower sensitivity to fatigue.

Corrosion

Offshore structures are placed in harsh conditions when it comes to corrosion. Especially the area of the structures that is in the so-called splash-zone where the wave action is at its roughest. There are several ways to counter corrosion, the three most widely used in the offshore industry are extra wall thickness, protective coating and cathodic protection [3]. Depending on the utilised protection method and the assumptions following from that method an appropriate S-N design curve should be selected from the design codes.

$$N(\Delta\sigma)^m = A \tag{E.1}$$

$$\log\Delta\sigma = -\frac{1}{m}\log N + \frac{1}{m}\log A \tag{E.2}$$

[1] $\mathbf{N \leq 10^6}$ and $\mathbf{N > 10^6}$ for the free corrosion curves: DNV-xx-W

Table E.1: Parameters for the S-N curves prescribed by Rambøll [71] and DNVGL [76].

S-N curve	$N \leq 10^7$ cycles[1]		$N > 10^7$ cycles[1]		Fatigue limit at 10^7 cycles[1]	Thickness exponent
	m_1	$\log \bar{a}_1$	m_2	$\log \bar{a}_2$		k
DNV-C1-A	3.0	12.449	5.0	16.081	65.50	0.10
DNV-D-A	3.0	12.164	5.0	15.606	52.63	0.20
DNV-C1-W	3.0	12.049	5.0	16.081	65.50	0.10
DNV-D-W	3.0	11.764	5.0	15.606	52.63	0.20

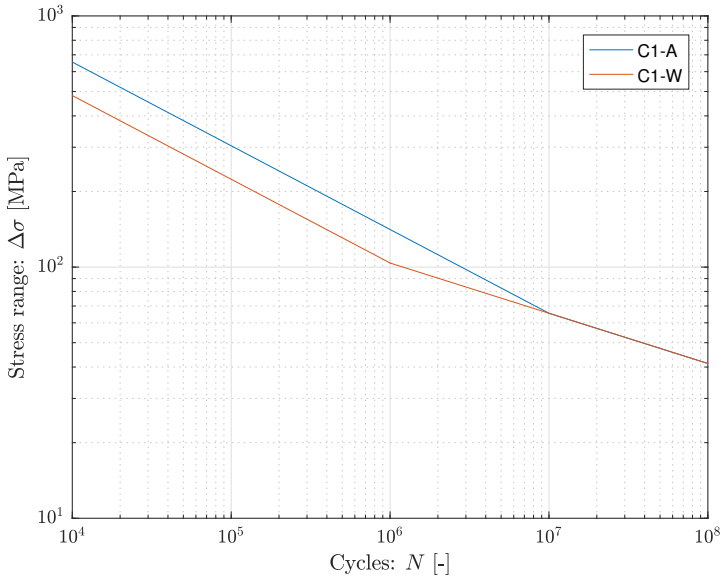

Figure E.1: air (blue) and seawater with cathodic protection (orange) S-N curves for a detail of type C1 from the DNVGL design code on fatigue analysis of marine structures [76], plotted on a log-log scale.

E.1.1. Fatigue Damage Analysis

In order to translate measured stress cycles to fatigue damage the Miner-Palmgren rule is combined with the S-N curves, the Miner-Palmgren rule states that every cycle in a constant amplitude stress range $\Delta\sigma_i$ can be interpreted as $D_i = 1/N_i$, where D_i is the fatigue damage per cycle and N_i is the number of cycles to failure for the stress range $\Delta\sigma_i$, found from the S-N curve. Now if all cycles of a stress time history are known, the sum can be taken over the fatigue for each single cycle to find the total fatigue damage [62], this is described mathematically in Equation E.3.

$$D_{fat} = \sum_i \frac{n_i}{N_i} \tag{E.3}$$

Where, D_{fat} is the total fatigue damage, n_i is the number of cycles in the stress history for the stress range $\Delta\sigma_i$. It is said that the specimen fails for $D_{fat} = 1$, however this means that the 2.3 % failure probability is reached, if the design S-N curves are used. From Equation E.3 it can be deduced that it is necessary to know the values for n_i and N_i to assess the fatigue damage. Therefore a stress history of the structure under investigation must be analysed. That analysis will have to return a distribution of stress ranges and numbers of occurrence, a widely accepted method for this analysis is the rainflow counting technique [60], a further explenation of this method is presented in Appendix E.2. For fatigue damage monitoring it is relevant to relate the fatigue damage to the designed lifetime of the structure. First the design fatigue damage of the in place structure has to be calculated, assuming a driven pile, the total design fatigue damage $D_{d,in-place}$ and its yearly component $D_{d,in-place/year}$ are computed through Equations E.4 and E.5.

$$D_{d,in-place} = 1 - D_{d,driving} \tag{E.4}$$

$$D_{d,in-place/year} = \frac{D_{d,in-place}}{T_{d,life}} \tag{E.5}$$

Here, $D_{d,driving}$ is the damage inflicted during the driving process as calculated in the design phase. Further, $T_{d,life}$ is the design fatigue life in years. Now if a fatigue damage monitoring system is in place, the measured yearly fatigue damage $D_{m,year}$ can be compared to the design values. Since the yearly design fatigue damage is taken to be equal for the entire life time, this gives an interesting insight in the expected total fatigue life.

$$D_{m,\%,year} = \frac{D_{m,year}}{D_{d,in-place/year}} \tag{E.6}$$

A far more detailed and complete description of the fatigue process and fatigue design can be found in the book on fatigue design of marine structures by Lotsberg [53].

As mentioned previously, the fatigue damage per stress range σ_i can be determined by reading out the number of cycles to failure N_i for a specific stress range $\Delta\sigma_i$ from the S-N curve and comparing this to the observed number of cycles in that stress range n_i according to Equation E.3. It is important to note here that the stress range input has an exponent m (see Equation E.1), where m is typically 3 for steel, this means that the stress range plays a fundamental role in the fatigue damage computation. The total damage caused by a time series of variable amplitude loading, e.i. loading of multiple stress ranges can be added up so that $D = \sum_i \frac{n_i}{N_i}$.

$$D_i = \frac{n_i}{N_i} \tag{E.7}$$

From Equations E.1 and E.7 it can be readily deduced that for given values of $\Delta\sigma_1$ and $\Delta\sigma_2$ for the same detail the ratio between the damage D_1 and D_2 is given by Equation E.8 and from this equation it can be easily seen that the ratios $^{\Delta\sigma_1}/_{\Delta\sigma_2} \neq {}^{D_1}/_{D_2}$ if $m_1 \neq m_2$.

$$\frac{D_2}{D_1} = \frac{(\Delta\sigma_1)^{m_1}}{(\Delta\sigma_2)^{m_2}} \tag{E.8}$$

Where m_1 and m_2 are the Wöhler coefficients related to $\Delta\sigma_1$ and $\Delta\sigma_2$, respectively.

E.1.2. Assurance Criteria

An often cited criterion for the accuracy of a computed time signal is the time response assurance criterion (TRAC) [6]. It can be written up as:

$$TRAC = \frac{\left(\sum_t \sigma_m(t)\sigma_p(t)\right)^2}{\left(\sum_t \sigma_m(t)\sigma_m(t)\right)\left(\sum_t \sigma_p(t)\sigma_p(t)\right)} \tag{E.9}$$

Where the TRAC value is between 0 and 1, with 1 being the very accurate and 0 implies no correlation, σ_m are the measured stresses and σ_p are the predicted stresses. A drawback of the TRAC is that it does not consider amplitude differences. To cover amplitude differences as well the weighted two-dimensional Euclidian is taken of the time domain signal, according to Equation E.10.

$$E_t = \frac{\sum_t^K \sqrt{\left(\sigma_m(t) - \sigma_p(t)\right)^2}}{K \cdot \max(\sigma_m(t))} \tag{E.10}$$

With K being the number of measurements in the time signal. A number close to zero means good correlation between the measured and predicted signal. The normalised mean absolute error or MAE can also be utilised, see E.11.

$$MAE = \frac{\sum_t^K \left|\sigma_m(t) - \sigma_p(t)\right|}{K \cdot \max(\sigma_m(t))} \tag{E.11}$$

Now it becomes obvious that if the same sample frequency has been taken for both $\sigma_m(t)$ and $\sigma_p(t)$, the error is one-dimensional and the Euclidian norm and the normalised MAE are equal.

E.1.3. Example

To test the effect of incorrect predicted stress levels, a time series of a constant amplitude signal is chosen to clarify the influence of different parameters. The 'measured' time signal has been plotted in blue in Figure E.2 with a constant amplitude of 200 MPa, the 'predicted' time signal has an amplitude that is 5 % larger than the measured signal, the phase of both signals is identical. As it is of interest how good the stress signal is

predicted and how that influences the fatigue damage that has been imposed on the structural detail both the assurance criteria and the total fatigue damage are compared. This results in a TRAC value of 1.0000 independent of the difference in amplitude. The MAE does show the error in the amplitude to be exactly a maximum of 5 % for the extremes of the time signal, with a sum value of 3.5357 %. Figure E.4 displays the fatigue damage caused by the measure and predicted stress time series, for a detail of class C1 for both the air and free corrosion S-N curves from the DNVGL [76]. Here we see 15.76 % increase for both the air and free corrosion S-N curves, this can be explained by both curves having the same value for the Wöhler coefficient m for the selected stress range. If the stress range passes the fatigue limit of the S-N curve the relation will be altered, this is shown in Table E.2. The values in the table are computed by $(D_s - D_m)/D_m \cdot 100\%$. As comparison a predicted time signal with a phase lag is generated the signal becomes time shifted (Figure E.3) and the TRAC and MAE values will change. A phase lag of 5 % results in a TRAC of 0.9755 and a MAE of 11.0958 %, however the phase lag on its own does not affect the inflicted fatigue damage.

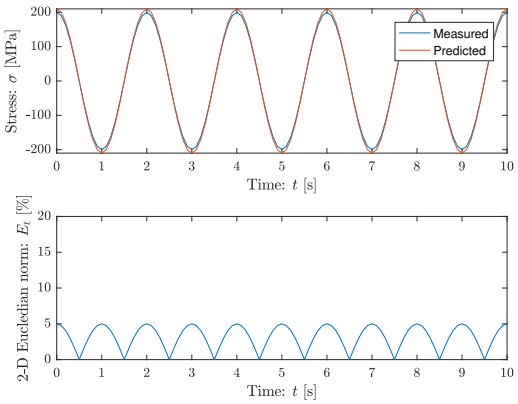

Figure E.2: Top: Practice time series, blue is the measured signal, orange is the predicted signal with increased stress. Bottom: time series of the MAE.

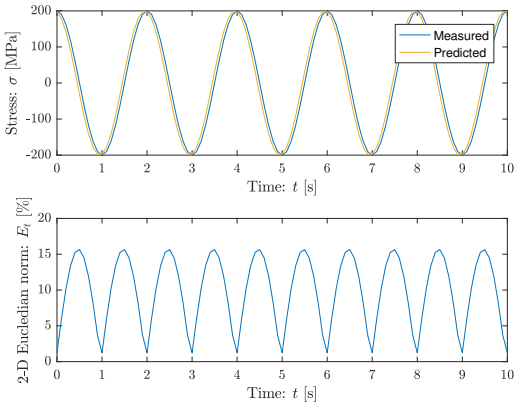

Figure E.3: Top: Practice time series, blue is the measured signal, yellow is the predicted signal with a phase lag. Bottom: time series of the MAE.

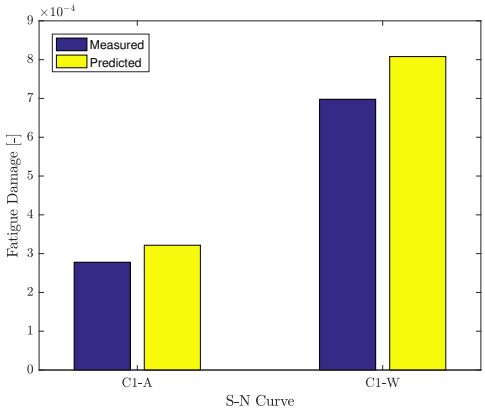

Figure E.4: Total accumulated damage by the stress time series of E.2, for different S-N curves. Control (blue) and Predicted (yellow)

Table E.2: The difference between the fatigue damage computed from measured and predicted stresses in percentages, the rows show an increase in the measured stress range, the columns show an increase in the difference between measured and predicted stress amplitudes. Large errors are introduced around the fatigue limit due to the change in Wöhler coefficient.

	S-N for air			**S-N for seawater with cathodic protection**		
$\Delta\sigma$[MPa]	**+1%**	**+5%**	**+10%**	**+1%**	**+5%**	+10%
40	5.10	27.63	61.05	5.10	27.63	61.05
80	3.03	15.76	33.10	5.10	24.61	43.28
200	3.03	15.76	33.10	3.03	15.76	33.10

E.2. Rainflow Counting

A drop that is falling from a pagoda roof can be taken as an analogy of the rainflow counting algorithm. To define the half-cycles flip the signal by 90°and start at the first point and 'drip down' the signal (roof) until:

1. It drops onto a part of the signal that started at larger maximum (smaller minimum);
2. It meets a flow that is coming from above;
3. It drops to the end of the signal.

If the flow has to be stopped due to one of the above rules, start again at the second turning point and work down the signal until all extremes have been accounted for. In Figure E.5 an example is given for how the half cycles have to be derived and how the rules of the rainflow algorithm are applied, the resulting half-cycles are presented in Table E.3. It can be seen that some half-cycles form a full cycle, or hysteris loop, these can be paired, which results in Table E.4. Table E.5 shows the result of the rainflow counting algorithm that is implemented in matlab [64], as was to be expected it shows it shows the exact same results as the manual application of the rainflow algorithm. Further explanation of the rainflow algorithm can be found in the book on fatigue analysis by Lee et al. [52].

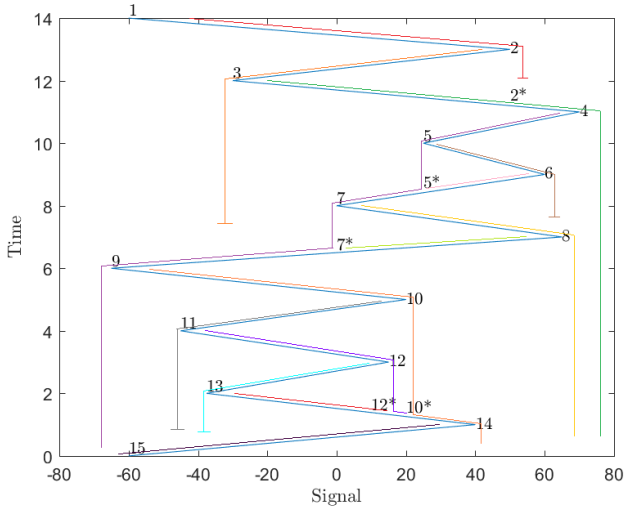

Figure E.5: Rainflow counting method, colored lines represent half cycles.

Table E.3: Manual rainflow counting from signal in Figure E.5

Half-cycle	Max	Min	Max-Min	Amplitude	Mean Value
1-4	70	-60	130	65	5
2-3	50	-30	80	40	10
*3-2**	50	-30	80	40	10
4-9	70	-65	135	67.5	2.5
5-6	60	25	35	17.5	42.5
*6-5**	60	25	35	17.5	42.5
7-8	65	0	65	32.5	32.5
*8-7**	65	0	65	32.5	32.5
9-14	40	-65	105	52.5	-12.5
10-11	20	-45	65	32.5	-12.5
*11-10**	20	-45	65	32.5	-12.5
12-13	15	-37.5	52.5	26.25	-11.25
*13-12**	15	-37.5	52.5	26.25	-11.25
14-15	40	-60	100	50	-10

Table E.4: Manual rainflow counting from signal in Figure E.5

Half-cycle	Max	Min	Max-Min	Amplitude	Mean Value	Number of cycles
*2-3-2**	50	-30	80	40	10	1
*5-6-5**	60	25	35	17.5	42.5	1
*7-8-7**	65	0	65	32.5	32.5	1
1-4	70	-60	130	65	5	0.5
*12-13-12**	15	-37.5	52.5	26.25	-11.25	1
*10-11-10**	20	-45	65	32.5	-12.5	1
4-9	70	-65	135	67.5	2.5	0.5
9-14	40	-65	105	52.5	-12.5	0.5
14-15	40	-60	100	50	-10	0.5

Table E.5: Rainflow counting from signal in Figure E.5, utilising rainflow algorithm

Cycle	Amplitude	Mean Value	Number of cycles
1	40	10	1
2	17.5	42.5	1
3	32.5	32.5	1
4	65	5	0.5
5	26.25	-11.25	1
6	32.5	-12.5	1
7	67.5	2.5	0.5
8	52.5	-12.5	0.5
9	50	-10	0.5

E.3. Hot Spot Stress and Fatigue Life Prediction

E.3.1. Load Sectors for the Hot Spots

As Rambøll describes in the Time Domain Fatigue Analysis [75], 12 equally sized sectors are defined by points around the circumference of the foundation section. This amount of sections was found appropriate as both the wind and wave predictions given in the Basis of Design [69] are stored into 12 direction bins as well. These load sectors will be utilised to orient the load direction relative to the hot spots that are investigated, the orientations will be chosen such that they represent the worst case scenario in each load sector. With a known value for θ_y (from Equations E.12 and E.13) and combining Equations E.14 and E.15 the nominal stress at a hot spot can be computed. The nominal stress that acts on a detail depends on the detail location in relation with the nominal stress direction as defined in Equation E.15.

$$M_b = \sqrt{M_{b,x}^2 + M_{b,y}^2} = \frac{\sqrt{I_{xx}^2 \sigma_{b,y}^2 + I_{xx}^2 \sigma_{b,x}^2}}{R_{in}} \tag{E.12}$$

$$\theta_y = \cos^{-1}\left(\frac{M_{b,y}}{M_b}\right) = \cos^{-1}\left(\frac{I_{xx}\sigma_{b,y}}{M_b R_{in}}\right) \tag{E.13}$$

Where, M_b is moment, I_{xx} is the moment of inertia about the x–axis, σ_b is bending stress, R_{in} is the inner radius and θ_y is the angle between measurement in the y-direction and the load direction, where the positive y-direction is defined parallel to the North arrow. The inner radius needs to be taken into account here as the strain sensors will be applied to the inside of the foundation. Here the assumption is made that the moments of inertia $I_{xx} = I_{yy}$, a small inaccuracy is introduced as the foundation in reality is not fully axis symmetric. See Figures E.6 and E.7 for clarification of the axis definitions. Equation E.13 follows from Equation 2.4. It is further assumed here that the twist in the foundation has a limited effect on the overall stresses, therefore θ_y at any instance in time is expected not to change over the length of the structure

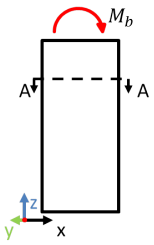

Figure E.6: Cylinder, with radius R and moment of inertia I loaded by a bending moment M_b

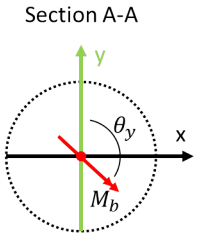

Figure E.7: Section A-A from Figure E.6, here θ_y is defined as the angle between M_b and the y-axis.

$$\sigma_b = \frac{M_b \cdot R_{in}}{I_{xx}} \tag{E.14}$$

$$\sigma_{b,dy} = \sigma_b \cos\left(\theta_y - \theta_{dy}\right) \tag{E.15}$$

where $\sigma_{b,dy}$ is the nominal stress that acts at the detail (dy) location. σ_b is the bending stress and θ_{dy} is the angle describing the orientation of the detail (dy) with respect to North.

$$\sigma_{b,crit} = \left(\frac{M_{b,crit} R_{in,crit}}{I_{xx}}\right) \cos\left(\theta_y - \theta_{dy}\right) \tag{E.16}$$

Where, $\sigma_{b,crit}$ is the nominal stress at the interpolated height and the position of the hot spot and $R_{in,crit}$ is the inner radius of the foundation at the hot spot. $M_{b,crit}$ is computed by the SFI method presented in Section 2.2.1. The hot spot stress is then simply found through Equation E.17.

$$\sigma_{HS} = SCF \cdot \sigma_{b,crit} \tag{E.17}$$

Here, σ_{HS} is the hot spot stress and SCF is the stress concentration factor. DNV-GL recommends utilising the Hot Spot Method to calculate the SCF's, Section 4 of the DNV-GL RP-C203 covers this subject [76].

E.3.2. Fatigue Life Prediction

The hot spot stress histories obtained from the interpolation or the MDE discussed in Chapter 3 are fed into the fatigue calculations, these give the fatigue damage that has been introduced to the structure. The basic methodology of the fatigue calculations as applied in the design for OWT's has been covered in Appendix E.1. The yearly fatigue damage data can be fitted to a normal distribution, of which the average is linearly extrapolated, along with the 95 % upper and lower bound, defined by twice the standard deviation. As more years of data come into the database, the precision of the statistical parameters is increased. Figures E.8 and E.9 present a case where the fatigue damage is extrapolated in such a fashion after 10 and 20 years of measurements, respectively. The case noted here is an example where the original input was a normal distribution with μ_D = 0.032 and $\sigma_D = \mu_D/5$. A normal distribution is assumed as a result of the yearly variation in environmental conditions and their effect on the fatigue damage, the yearly variation for wind speeds is assumed to be normally distributed as well [26]. A risk to this approach is the low number of data points and the detrimental effect that has on the normal distribution fitting.

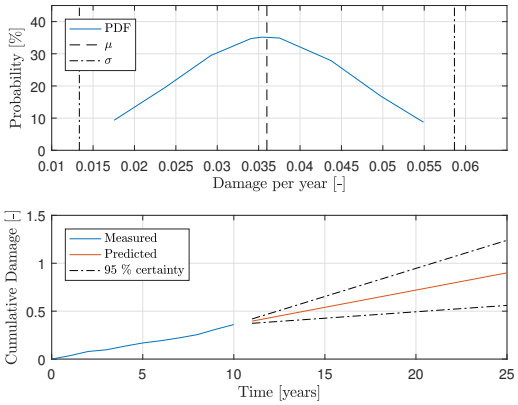

Figure E.8: Top: The measured fatigue damage per year fitted to a normal distribution. Bottom: Extrapolated fatigue damage based on the probability density distribution from the measured data. These results are for measurement data set of 10 years

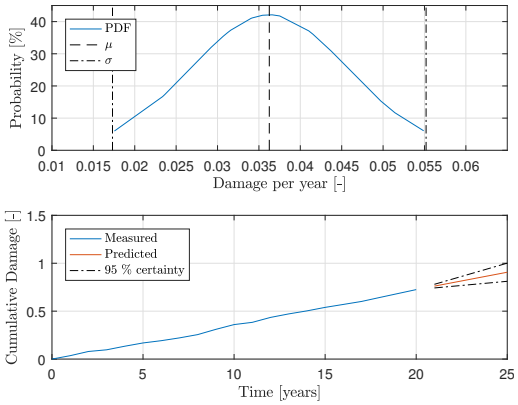

Figure E.9: Top: The measured fatigue damage per year fitted to a normal distribution. Bottom: Extrapolated fatigue damage based on the probability density distribution from the measured data. These results are for measurement data set of 20 years

E.4. Digital Signal Processing

The signal that is read from the sensors has to be processed so that it can be interpreted properly. in this section first the power spectral density (PSD) is discussed, then digital filtering is covered.

E.4.1. Power Spectral Density

When spectral analysis of a digital signal is applied some form the Discrete Fourier Transform (DFT) is utilised. The DFT separates a digital signal into a finite number of digital sinusoids, under the assumption that the original signal is periodic. In this manner a time domain signal can be broken up into its frequency domain counter part. The complex value of the coefficients X_m are calculated for the analysis frequencies f_m. For more information on how the Fourier Transform operates the book by Brandt on Noise and Vibration Analysis gives a thorough introduction [12]. The magnitude spectrum shows the amount of energy that signal contains at what frequencies.
Some issues regarding spectral analysis are the following:

- Windowing
- Leakage
- Zero-padding

Firstly, windowing is related to the fact that the DFT assumes periodicity of the signal, for most real-life problems however this is not the case. So if a finite signal that is not periodic is put into the DFT algorithm, the discontinuity at the first and last point of the time signal cause disturbance in the spectrum. Different types of windows are available to taper the beginning and end of the time signal to zero to decrease the influence of this discontinuity. Choosing a window type is related to what needs to be investigated in the signal, some windows allow the investigation of two close peaks, others allow for the inspection of small contributions of the magnitude spectrum. Leakage is caused by incongruence between the analysis frequencies and the signal frequencies. As the Fourier Transform tries to break up the time signal into a finite number of sinusoids it has a set number of frequencies over which to distribute the energy of the time signal. If the time signal contains energy at a frequency that is not an analysis frequency this energy will 'leak' to other frequencies, on the other hand if the time signal contains only a single frequency which is also an analysis frequency the magnitude spectrum will contain only non-zero entries for that specific frequency. Zero-padding may be applied to increase the number of analysis frequencies for the DFT, this is done by adding zeros to the end of the windowed time signal. Another reason to do this is that DFT algorithms work faster if the input signal is of a length of 2^n, thus a time signal that is not of that form can be zero-padded to the required length.

In this case Welch's method for obtaining the PSD is applied, this entails dividing the time signal into segments and averaging the resulting PSD's for each frequency line, to reduce the random error of the PSD estimate. In this example a time signal of length 12000 and dt = 0.05 s is considered. Use is made of the Hamming window and 8 segments have been defined, with a 50 % overlap and the DFT was computed using 4096 analysis frequencies. In Figure E.10, the displacement PSD for an OWT is displayed.

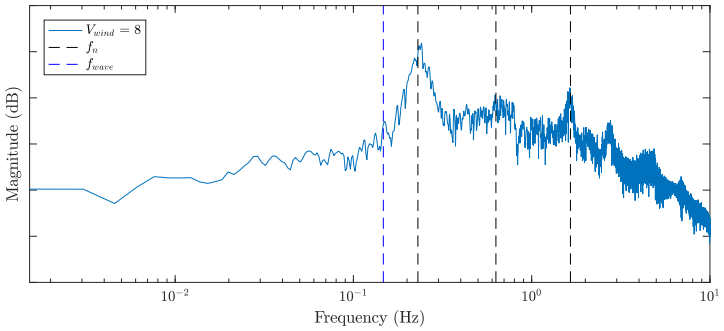

Figure E.10: Power density spectrum obtained with Welch's method, with 3 segments a 50 % overlap and 2^{15} analysis frequencies.

E.4.2. Digital Filtering: IIR vs. FIR

A digital filter is applied to enhance or reduce specific aspects of a signal, the filter performs mathematical operations on the signal to obtain the sought for result. Linear, time-invariant (LTI) systems form the most important class of filters. The linearity refers to the input-output relation and the time-invariance means that the system behaves the same regardless of the time instance at which the input is given. The frequency response of an LTI sytem can be used to fully describe the filter. Equation E.18 prescribes how the frequency response $H(\hat{\omega})$ of a filter maps the values of X_n to U_n, which are the Fourier transforms of x_n and u_n, respectively.

$$U_n(\hat{\omega}) = H(\hat{\omega})\, X_n(\hat{\omega}) \tag{E.18}$$

Here, $\hat{\omega}$ is the normalised angular frequency. The function of the frequency response of an LTI digital filter can be written as:

$$H(\hat{\omega}) = \sum_{k=-\infty}^{\infty} h_k e^{-i\omega k} \tag{E.19}$$

Where, h_k is the impulse response of the filter. The frequency response is a complex function and, similarly to the complex coefficients X_m of the Fourier Transform discussed in Section E.4.1, it has a magnitude $|H(\hat{\omega})|$ and a phase $\Phi(\hat{\omega})$. Another possibility to define the filter is by a difference equation:

$$u_n = \sum_{k=0}^{p} a_k x_{n-k} - \sum_{l=0}^{q} b_l x_{n-l} \tag{E.20}$$

With $\max(p,q)$ is the order of the filter, a_k are the feed forward coefficients and b_l are the feed backward coefficients. This way of defining the filter allows for a simple way to make a distinction between finite impulse response (FIR) filters and infinite impulse response (IIR) filters. FIR filters only have non-zero feed forward coefficients, IIR have at least 1 non-zero feed backward coefficient. For many applications it is important that the output of the filter is not distorted, distortion occurs if different frequency components are delayed by different amounts and it is caused by a non-linear phase response. Typically, it is impossible to design linear phase IIR filters, but it is relatively easy to design linear phase FIR filters.

Phase Response

In Figure E.11 three low pass filters are presented. The first is an ideal filter, the second filter is an IIR Butterworth filter and the last filter is an FIR Hamming filter, the last two have the same order and the same cut-off frequency. A large difference between the IIR and FIR filter can be observed. Two main differences should be noted especially from the magnitude and phase plots. First of all, from the two, the IIR filter has a far steeper drop-off after the cut-off frequency, furthermore the IIR filter has a non-linear phase response as discussed before.

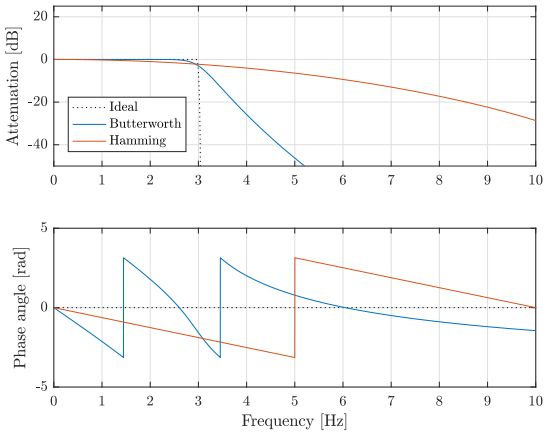

Figure E.11: Frequency response of 10^{th} order low pass filters with cut-off frequency f_c = 3 Hz. Top: Attenuation, bottom: Phase angle.

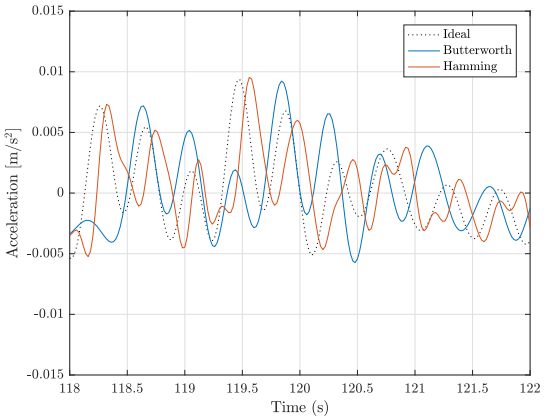

Figure E.12: Time domain result of the filters presented in Figure E.11 (zoomed in).

Figure E.12 shows the effects of the filters in the time domain, the section shown is taken from a time series of 600 seconds. The steeper drop-off of the IIR filter results in less high frequency content, similar to the ideal filter, the time domain result from the FIR filter still contains some higher frequencies as shown by extra peaks in the signal. The non-linear phase response of the IIR filter can also be found in the time domain results, it can be observed that the Butterworth signal shifts for every peak with respect to the ideal signal, while the FIR signal has only been shifted in time by a constant number of samples. The FIR signal can also be restored, by simply shifting it in time, the IIR needs more complicated manipulation to match the original results.

To prevent the IIR filter from distorting the signal, the filter can be applied forward and backward in time [48]. There are some issues regarding this method, namely the entire input data vector must be available. Furthermore, the output of this forward and backward filtering needs to be scaled correctly to ensure a proper magnitude response. The MATLAB function *filtfilt* performs this type of filtering and scaling automatically, for a given filter [59]. Figure E.13 shows the result of this zero-phase filtering method, as well as the effect of time shifting the result from the FIR filtering.

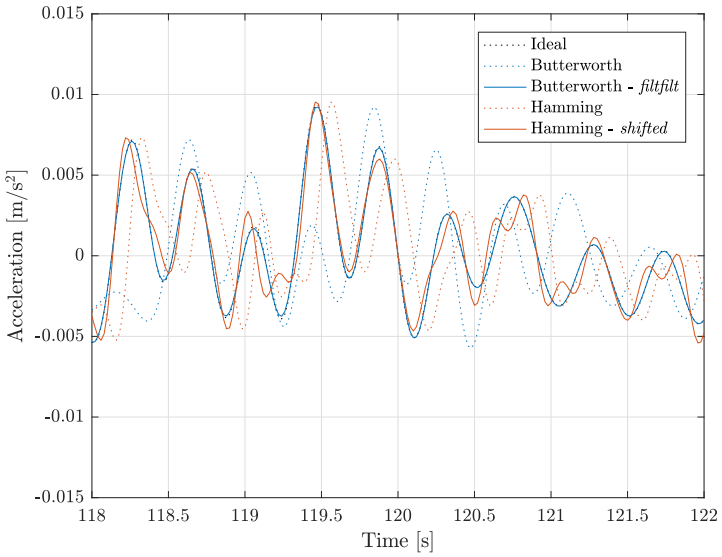

Figure E.13: Improved time domain result of the filters presented in Figure E.11 (zoomed in).

The resulting TRAC and MAE values are presented in Figure E.14. Here, can be observed that the *filtfilt* and *shifted* results are a dramatic improvement on the original results. For the IIR filter the TRAC value increases from 0.054 to 9.999 and the MAE drops to 0.742, the cost for this improvement is an increased calculation time from 0.0011 s to 0.0023 s for a 600 second time signal with a sampling frequency f_s = 50 Hz. For the FIR filter a TRAC of 0.933 can be achieved with an MAE of 5.143, for this improved result a cost of $n/2$ samples has to be paid, where n is the filter order.

It should be noted that the *filtfilt* function results in a non-causal filter, that means that only post processing of stored data is possible, real time filtering cannot be done as the filter requires information from previous and subsequent time steps. This also causes transients to be blurred forwards and backwards in time, this means that distortion by a external influence can appear in the filtered signal before it actually occurs. Equations E.21 through E.24 describe the zero-phase filtering process mathematically, the process can also be seen in the flowchart in Figure E.15. From Equation E.24 it can be concluded that the frequency response of the entire filtering process is $|H(\hat{\omega})|^2$. As this is both real and positive the the phase response has to be zero. However, because $H(\hat{\omega}) \neq |H(\hat{\omega})|^2$ the results $Y_n(\hat{\omega})$ have to be scaled, this is action is included in the *filtfilt* function.

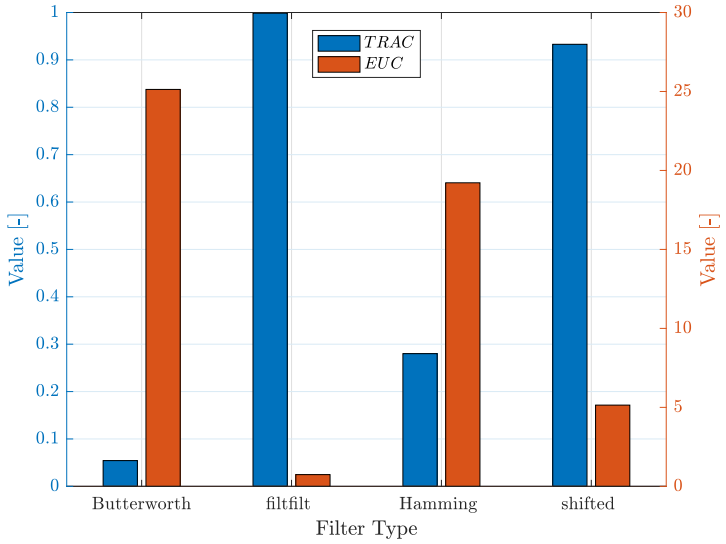

Figure E.14: Assurance criteria for the respective filters and improvement methods. *filtfilt* represent the zero-phase filter function from MATLAB and *shifted* the FIR filtered signal that has been time shifted to match the ideal signal. The axis for the TRAC value can be read off on the right and the MAE axis is presented on the right.

$$U_n(\hat{\omega}) = H(\hat{\omega})\, X_n(\hat{\omega}) \tag{E.21}$$

$$W_n(\hat{\omega}) = U_n^*(\hat{\omega}) = H^*(\hat{\omega})\, X_n^*(\hat{\omega}) \tag{E.22}$$

$$V_n(\hat{\omega}) = H(\hat{\omega})\, W_n(\hat{\omega}) = |H(\hat{\omega})|^2 X_n^*(\hat{\omega}) \tag{E.23}$$

$$Y_n(\hat{\omega}) = V_n^*(\hat{\omega}) = |H(\hat{\omega})|^2 X_n(\hat{\omega}) \tag{E.24}$$

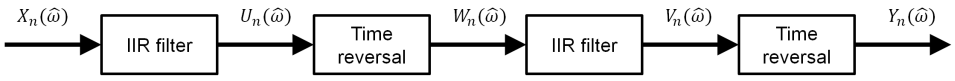

Figure E.15: Flow chart of the zero phase filtering process.

E.4.3. Butterworth Filter Order

For this specific application of the MDE it is necessary to split the original signal into a quasi-static (QS) signal, a low frequency (LF) signal and a high frequency (HF) signal. To obtain these different signals three separate filters are used on the original signal. A low pass filter with cut-off frequency $f_{c,1} = 0.075$ Hz is used to get the QS content (Figure E.16), a band pass filter with cut-off frequencies $f_{c,1} = 0.075$ Hz and $f_{c,2} = 0.4$ Hz selects the LF band (Figure E.17) and a second band pass filter with cut-off frequencies $f_{c,2} = 0.4$ Hz and $f_{c,3} = 10$ Hz for the HF signal (Figure E.18). It is found that for some cases the algorithm performs better if the cut-off frequencies are shifted somewhat, e.g. $f_{c,2}$ should be shifted to 0.35 Hz for a wind speed of 8 m/s.

From Figures E.16 trough E.18 it is clear that the phase response of the filters is non-linear, as to be expected for IIR filters. The choice for a Butterworth IIR filter is made to emulate the method applied by Illiopoulos et al., also this type of filter results in a maximally flat magnitude response in the pass band. Appendix E.4 gives more insights in the influence of the type of filter on the results of the state estimation.

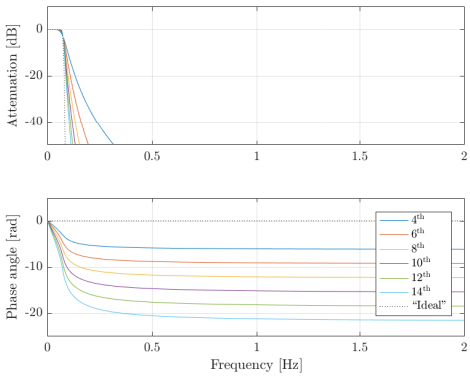

Figure E.16: Frequency response of different order low pass Butterworth filters, with a cut-off frequency $f_{c,1}$ = 0.075 Hz. Top: Attenuation, bottom: Phase angle.

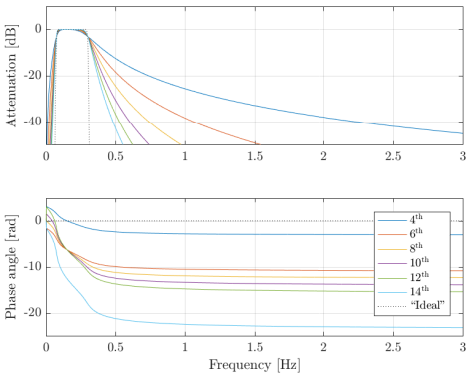

Figure E.17: Frequency response of different order band pass Butterworth filters with cut-off frequencies $f_{c,1}$ = 0.075 Hz and $f_{c,2}$ = 0.3 Hz. Top: Attenuation, bottom: Phase angle.

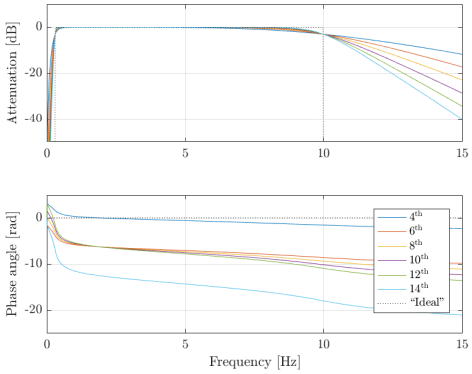

Figure E.18: Frequency response of different order band pass Butterworth filters with cut-off frequencies $f_{c,2}$ = 0.3 Hz and $f_{c,3}$ = 10 Hz. Top: Attenuation, bottom: Phase angle.

E.4.4. Filter Order & Stability

It may be observed in Figures E.16 and E.17 that the drop off, for increased order, becomes steeper. By simply looking at the frequency responses of the amplitude and phase it looks like there is no drawback of increasing the filter order. However, as will become evident in the following, increasing the filter order increases the number of filter coefficients and thus the transient distortion introduced in the signal due to the filling up of these coefficients becomes more influential.

To inspect the effect of the order of a filter on the results, the following test has been performed. First, the original data set is separated in the QS, LF and HF band, by the filters presented in Figures E.16 through E.18. Then the separated signals are compared with the results of an "ideal" filter, more information on this filter can be found in the subsection *Ideal Filter* at the end of this section. The results of the investigation into the filter orders have been provided in Table E.6. There is a clear increase in the result of the LF and HF bands by increasing the filter order from 4 to 10, however a sharp drop-off is seen for the 14^{th} order, furthermore some extra computer time is required for the higher order filters. For the QS band it is shown that the assurance criteria give very low scores, this can be explained by the lack of low frequency content in the original signal, thus any small error is magnified. The reconstructed signals are plotted in the time domain to see what the practical result is, see Figure E.19. On visual inspection it can be concluded that especially near the beginning and end the reconstructed signal deviate. A solution to this can be to cut off these parts of the signal and look at the middle section for the quality of the reproduced signal. In Figure E.21 can be seen that all filters perform very well and that the original signal can hardly be distinguished. Figures E.22 and E.23 show that by only looking at the middle section of the signal the assurance criteria can be improved dramatically. A real-life solution could be to cut up the original signal in several overlapping sections. For each section the

transient is disregarded, but due to the overlap the original signal can still, almost completely, be reproduced.

Because the time domain results do not show such a large improvement from the 4^{th} to the 6^{th} order and to keep in line with the method prescribed by Iliopoulos, it is decided to continue with the 4^{th} order Butterworth filter.

Table E.6: Assurance criteria and process time for different filter orders of the Butterworth IIR filter, for a 600 second time history of accelerations with a sampling rate of 50 Hz.

		TRAC [-]			**MAE [-]**			**Time [s]**		
Signal	**Order:**	**4**	**10**	**14**	**4**	**10**	**14**	**4**	**10**	**14**
QS		0.0193	0.0344	0.0368	$1.4466 \cdot 10^4$	$3.2642 \cdot 10^3$	$1.3898 \cdot 10^4$	0.0026	0.0086	0.0093
LF		0.0292	0.2458	0.0033	21.3994	10.2317	138.3981	0.0029	0.0041	0.0055
HF		0.9159	0.9924	0.9238	0.0474	0.0204	0.0484	0.0035	0.0040	0.0052
Reconstructed		0.7487	0.9879	0.4720	0.1065	0.0342	0.3582	-	-	-

Ideal Filter

Here, an 8000^{th} order FIR filter is used that is based on a Hamming window, the frequency response of this filter is plotted in Figures E.16 through E.18 as well. The sharp drop-off around the cut-off frequencies ensures that only the frequencies of interest will be transmitted to the filtered signal, furthermore the linear phase response of the FIR filter allows for a simple reconstruction of the original phase, by shifting the signal in time to match the group delay caused by the filter. The shifting of the signal in time is directly influenced by the order of the filter, this means that for high order filters large amounts of data points are lost in this shifting process, therefore this kind of filter is not preferable in an actual measurement system. Even more, these high order filters have an operation time that is a factor 20 higher than the IIR filters presented above, which makes them even more undesirable for large data sets.

E.4.5. Non-Linear Phase response

As already shortly mentioned, the phase response of the Butterworth filter is non-linear, this results in an unequal phase shift of the frequencies. This means that signal becomes distorted and cannot be recovered as easily as with an FIR filter. Appendix E.4 gives a solution to this problem, which also has been applied in Section E.4.4. Another work-around for the MDE application is found by applying the same filters to the control data as to the measurement data, because the signal will be distorted in a similar way the two distorted signals should match each other. Thus the following approach is utilised:

1. Filter raw acceleration data for LF and HF bands using Butterworth band pass filters;
2. Decompose filtered data to obtain “modal accelerations”;
3. Integrate “modal accelerations” twice to get “modal displacements”;
4. Use the strain distributions (see Section 4.1.3) to predict the dynamic strains in the LF and HF bands;
5. Add the LF and HF strain contributions
6. Filter the control measurements (strain) using the same Butterworth filters as for the acceleration data;
7. Filter the raw strain data for the QS band using a 4^{th} order Butterworth low pass filters;
8. The QS and dynamic strain contributions are superimposed to get the total strain.

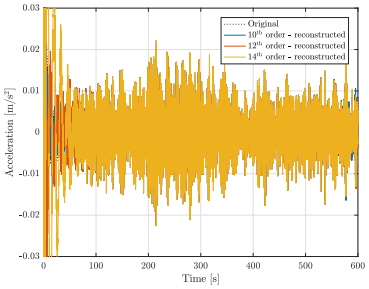

Figure E.19: Reconstructed signals from the different filter orders.

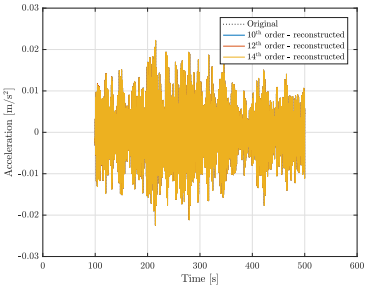

Figure E.20: Reconstructed signals from the different filter orders, the first and last 100 s have been cut off.

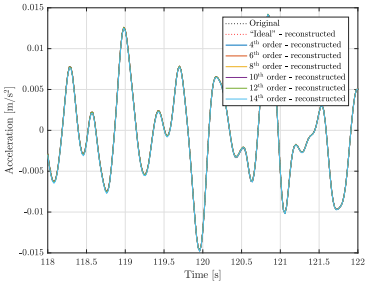

Figure E.21: Reconstructed signals from the different filter orders (zoomed in).

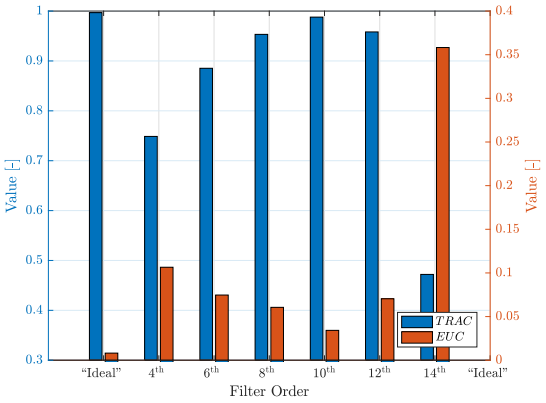

Figure E.22: The TRAC and MAE assurance criteria have applied on the reconstructed signals from Figure E.19.

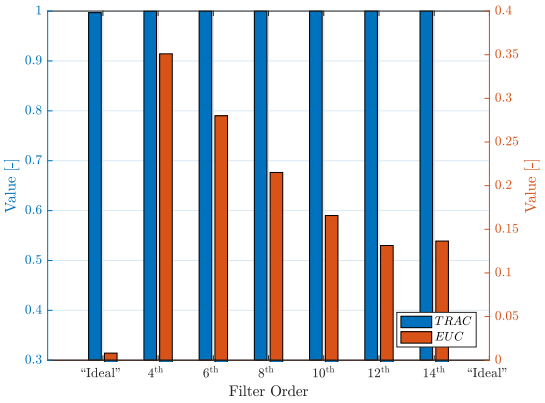

Figure E.23: The TRAC and MAE assurance criteria have applied on the reconstructed windowed signals from Figure E.20.

E.5. Modal Decomposition & Expansion

For the MDE method an example is given where two sinusoidal forces have been used as input, one in the x-direction and one in the y-direction, the time series of these forces are displayed in Figure E.24. The force in the x-direction F_x has been applied on at a height of 89.09 m + LAT (Node 902) and the force in the y-direction F_y at 18.60 m (Node 1101). The nodes that were read out for this exercise are noted in Table E.7, from these 5 nodes the highest three are selected as measurement levels and the lowest two are predicted. Thus the accelerations (measured in both x- and y-directions) for Node 902, 1010 and 1101 are used as input for the estimation and the accelerations for Node 1188 and 1424 are reference material for the estimated accelerations at these nodes using the MDE algorithm.

Table E.7: Selection of nodes that has been investigated for this example, from the FE model of the support structures of the ZEC5 location of the Gemini wind farm.

Node number	Node height + LAT [m]
902	89.09
1010	66.83
1101	18.60
1188	-24.50
1424	-48.00

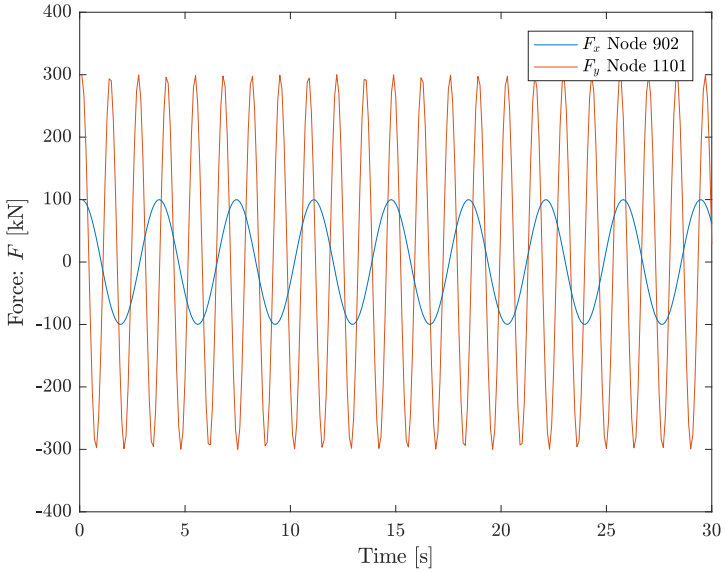

Figure E.24: Excitation forces chosen to be sinusoids with frequencies f_{F_x} = 0.27 Hz and f_{F_y} = 0.74 Hz and amplitudes A_{F_x} = 100 kN and A_{F_y} = 300 kN.

A section of the measured and predicted accelerations at Nodes 1188 and 1424 are plotted in Figure E.25 and E.26. Both figures show that after the first 5 seconds a good prediction of the measured response is obtained. It is clear that the MDE algorithm is able to split up 3-D displacements into the relevant 2-D modes and that for a simple load case the exact frequencies and amplitudes are estimated. Figure E.27 shows the absolute difference for the accelerations in x- and y-direction for both of the predicted nodes. The figure shows a significant error for the first part of the signal, but the error values drop quickly. in Table E.8 the TRAC and MAE results are summarised, all values indicate a good correlation between the predicted and measured signals. However, there is a better estimation for the x-accelerations than for the y-accelerations.

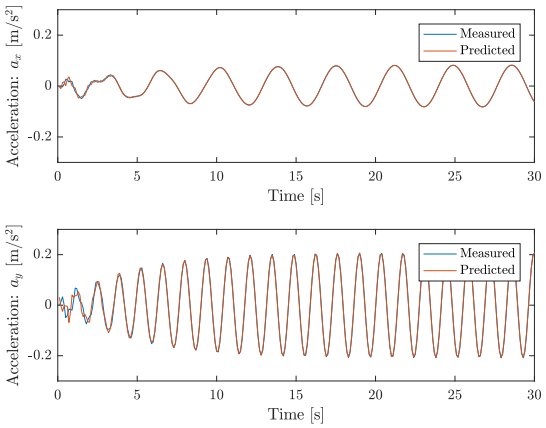

Figure E.25: Predicted signal compared to the measured signal for FE model node 1188. Top: accelerations in x-direction, bottom: accelerations in y-direction.

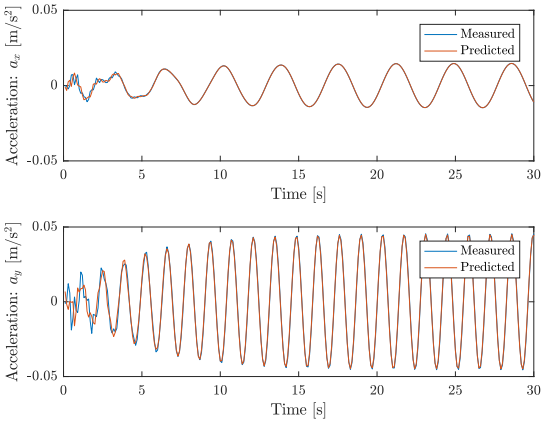

Figure E.26: Predicted signal compared to the measured signal for FE model node 1424. Top: accelerations in x-direction, bottom: accelerations in y-direction.

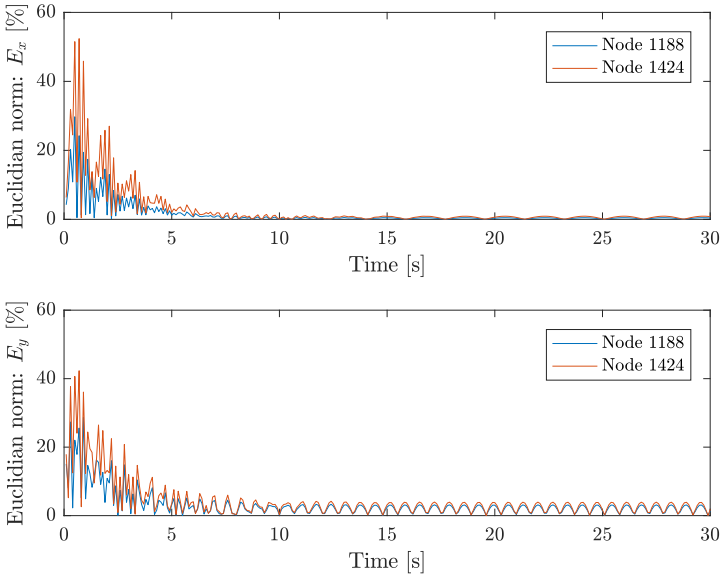

Figure E.27: MAE for the estimation of the acceleration time history of Node 1188 and Node 1424. Top: accelerations in x-direction, bottom: accelerations in y-direction

Table E.8: TRAC and MAE results for the prediction of the accelerations at Node 1188 and 1424.

	MAE		**TRAC**	
Node number	**x**	**y**	**x**	**y**
1188	0.0455	0.1923	0.9991	0.9978
1424	0.0860	0.2382	0.9966	0.9956

F

Original Multi-Band Settings

		Case definitions						MDE sensor/mode settings									
		v_{wind} (m/s)		rpm		Pitch		VLF band		LF band		HF band					
	Cases	Min.	Max.	Min.	Max.	Min.	Max.	0–0.2 Hz		0.2–0.5 Hz		0.5-2 Hz					
1	Pitch: >80	–	–	–	–	80	100	ε_{41m}	ϕ_{ε}^{QS}	α_{70m}	ϕ^{FA1}	α_{70m}, α_{27m}, α_{19m}	ϕ^{FA1}, ϕ^{FA2}				
2	Pitch: ±80	0	20	–	–	70	80	ε_{41m}	ϕ_{ε}^{QS}	α_{70m}	ϕ^{FA1}	α_{70m}, α_{27m}, α_{19m}	ϕ^{FA1}, ϕ^{FA2}				
3	Pitch: ±20	–	–	–	–	19.5	20.5	ε_{41m}	ϕ_{ε}^{QS}	α_{70m}	ϕ^{FA1}	α_{70m}, α_{27m}, α_{19m}	ϕ^{FA1}, ϕ^{FA2}, ϕ^{FA3}				
4	RPM: <10	–	–	2.5	9.8	–	–	ε_{41m}	ϕ_{ε}^{QS}	α_{70m}	ϕ^{FA1}	α_{70m}, α_{27m}, α_{19m}	ϕ^{FA1}, ϕ^{FA2}, ϕ^{FA3}				
5	RPM: ±10	–	–	9.8	10.2	–	–	ε_{41m}	ϕ_{ε}^{QS}	α_{70m}	ϕ^{FA1}	α_{70m}, α_{27m}, α_{19m}	ϕ^{FA1}, ϕ^{FA2}, ϕ^{FA3}				
6	RPM: <16	–	–	10.2	15.9	–	–	ε_{41m}	ϕ_{ε}^{QS}	α_{70m}	ϕ^{FA1}	α_{70m}, α_{27m}, α_{19m}	ϕ^{FA1}, ϕ^{FA2}, ϕ^{FA3}				
7	RPM: ±16	–	–	15.9	17	–	–	ε_{41m}	ϕ_{ε}^{QS}	α_{70m}	ϕ^{FA1}	α_{27m}, α_{19m}	ϕ^{FA1}, ϕ^{FA2}				
8	Cut-Out	20	–	–	–	70	80	ε_{41m}	ϕ_{ε}^{QS}	α_{70m}	ϕ^{FA1}	α_{70m}, α_{27m}, α_{19m}	ϕ^{FA1}, ϕ^{FA2}				

Figure F.1: Overview of the cases and the sensor/mode settings for each frequency band considered in the multi-band MDE algorithm. VLF stands for very low frequency and represents the quasi-static band. [38].

G

Results - Graphs and Tables

G.1. Strain Reconstruction based on Section Force Interpolation

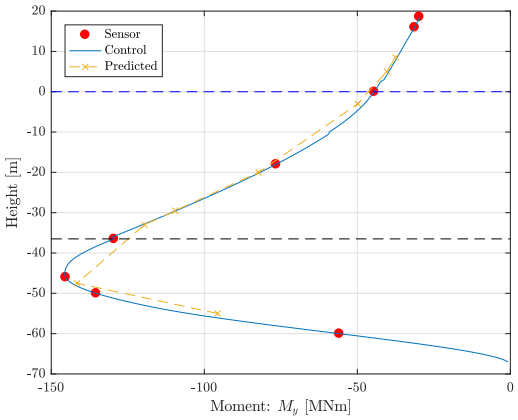

Figure G.1: The bending moment found from the measurements for the SFI method are plotted along the height of a homogeneous foundation with their related values for time = 268.94 s, LC 7.

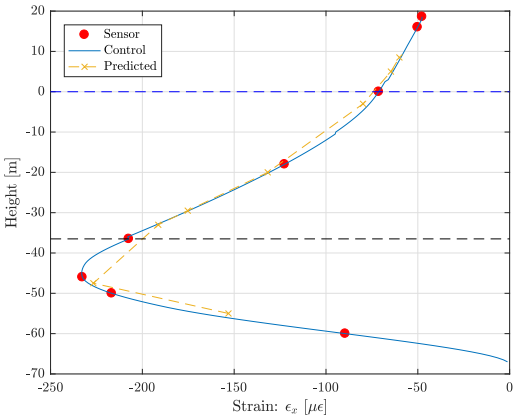

Figure G.2: The measurement locations for the SFI method are plotted along the height of a homogeneous foundation with their related values for time = 268.94 s, LC 7.

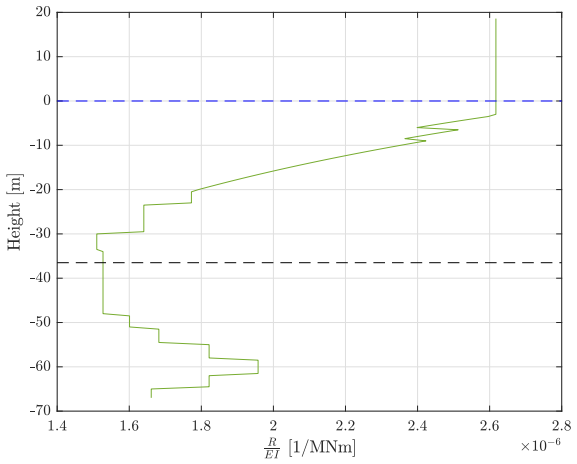

Figure G.3: Representation of the changing foundation geometry, for Figures 5.3 and 5.4. R/EI is the factor that converts bending moments to strains.

G.2. Strain Reconstruction based on Multi-Band Modal Decomposition & Expansion

It should be noted here that the tables presented in this section are error statistics and do not represent mean values and standard deviations of the actual strain signals, but relate to the assurance criteria over the length of the foundation.

Table G.1: Here the assurance criteria for the different configurations of HF band for the Multi-Band MDE are presented for LC 1 and a noise level of 0 %, the values in cells that are highlighted in red perform worse than cells highlighted in green.

noise level 0 %	**Load Case 1**					
Configurations	**MAE (mean)**	**MAE (std)**	**TRAC(mean)**	**TRAC(std)**	**Error_D (mean) [%]**	**Error_D (std) [%]**
Mode: 1, Sensor: 87m	0.5003	0.2400	0.9972	0.0021	4.7427	2.6042
Mode: 1, Sensor: 66m	0.4713	0.2059	0.9975	0.0016	4.8269	2.6120
Mode: 1, Sensor: 34m	0.4653	0.1219	0.9976	0.0009	5.6442	2.7733
Mode: 1, Sensor: 19m	0.5237	0.0851	0.9971	0.0009	6.0927	2.8408
Mode: 1, Sensor: 87m	0.0166	0.0068	0.9966	0.0023	3.9775	1.2539
Mode: 1, Sensor: 66m	0.0152	0.0060	0.9971	0.0018	4.0605	1.2298
Mode: 1, Sensor: 34m	0.0139	0.0031	0.9977	0.0008	4.9003	1.5117
Mode: 1, Sensor: 19m	0.0153	0.0018	0.9973	0.0006	5.5206	1.9277
Mode: 1, Sensor: 87&66m	0.0147	0.0022	0.9975	0.0006	5.4926	1.7591
Mode: 1, Sensor: 87&34m	0.0151	0.0021	0.9974	0.0006	5.6394	1.8263
Mode: 1, Sensor: 87&19m	0.0152	0.0020	0.9973	0.0006	5.6177	1.8680
Mode: 1, Sensor:66&34m	0.0140	0.0037	0.9976	0.0010	4.9228	1.4432
Mode: 1, Sensor:66&19m	0.0140	0.0036	0.9976	0.0010	5.0103	1.4548
Mode: 1, Sensor:34&19m	0.0157	0.0063	0.9969	0.0020	4.0582	1.2356
Mode: 1, Sensor: 87,66,&34m	0.0147	0.0024	0.9975	0.0007	5.5393	1.7079
Mode: 1, Sensor: 87,66,&19m	0.0147	0.0023	0.9975	0.0007	5.5490	1.7406
Mode: 1, Sensor: 66,34,&19m	0.0141	0.0040	0.9976	0.0011	4.9706	1.3952
Mode: 1, Sensor: 87,34,&19m	0.0150	0.0023	0.9974	0.0007	5.7029	1.7696
Mode: 1, Sensor: 87,66,34&19m	0.0146	0.0025	0.9975	0.0007	5.5756	1.6583
Mode: 1&2, Sensor: 87&66m	0.0150	0.0061	0.9971	0.0017	3.6565	3.5734
Mode: 1&2, Sensor: 87&34m	0.0127	0.0037	0.9980	0.0010	3.7455	1.6639
Mode: 1&2, Sensor: 87&19m	0.0124	0.0032	0.9981	0.0008	4.2702	1.0419
Mode: 1&2, Sensor: 66&34m	0.0104	0.0022	0.9986	0.0005	3.3756	0.7901
Mode: 1&2, Sensor: 66&19m	0.0098	0.0020	0.9987	0.0004	3.1496	0.7667
Mode: 1&2, Sensor: 34&19m	0.0073	0.0016	0.9991	0.0002	4.2584	2.5665
Mode: 1&2, Sensor: 87,66&34m	0.0129	0.0041	0.9979	0.0010	3.5390	1.5827
Mode: 1&2, Sensor: 87,66&19m	0.0126	0.0037	0.9980	0.0009	3.5820	1.9348
Mode: 1&2, Sensor: 66,34&19m	0.0101	0.0021	0.9986	0.0005	3.2720	0.6089
Mode: 1&2, Sensor: 87,34&19m	0.0125	0.0035	0.9980	0.0009	4.0333	1.3483
Mode: 1&2, Sensor: 87,66,34&19m	0.0124	0.0035	0.9980	0.0009	3.6977	1.8239
Mode: 2&3, Sensor: 87&66m	0.0264	0.0142	0.9913	0.0064	23.3614	22.0807
Mode: 2&3, Sensor: 87&34m	0.0423	0.0202	0.9795	0.0151	55.7983	49.0143
Mode: 2&3, Sensor: 87&19m	0.0557	0.0253	0.9660	0.0242	97.1773	81.8945
Mode: 2&3, Sensor: 66&34m	0.0108	0.0027	0.9985	0.0006	7.9331	5.4711
Mode: 2&3, Sensor: 66&19m	0.0098	0.0020	0.9987	0.0004	7.3226	4.8633
Mode: 2&3, Sensor: 34&19m	0.0064	0.0011	0.9992	0.0001	5.5113	3.5918
Mode: 2&3, Sensor: 87,66&34m	0.0201	0.0090	0.9951	0.0032	15.7487	13.7693
Mode: 2&3, Sensor: 87,66&19m	0.0175	0.0071	0.9963	0.0023	13.3115	11.0437
Mode: 2&3, Sensor: 66,34&19m	0.0101	0.0022	0.9986	0.0005	7.4834	5.0347
Mode: 2&3, Sensor: 87,34&19m	0.0392	0.0179	0.9825	0.0126	47.7270	41.0671
Mode: 2&3, Sensor: 87,66,34&19m	0.0172	0.0067	0.9965	0.0021	13.0885	10.4533
Mode: 1,2&3, Sensor: 87,66&34m	0.0066	0.0011	0.9992	0.0001	4.5208	2.9777
Mode: 1,2&3, Sensor: 87,66&19m	0.0064	0.0011	0.9992	0.0001	4.6026	3.0900
Mode: 1,2&3, Sensor: 66,34&19m	0.0061	0.0011	0.9993	0.0001	5.4416	3.5671
Mode: 1,2&3, Sensor: 87,34&19m	0.0061	0.0011	0.9993	0.0001	5.3033	3.5258
Mode: 1,2&3, Sensor: 87,66,34&19m	0.0065	0.0011	0.9992	0.0001	4.5925	3.0543
Mode: 2,3&4, Sensor: 87,66&34m	0.0907	0.0371	0.9191	0.0574	325.6271	361.5421
Mode: 2,3&4, Sensor: 87,66&19m	0.2097	0.1105	0.7066	0.1955	9703.6959	15960.8767
Mode: 2,3&4, Sensor: 66,34&19m	0.0076	0.0015	0.9991	0.0002	5.9661	3.4958
Mode: 2,3&4, Sensor: 87,34&19m	0.0822	0.0575	0.9199	0.0851	296.3430	406.2876
Mode: 2,3&4, Sensor: 87,66,34&19m	0.0649	0.0270	0.9558	0.0331	133.7959	129.4770
Mode: 1,2,3&4, Sensor: 87,66,34,19m	0.0060	0.0012	0.9993	0.0001	5.8258	3.4682

Table G.2: Here the assurance criteria for the different configurations of HF band for the Multi-Band MDE are presented for LC 1 and a noise level of 5 %, the values in cells that are highlighted in red perform worse than cells highlighted in green.

noise level 5 %	**Load Case 1**					
Configurations	**MAE (mean)**	**MAE (std)**	**TRAC(mean)**	**TRAC(std)**	**Error$_D$ (mean) [%]**	**Error$_D$ (std) [%]**
Mode: 1, Sensor: 87m	0.1174	0.0146	0.9860	0.0046	14.6826	9.6972
Mode: 1, Sensor: 87m	0.0373	0.0054	0.9861	0.0044	15.9740	10.7691
Mode: 1, Sensor: 66m	0.0366	0.0052	0.9867	0.0042	16.0559	10.8417
Mode: 1, Sensor: 34m	0.0357	0.0048	0.9873	0.0039	16.2952	11.1030
Mode: 1, Sensor: 19m	0.0362	0.0043	0.9869	0.0037	16.8737	11.6268
Mode: 1, Sensor: 87&66m	0.0359	0.0045	0.9871	0.0038	16.7386	11.5038
Mode: 1, Sensor: 87&34m	0.0361	0.0044	0.9870	0.0038	16.8664	11.6246
Mode: 1, Sensor: 87&19m	0.0361	0.0044	0.9870	0.0038	16.8821	11.6256
Mode: 1, Sensor:66&34m	0.0358	0.0048	0.9872	0.0039	16.3103	11.0964
Mode: 1, Sensor:66&19m	0.0358	0.0048	0.9872	0.0039	16.3343	11.1070
Mode: 1, Sensor:34&19m	0.0368	0.0053	0.9865	0.0042	16.0608	10.8379
Mode: 1, Sensor: 87,66,&34m	0.0359	0.0045	0.9871	0.0038	16.7355	11.5017
Mode: 1, Sensor: 87,66,&19m	0.0359	0.0045	0.9871	0.0038	16.7473	11.5122
Mode: 1, Sensor: 66,34,&19m	0.0359	0.0049	0.9872	0.0040	16.3138	11.0951
Mode: 1, Sensor: 87,34,&19m	0.0361	0.0045	0.9870	0.0038	16.8573	11.6148
Mode: 1, Sensor: 87,66,34&19m	0.0359	0.0046	0.9871	0.0038	16.7274	11.4957
Mode: 1&2, Sensor: 87&66m	0.0365	0.0055	0.9867	0.0045	17.8153	10.9706
Mode: 1&2, Sensor: 87&34m	0.0354	0.0042	0.9876	0.0035	16.5957	10.4766
Mode: 1&2, Sensor: 87&19m	0.0352	0.0039	0.9877	0.0032	16.4992	10.5266
Mode: 1&2, Sensor: 66&34m	0.0345	0.0038	0.9882	0.0032	15.8141	10.0252
Mode: 1&2, Sensor: 66&19m	0.0343	0.0037	0.9883	0.0031	15.3632	9.6585
Mode: 1&2, Sensor: 34&19m	0.0342	0.0041	0.9883	0.0034	10.5149	6.7912
Mode: 1&2, Sensor: 87,66&34m	0.0355	0.0044	0.9875	0.0037	16.8883	10.6194
Mode: 1&2, Sensor: 87,66&19m	0.0353	0.0042	0.9876	0.0035	16.8454	10.6378
Mode: 1&2, Sensor: 66,34&19m	0.0344	0.0038	0.9883	0.0032	15.5841	9.8503
Mode: 1&2, Sensor: 87,34&19m	0.0353	0.0040	0.9876	0.0034	16.5506	10.4963
Mode: 1&2, Sensor: 87,66,34&19m	0.0352	0.0042	0.9877	0.0035	16.7384	10.5875
Mode: 2&3, Sensor: 87&66m	0.0430	0.0102	0.9805	0.0091	15.4895	10.2598
Mode: 2&3, Sensor: 87&34m	0.0547	0.0160	0.9680	0.0166	45.8851	29.1568
Mode: 2&3, Sensor: 87&19m	0.0658	0.0211	0.9540	0.0253	86.2968	60.3593
Mode: 2&3, Sensor: 66&34m	0.0345	0.0041	0.9880	0.0033	8.5944	6.4643
Mode: 2&3, Sensor: 66&19m	0.0342	0.0039	0.9882	0.0032	9.4255	6.5806
Mode: 2&3, Sensor: 34&19m	0.0342	0.0041	0.9883	0.0034	9.5430	7.0099
Mode: 2&3, Sensor: 87,66&34m	0.0387	0.0064	0.9845	0.0053	7.8361	6.8829
Mode: 2&3, Sensor: 87,66&19m	0.0373	0.0054	0.9858	0.0045	6.7350	6.5471
Mode: 2&3, Sensor: 66,34&19m	0.0343	0.0040	0.9882	0.0033	9.1688	6.5136
Mode: 2&3, Sensor: 87,34&19m	0.0522	0.0138	0.9712	0.0138	38.2124	21.8952
Mode: 2&3, Sensor: 87,66,34&19m	0.0371	0.0051	0.9859	0.0042	6.9487	6.1898
Mode: 1,2&3, Sensor: 87,66&34m	0.0337	0.0041	0.9888	0.0034	10.7197	6.8041
Mode: 1,2&3, Sensor: 87,66&19m	0.0336	0.0041	0.9888	0.0034	10.7737	6.8888
Mode: 1,2&3, Sensor: 66,34&19m	0.0344	0.0039	0.9881	0.0033	9.6010	7.0993
Mode: 1,2&3, Sensor: 87,34&19m	0.0342	0.0041	0.9883	0.0034	9.5530	7.0034
Mode: 1,2&3, Sensor: 87,66,34&19m	0.0336	0.0041	0.9888	0.0034	10.7765	6.8607
Mode: 2,3&4, Sensor: 87,66&34m	0.0983	0.0341	0.9040	0.0581	321.0901	361.3841
Mode: 2,3&4, Sensor: 87,66&19m	0.2149	0.1088	0.6883	0.1959	10073.1058	16650.1869
Mode: 2,3&4, Sensor: 66,34&19m	0.0355	0.0026	0.9873	0.0023	12.1593	5.4713
Mode: 2,3&4, Sensor: 87,34&19m	0.0931	0.0515	0.9054	0.0859	329.5183	464.7361
Mode: 2,3&4, Sensor: 87,66,34&19m	0.0747	0.0229	0.9420	0.0330	128.3507	126.7956
Mode: 1,2,3&4, Sensor: 87,66,34,19m	0.0353	0.0027	0.9875	0.0024	12.1304	5.5839